# Unbonded Pre-tensioned Bridge Columns with Hybrid Fiber-Reinforced Concrete Shells

Gunnsteinn Finnsson

A thesis

Submitted in partial fulfillment of the

Requirements for the degree of

Master of Science in Civil Engineering

University of Washington

2013

Committee:

Marc O. Eberhard

Charles W. Roeder

John F. Stanton

Program Authorized to Offer Degree:

Department of Civil and Environmental Engineering

University of Washington

**Abstract**

Unbonded Pre-tensioned Bridge Columns with Hybrid Fiber-Reinforced Concrete Shells

Gunnsteinn Finnsson

Chair of the Supervisory Committee:
Professor Marc O. Eberhard and
Professor John F. Stanton

Many bridges in the United States are obsolete or deficient, and will need to be replaced in the near future. If the new bridges are constructed with conventional cast-in-place concrete, the construction will cause traffic congestion, which is a costly problem. Furthermore, cast-in-place concrete structures are susceptible to earthquake-induced damage, such as concrete spalling, bar buckling, bar fracture and residual displacements.

A new pre-tensioned precast bridge bent system has been developed to meet these challenges. The system makes use of (1) precast technology to accelerate the bridge construction, (2) unbonded pre-tensioning to minimize residual displacements, and (3) high-performance materials to reduce earthquake damage and extend the bridge‘s durability.

The seismic performance of the system was investigated with pseudo-static tests of two column-footing subassemblies. Both specimens featured a shell of ductile concrete (HyFRC, developed by Ostertag) in the plastic-hinge region of the columns. The longitudinal reinforcement consisted of conventional steel bars in one column and stainless steel bars in the other .The test results showed that the use of HyFRC delayed spalling of the concrete, and to a lesser extent, buckling of the bars. The use of stainless steel had little effect on the observed damage.

# Table of Contents

# List of Figures

# List of Tables

# 1 Introduction

This report describes the development and laboratory testing of a new concrete bent system for bridges. The system was developed:

- to accelerate bridge construction,
- to improve the seismic performance of the bents compared with conventional reinforced concrete bents, and
- to increase the durability of the bents.

The system is shown schematically in Figure 1-1.

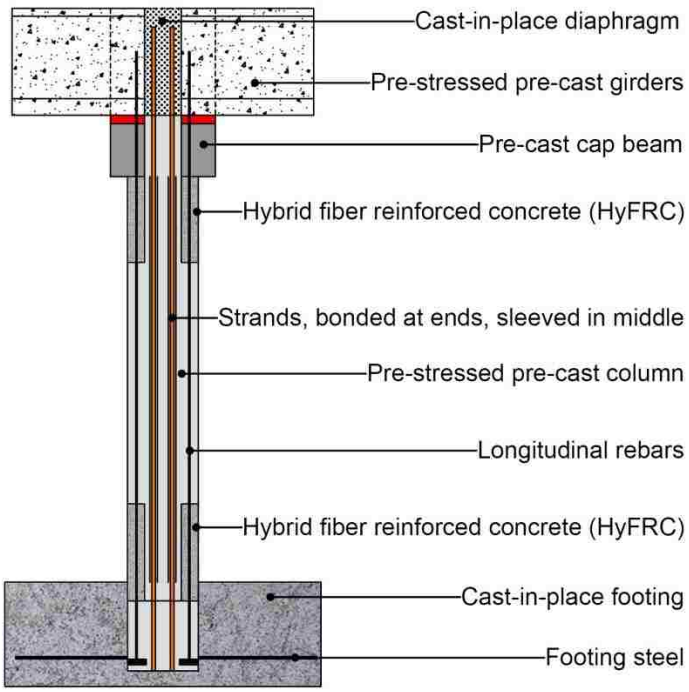


**Figure 1-1: Elevation of prestressed concrete column system (adapted from Davis et al. (2011)).**

The main differences between this system and a conventional reinforced concrete footing-column-beam bent system are:

- the system has precast columns and beams.

- the system has a socket connection between the column and the cast-in-place footing, (Haraldsson et al. 2011) and a grouted duct connection to the precast crossbeam (Pang et al. 2008)
- the columns of this system contain unbonded prestressing tendons that encourage re-centering of the columns after an earthquake.
- the system uses Hybrid Fiber Reinforced Concrete (HyFRC), epoxy covered strands and (possibly) stainless-steel reinforcement.

The non-prestressed versions of the socket connection to the footing (Haraldsson et al., 2011) and the grouted duct connection to the precast crossbeam (Pang et al., 2008) have been shown by laboratory tests to provide good resistance to cyclic loading. The non-prestressed versions of these connections have also been deployed in the field (Khaleghi et al., 2012) and found to be easy to construct. The pre-tensioned column version (with conventional concrete) has been tested in the laboratory (Davis et al., 2011). While it provided the desired re-centering properties, spalling and bar buckling in the plastic-hinge region started at a lower drifts than in comparable non-prestressed columns.

The two tests described in this report were conducted to evaluate whether the inclusion of high-performance materials would improve the performance of the pretensioned, spread-footing connection (PreT-SF) tested by Davis et al. (2011). In this study, Specimen PreT-BS was tested with the same geometry and reinforcement as PreT-SF, but a shell of HyFRC was added to the plastic-hinge region. Specimen PreT-SS was nominally identical to PreT-BS with the exception that the conventional longitudinal bars ("Black Steel") were replaced with stainless-steel reinforcing bars.

## 1.1 Precast Columns and Beams for Accelerated Bridge Construction

Precasting columns and crossbeams has many advantages over casting them in place. One advantage is that precasting reduces the work that needs to be done on site. If less work is done on site, there will be fewer traffic delays and therefore, there will be fewer greenhouse gasses released to the atmosphere (Khaleghi et al., 2012), and less money will be wasted on gas. Precasting in a fabrication plant also makes it easier to ensure good quality control.

Structural elements have often been precast in the United States and elsewhere. For example, precast bridge girders have been used to accelerate bridge construction in Washington State for more than 50 years (Khaleghi et al., 2012). In contrast, bridge columns and beams have rarely been precast in

seismic areas. Such designs are challenging, because the locations at which the connections are most conveniently made (the beam-column interface) are also the locations with the highest force and deformation demands.

## 1.2 Socket Connections

The column-to-footing socket connection was developed at the University of Washington in collaboration with Berger/ABAM Engineers, Concrete Technology Corporation, Tri-State Construction and the Washington State Department of Transportation (WSDOT) (Haraldsson et al., 2011). Typical, cast-in-place columns are connected to other elements with continuous reinforcement that is anchored in the footing by bending it outwards. This configuration would make it hard to fit the column inside of the footing if the columns were precast and the footing has top steel. Having rebars sticking out of the columns would also make it harder to transport the columns from the precasting plant to construction site. Thus the columns were designed with straight longitudinal bars and anchor heads. Forces are transmitted from the precast column to the surrounding footing concrete by the concrete alone.

At the top of the column (Figure 1-2), the connection to the crossbeam features a small socket (Davis et al., 2011) and longitudinal bars grouted in ducts (Pang et al., 2009).

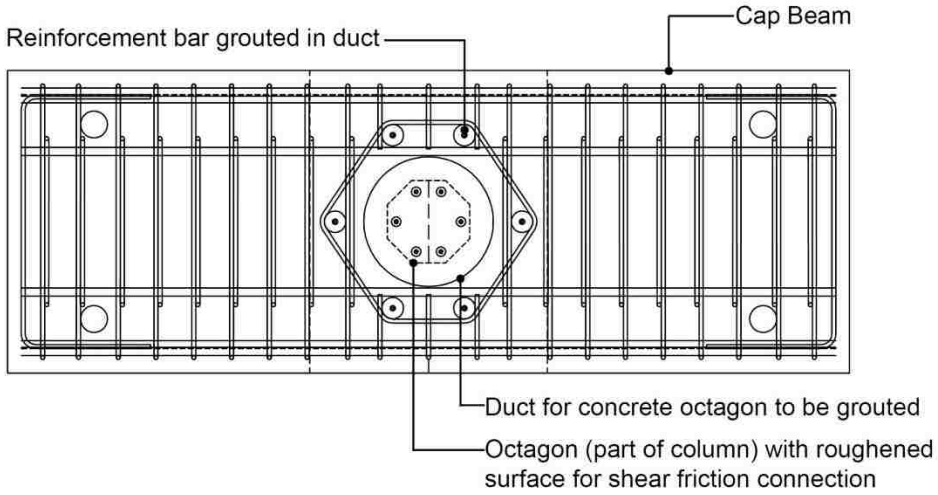


**Figure 1-2: Main parts of column to cap beam socket connection.**

Figure 1-3 shows the construction process of placing the columns in the footing using a socket connection. First the ground is excavated, and then the footing rebar is placed. When the footing rebar has been placed the columns are placed inside the footing rebar cage, and then the footing is cast. When

the footing concrete has gained sufficient strength, a precast crossbeam is then placed at the top of the columns using the grouted duct connection at top of the columns, designed by Pang et al. (2008) and Davis et al. (2011).

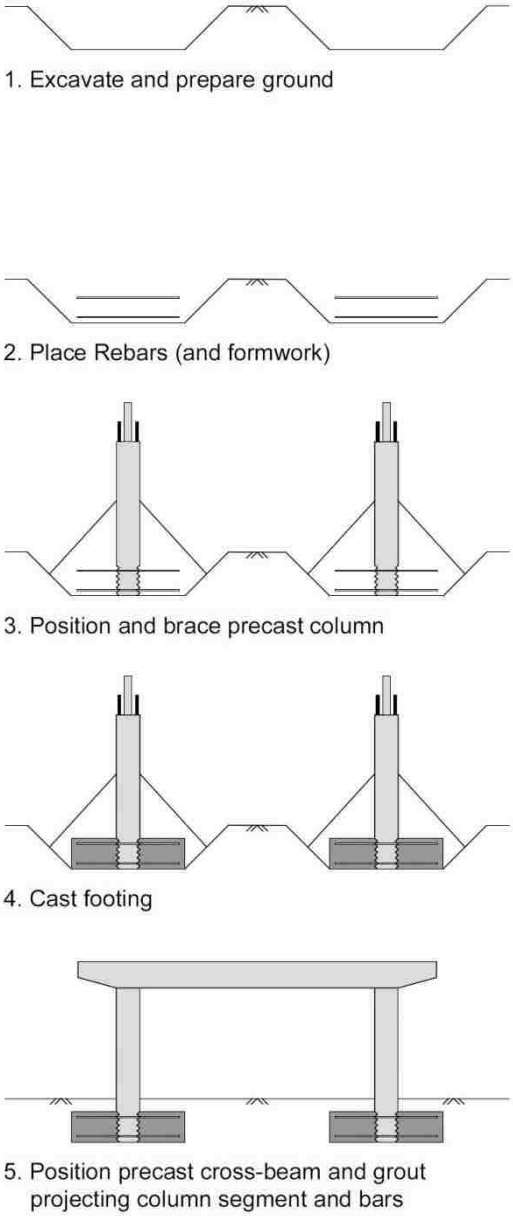


**Figure 1-3: The process of using socket connection to accelerate construction.**

## 1.3 Prestressing to Limit Residual Displacements

The proposed precast column system was designed to have earthquake resistance superior to that of traditional precast columns. Unbonded prestressing tendons have been used by researchers to

reduce residual displacements of systems after an earthquake, and therefore limit the repair cost (e.g., Cohagen et al., 2008). The rationale for debonding the prestressing tendons is to spread the deformations in the tendons over the unbonded length so the resulting strains will be small enough for the tendon to remain elastic. Since the tendons will remain elastic, they will tend to restore the element to its initial position.

When a material yields, it does not return to its original state after unloading. A reinforced concrete column responds similarly, and may display residual drift after cyclic loading on it stops. Figure 1-4 illustrates the benefits of including an unbonded prestressed element within a system. In a conventional reinforced concrete system (Figure 1-4 a) the system is loaded up to yielding point, up to maximum load and then unloaded. When the force is removed from the system, the displacement will not be zero. By continuing to load (in the opposite direction) the system the will yield again and when there is no displacement relative to the initial position of the system, the load is again not zero. If loading continues to maximum force and then releases, the displacement at zero load will not be zero relative to the initial displacement.

In a system with sufficient unbonded prestessing (Figure 1-4 b) the system will be loaded through yielding and up to maximum load. When it is unloaded, the unbonded tendons cause the unloading path to rejoin the loading path down to the origin. Thus, when the load is removed, the displacement returns to zero. The same behavior occurs in the opposite direction.

Prestressing tendons can either be pre-tensioned or post-tensioned. The proposed system is pre-tensioned, which requires that the prestressing strands be anchored to the concrete by bond alone. In contrast, post-tensioned tendons transfer their load to the concrete by mechanical anchors at the end of the tendons, so bond is unnecessary.

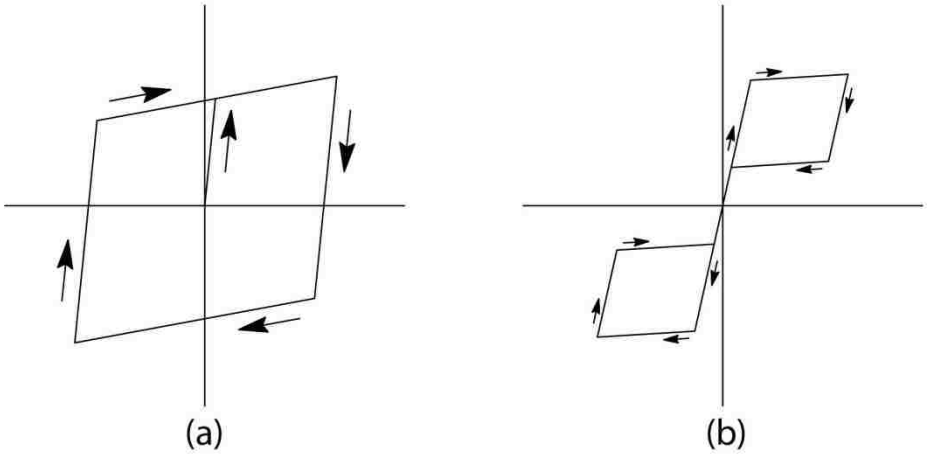


**Figure 1-4: Theoretical hysteresis loops for both traditional reinforced concrete system (a) and unbonded prestressed concrete system (b) (adapted from Stanton et al., 1997).**

Two concrete re-centering systems have been tested at the University of Washington, one by Cohagen et al. (2008) and one by Davis et al. (2011). The system tested by Cohagen was a reinforced concrete column that had one unbonded, post-tensioned bar in the middle of the column with mechanical anchorages at the ends. The system was connected to a cap beam, using both the unbonded post-tensioned bar and conventional deformed bar reinforcement configured with the large-bar-to-duct connection proposed by Pang et al. (2008). The system proposed by Cohagen showed improved re-centering compared with a non-prestressed column, as shown in Figure 1-5.

The system developed by Davis also showed improved re-centering, as shown in Figure 1-6. Davis used unbonded pre-tensioned strands to achieve the re-centering effect because the prestressing operation is done in a plant, off-site, thereby saving on-site construction time. Pre-tensioning also avoids the need for mechanical anchors, which are viewed by some as susceptible to corrosion. His columns showed better re-centering than Cohagen's column, but the concrete spalled earlier than expected. This was attributed to the fact that the concrete was conventional but experienced additional initial stress from the prestressing, and the longitudinal bars were smaller. The system proposed in this thesis is similar to the one tested by Davis, but it differs in that the conventional concrete in the plastic hinge region is replaced by a ductile concrete in order to delay spalling.

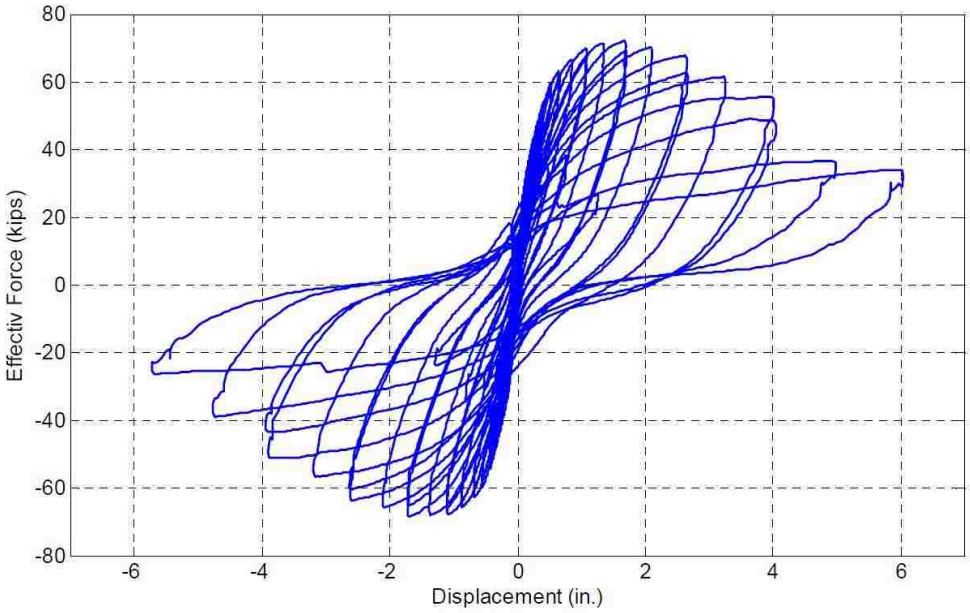


**Figure 1-5: Effective lateral force versus lateral displacement, Cohagen et al. (2008).**

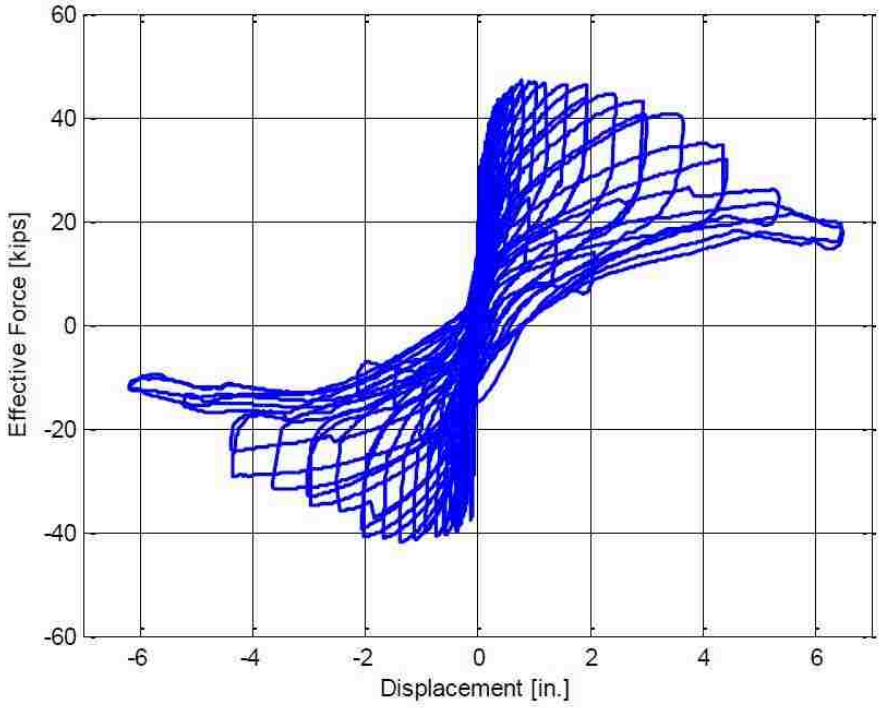


**Figure 1-6: Effective lateral force versus lateral displacement Davis et al. (2011).**

## 1.4 Hybrid Fiber Reinforced Concrete

The bent system that is evaluated in this thesis is intended to be an improved version of the systems developed by Davis et al. (2011). In Davis' columns, the concrete in the plastic hinge zone spalled much earlier than predicted by models based on the performance of conventional columns (Berry et al., 2004). For this research, high-performance concrete that is very ductile was added in those the places where maximum moment is expected, that is, at the column-footing interface at the bottom and at column-cap beam interface at the top.

The concrete is called Hybrid Fiber Reinforced Concrete (HyFRC), which was developed by Ostertag et al. (2012). The concrete is called Hybrid because it contains both steel fibers and polymer fibers. The fiber dosage is quite heavy. Detailed information on HyFRC is given in Section 2.2.3.

## 1.5 Stainless Steel

Ductility is usually of concern in seismic regions. Therefore to use stainless steel rebar was used for longitudinal reinforcement in one of the columns. The goal was to take advantage of the higher ductility provided by most stainless steel bars compared with conventional steel reinforcing bars (ASTM A706). Many alloys of stainless steel are available for rebars. For the systems proposed in this thesis, Type 2205 alloy was selected. More details on that alloy are provided in Section 2.2.1.

Another benefit of incorporating stainless steel in the columns is that stainless steel has corrosion resistance superior to that of conventional reinforcing steel. The additional corrosion resistance increases the life of the columns (Schnell et al., 2008) as does the use of epoxy coating on the prestressing strands. Better corrosion resistance is beneficial in all cases, but particularly in corrosive environments, such as marine locations or regions where de-icing salts are extensively used on the roadway.

# 2 Design of Test Specimens

The specimens tested here are the result of a long development process, supported by testing of many of the contributing components. The primary goal of the column design is to accelerate bridge construction. Bottom and top column connection concepts have been developed for the system and they make it possible to accelerate bridge construction. The second goal is to limit residual displacements. Unbonded pretensioning helps to limit residual displacements, but in the first laboratory tests (Davis et al 2012) it caused the concrete to spall earlier than expected. In the work described in this thesis, an HyFRC shell was added to the columns where maximum moment is expected in the columns with the objective of delaying spalling. It is expected to prevent concrete spalling since the HyFRC keeps its compressive strength longer and has higher tensile strength than regular concrete (Ostertag et al. 2013).

## 2.1 Geometry of the specimens

The columns tested here simulate prototype columns with an outside diameter of 48 in. (or 4 ft.). Due to size restrictions in the structures lab at the University of Washington the test specimens were scaled down to have an outside diameter of 20 in. Therefore the scale factor for the test specimens was 0.417 and all dimensions and material were scaled down by a number as close to the scale factor as possible.

The columns were octagonal in cross-section. This choice was made to simplify the formwork and the casting procedure. To facilitate pre-tensioning, the columns were cast horizontally, and the concrete was deposited through the open top of the form. The flat faces of the octagon made the formwork easier to build than if the shape had been circular, and the flat top of the concrete was easier to finish than a curved surface would be. These arguments would also hold true at full scale. Other shapes, such as square, would have been led to equal of greater simplicity in fabrication, but the octagon was preferred because it allows the use of spiral transverse reinforcement and its strength and stiffness are, for practical purposes, equal in all directions. The columns were reinforced with a combination of regular reinforcement bonded to the concrete and unbonded prestressing strands. The reason for choosing this combination was to have the regular reinforcement yield cyclically and dissipate energy while the unbonded prestressing strands remain elastic and re-center the column. To dissipate as much energy as possible and have maximum moment capacity the regular reinforcement was placed as close

to the outside of the column. The unbonded prestressing strands were placed as close to the center of the columns as possible because the geometry of the top connection requires that.

The configuration of the top and bottom connections to the columns permits accelerated bridge construction. The column-to-footing connection consists of only a roughened surface, with a saw-tooth detail, to transfer shear between the precast column and the spread footing concrete that is cast in place round it. No steel projects out of the bottom or sides of the column. Therefore it is much easier to transport the columns from a precasting plant to a construction site.

A top connection had already been developed for the pre-tensioned columns. It was tested by Davis et al. (2011) and the connection worked as well as the bottom connection, so this thesis only looks at the bottom connection.

Although the top connection is not of concern in this thesis it is useful to introduce the design concept for it, because it influences the configuration of the reinforcement. The configuration is governed by the fact that the cap beam is to be precast, which prevents the use of a socket connection similar to the bottom one. The strands in the columns should be unbonded over as long region as possible in the columns, which means that they should be bonded within the depth of the cap beam, which in turn implies the need for extending the precast column up into an opening in the cap beam. To minimize the size of that opening, and therefore the width and weight of the cap beam, the column section is reduced, as shown in Figure 2-1. This geometry also provides a shoulder on the column on which the cap beam can be set during erection, and obviates the need for column clamps.

The reduced column section is grouted into the opening in the cap beam, and the non-prestressed bars project up into ducts where they too are grouted. The grouted duct connection is similar to the large-bar concept tested by Pang et al. (2008), but the bars are likely to be smaller since some of the column's flexural resistance is provided by the prestressing strands and less bar steel is needed.

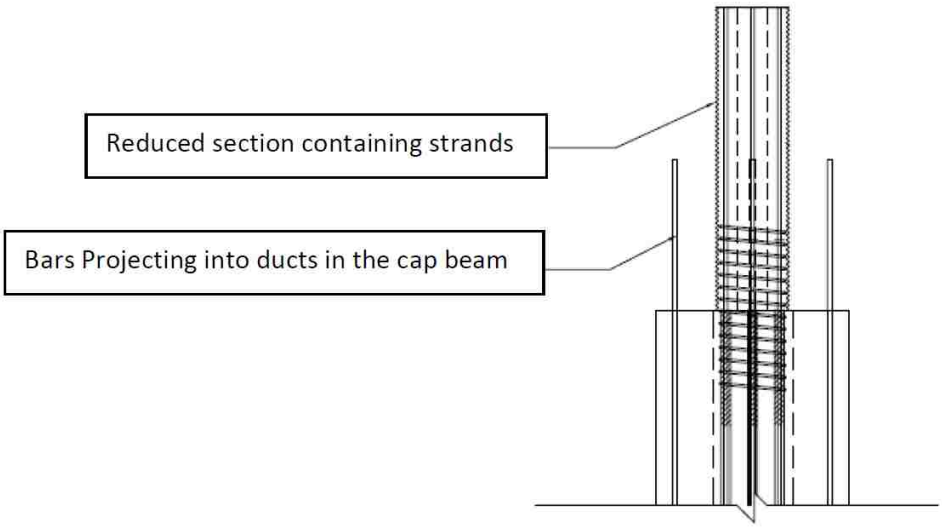


**Figure 2-1: Hybrid grouted socket connection, Davis et al. (2011).**

The unbonded pre-tensioning in the columns is intended to provide re-centering after an earthquake. The strands were bonded at the top and bottom of the column, as shown in Figure 2-3, and debonded in the central region by placing them in plastic sleeves. When the column is bent by transverse load, the strands elongate, but the deformation is spread over the whole unbonded length and causes a strain increment small enough that the strands remain elastic and thus provide an elastic restoring force. The column must also have sufficient strength in resisting transverse load and should dissipate as much energy as possible without jeopardizing the re-centering feature. The design variables to achieve these performance include the total area of strand and deformed bar, and the initial stress in the strands. For consistency with the previous tests conducted by Davis et al (2011), the reinforcement consisted of six 3/8" dia. epoxy-coated strands and six No. 4 deformed bars.

When the column is loaded laterally, the maximum moment and the highest compressive stress in the concrete occur at the bottom of the column. In previous experiments related to this thesis, the concrete spalled earlier than expected (Davis et al. 2011). That was probably because the prestressing increased the initial stress in the concrete beyond that caused by the applied axial load. It was therefore decided to use much more ductile concrete in the present columns, in the hopes that that would delay the onset of damage at the bottom of the column. The concrete used was the HyFRC mentioned before. Figure 2-2 compares shows the compressive stress-strain properties of the HyFRC with those of conventional concrete with comparable strength.

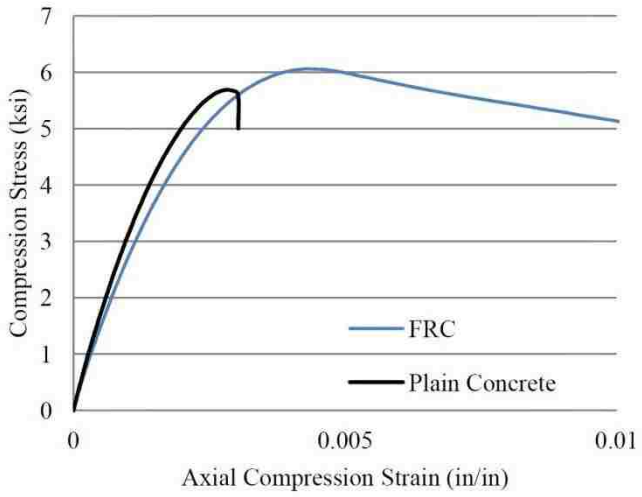


**Figure 2-2: Typical compression stress vs. axial compression strain for HyFRC compared to plain concrete, Ostertag et. al (2011).**

In a multi-column bent in the field, the column would have an inflection point at approximately mid-height. To facilitate testing, only the bottom half of the column was tested, as a cantilever. Structurally the two are equivalent, but, because the columns contain unbonded pre-tensioned strands, the detail at the inflection point has to be different. In the field, symmetry shows that, at mid-height, the strand will not slip relative to the surrounding concrete. Therefore in the test specimens the strand could be bonded there without influencing the behavior. However, anchoring the strands requires a finite distance, and in the test specimens the bonded region extended 12 inches below the inflection point. This meant that the unbonded length was slightly shorter than it would be in the field, which in turn meant that the strand would yield at a slightly smaller drift than it would in the field. The strands were bonded for anchorage for 24 $^{9}/_{16}$'' at the bottom and 24'' at the top. Figure 2-3 shows clearly that the test specimens had shorter unbonded region.

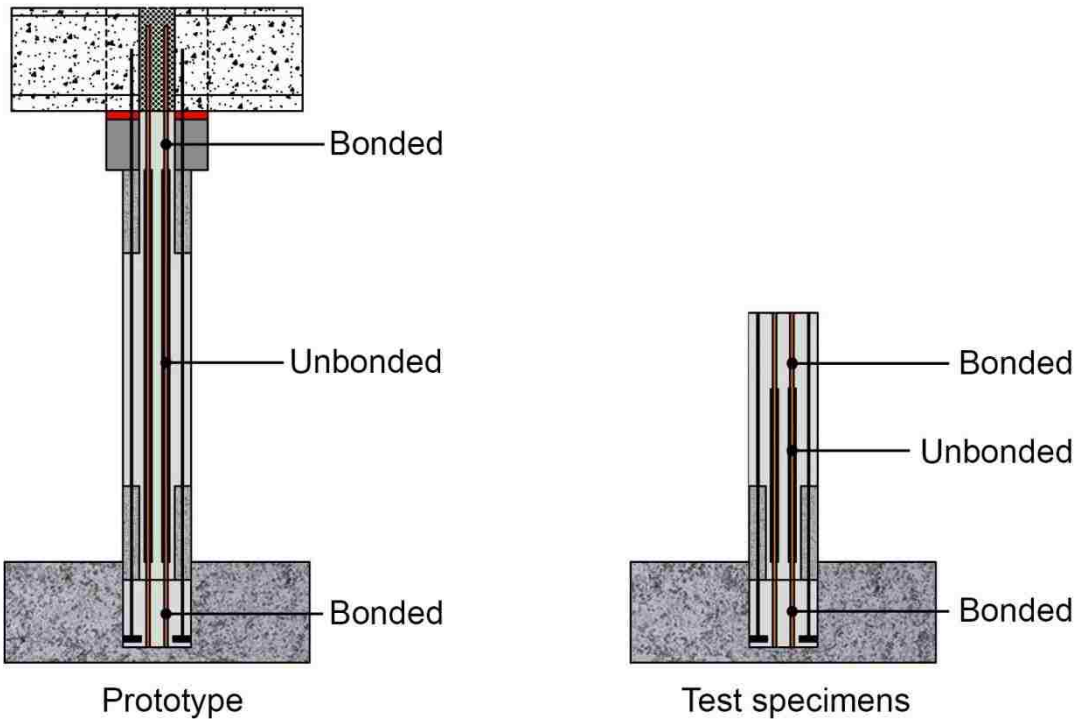


**Figure 2-3: Differences between the bonded regions in a column in the field and the test specimens (adapted from Davis (2011)).**

The bond requirements for the strand were also affected by the scale factor. The smallest epoxy-coated strand that was commercially available was 3/8" diameter, which corresponds to 0.90" diameter at prototype scale. Because full anchorage of the strand is critical but the available bond length is essentially limited to the depth of the cap beam or footing, the strand size should be chosen with bond in mind.

ACI 318-11 requires a development length of $150d_b$ if the strand has an effective stress, $f_{se}$, of 150 ksi. Then, to achieve anchorage within a typical 42" deep cap beam, the strand diameter should be no more than 42"/150 = 0.28". 0.25" strand is available, but a large number (60 to 100) strands would be needed in the prototype, and configuring them in the reduced section would be difficult. Thus, larger diameter strands would be needed for practical reasons, and bond testing would be necessary to demonstrate the adequacy of the anchorage because it would be less than $150d_b$ long. If ½" strand were to be used in the prototype, the available development length would be 84 $d_b$, and the corresponding diameter at laboratory scale would be 0.2083". The 3/8" diameter strand that was actually used is 1.8 times this size. This situation was undesirable, but unavoidable.

The consequence of using oversize strand in the tests is that the bond stresses would be higher than in the prototype and spurious bond failure would be possible. In order to prevent such failure, prestressing chucks were fitted onto the strands at each end of the column, as shown in Figure 2-4, after the release of the strands. To ensure that they were tight, a screw thread device was placed between them and the face of the column. It consisted of a 7/8" diameter ASTM A490 bolt with a hole drilled through middle. After the chuck was installed, the bolt was turned until it caused a load of approximately 4 kips in the strand. This load set the wedges in the chuck so that, if the strand lost bond in the test, the chucks would provide anchorage with almost no further strand movement. At one end of the column (the top) a strand load cell was placed between the screw thread device and the chuck. Any load change detected by the load cell would indicate slip in the bonded region, but the chucks would nonetheless anchor the strand and allow the test to continue.

**Figure 2-4: System to prevent the strands from fully slipping and losing prestressing.**

## 2.2 Materials

### 2.2.1 Reinforcement steel

The flexural strength of the column is provided by a combination of prestressing strand and deformed reinforcing bars. The columns were designed so that about 40% of the flexural strength would be provided by the bonded reinforcement bars and about 60% would be from the unbonded prestressing strands. Thus the cross-sectional area of deformed bar is less than in a conventional column, and was provided here by six #4 longitudinal bars to give a reinforcement ratio of $\rho_g = 0.36\%$. Using #4 bars in the test column is equivalent to using No. 10 bars in the field (since the specimens where scaled down by 0.417 scale factor). The bars are grouted into ducts in the cap beam. Pang et al. (2008) showed

that such large bars can be anchored reliably within the cap beam depth despite having a development length shorter than that required by ACI, because the confinement provided by the duct leads to improved bond.

All longitudinal rebar used in both the columns, except for the stainless steel described later, was ASTM A706 Gr. 60, as required for seismic design. For the footings, some #3 bars were needed and these were not available in A706, so A615 steel was used instead. The reduced ductility of A615 steel was expected to make no difference because the footing bars were expected to remain elastic. First, the footing is overdesigned, as described in Section 2.4 and second, most of the #3 rebar in the footing were in the top mat and the top mat was expected to be mainly in compression. The footing also had stirrups made from #3 rebar but previous tests showed that they would not yield in which case the reduced ductility would not affect response.

For shear reinforcement in the columns, spiral made from No. 3 gauge smooth steel wire was used. It has a cross-sectional area of $A_{wire}$ = 0.041 in$^2$. The spiral had an outer diameter of 18 $^5/_{16}$ in. so the smallest cover to the spiral (and therefore the reinforcement) was $^{13}/_{16}$ in. This corresponds to 2" clear cover to the spiral in the prototype. The pitch of the spiral was 1.25 in. center to center. The spiral was discontinuous just above the HyFRC shell (25" above column-footing interface) and was terminated , as required by ACI, by adding three closely spaced turns of spiral and bending the end in the core of the column. The same method was used at the top and bottom of the column to anchor the spiral.

One of the goals of this thesis was to evaluate the benefits of using of using stainless steel instead of regular "black" steel for the longitudinal reinforcement, and stainless steel was therefore used in one of the columns for two reasons. The first reason was that stainless steel is typically both more ductile and stronger than regular black steel (see later in this section). Yielding of longitudinal rebar is the main source of energy dissipation in the columns and it is improved by the higher levels of both strength and ductility of the stainless steel bars. The second reason why stainless steel was used is that it has superior corrosion resistance compared with regular steel. While this benefit would not be seen in the laboratory testing, it would be beneficial in the field.

For the stainless steel column everything except the longitudinal reinforcement was exactly the same as for the black steel column. Detailed information about the stainless steel used and other steel types investigated can be found in Appendix D.

Stainless steel bars are available in at least five alloys: ASTM A304LN, 316LN, XM-28 (sold commercially as Enduramet 32), XM-29 (sold commercially as Enduramet 33), and alloy 2205. The alloys all have higher strength and greater ductility than conventional ASTM A706 steel. They differ slightly in mechanical properties, and more widely in their corrosion-resistance and magnetic properties. Commercial availability and price emerged as two of the more important criteria, and Alloy 2205 proved to be the most readily available and economical. It offered good mechanical properties including low cyclic strain hardening, and was thus selected for use in this program.

Discussion with the bar manufacturer revealed that small diameter bars were commonly stored and shipped in coils, to be straightened on site prior to placement if necessary. Such small bars were expected to be used for spiral or other transverse reinforcement for which any lack of straightness would be unimportant. Coiled storage is commercially convenient, but necessarily introduces some plastic bending and would leave some residual curvature if the bars were straightened. Residual curvature risked affecting the onset of bar buckling in the present tests, so it was necessary to specify straight bars that had never been coiled. This issue was important at lab scale but, since large bars are not coiled, it would not be relevant at prototype scale.

### 2.2.2 Prestressing strands

Each column was prestressed with six epoxy coated strands. Epoxy coating increases the corrosion resistance of the strands.

The bond characteristics of the stand are important. Previous investigators (Cousins et al, 1990) tested the bond capacity of epoxy coated strand and compared it with that of bare “black” strand. Epoxy coating alone decreases the bond capacity of the strand, so manufacturers add fine silica sand to improve it. Cousins et al. (1990) were able to test strands with three different grit levels (described as light, medium and heavy). In general, more grit provided better bond.

Commercial availability was investigated. It was found that only two US manufacturers make epoxy-coated strand (Sumiden and RAIL-CO International), because it is a patented item and the market is anyway small, so availability is not good, especially for the small size (3/8”) needed for these tests. Furthermore, those manufacturers make only one level of grit impregnation today. The grit is applied by a manual process and is therefore subject to variability both along any one strand and from strand to strand, and no ASTM exists to govern it. For this reason, samples of the strand that was obtained were tested for bond in a separate investigation and were reported by Jimenez (2012).

Bond of black strand has been an ongoing problem in the pre-tensioning industry for approximately 20 years. The primary problem has been large variations in bond capacity among strand manufacturers. While the great majority provides bond that leads to transfer lengths equal to or less than that specified by ACI, a few samples have proved unsatisfactory. Consequently the North American Strand Producers' Association (NASP) has developed a strict testing protocol for acceptance testing of strand. It is based on testing ½" diameter black strand embedded in grout cylinders.

Jimenez (2012) followed that protocol as closely as possible in his tests on the 3/8" epoxy-coated strand used here. NASP specifies that the bond be evaluated at a front slip of the strand relative to the grout cylinder of 0.1". However, additional measurements were made at a slip of 0.02", because, for the short unbonded length used in these tests, 0.1" slip corresponds to a change in stress of approximately 60 ksi.

Jimenez found considerable scatter in his results. He also found that the peak bond force was not reached until a slip of approximately 0.5" in many cases. In the columns used here that slip would cause the loss of all of the prestress, so the peak bond force was considered an inappropriate characteristic. Overall, Jimenez found that epoxy coated strand had a higher bond peak strength than that of black strand (but at very large slip values), and a bond strength at low slip values (0.02" and 0.1") that was very close to that of black strand. The low-slip bond capacity values were in fact slightly less than those for black strand but the difference lay within the scatter band. Thus they were treated as being the same.

In conventional prestressed systems, the strand is usually stressed to the highest permissible stress in the interests of economy. The stress is usually limited by the jacking stress, which is typically $0.75f_{pu}$. However, in the pre-tensioned columns used here, the drift at first yield of the strands is directly related to the initial stress, because the strand experiences additional stress due to column bending that is approximately proportional to drift. Therefore the initial stress should be chosen based on the yield drift desired. Here the target initial stress was 170 ksi, which was intended to provide a yield drift of 3% (Davis et al. 2011). The additional 80 ksi required to bring the strands to yield would add approximately 40 kips to the axial force on the concrete.

### 2.2.3 HyFRC

The column used both conventional concrete and HyFRC. Relative to conventional concrete, HyFRC has better tensile properties and better ductility in compression because of the fibers in it. It is

also much more expensive and less workable in the fresh state, so it was used only in the plastic hinge region where its superior mechanical properties would be advantageous. That was achieved by first casting a hollow octagonal section, or shell, of HyFRC, 29 inches long, as shown in Figure 2-5. When that had gained strength it was placed in the main column form, and the remainder of the column was cast using conventional concrete.

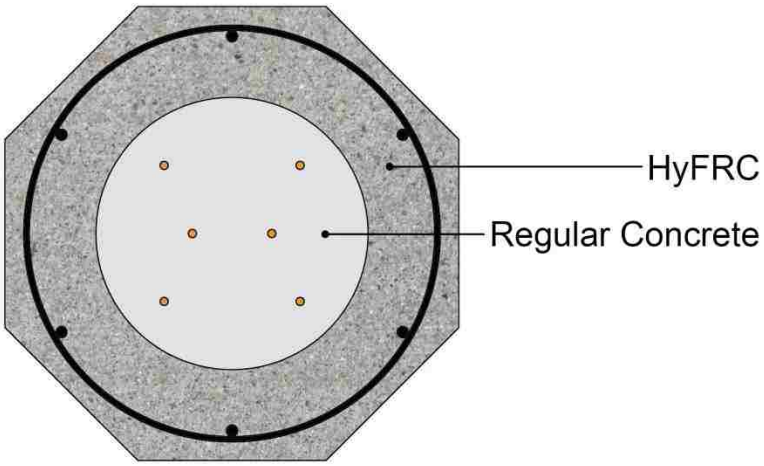


**Figure 2-5: Section through the column at the level of the HyFRC shell.**

The word "hybrid" in the name indicates that two types of fiber, steel and polymer, are used in the concrete. The purpose is to optimize the mechanical properties. The steel fibers are shown in Figure 2-6, and were Dramix ZP 305 produced by Bekaert (2010). The fibers are 30 mm long (or 1.18 in.), have a diameter of 0.55 mm (0.02 in.) and have one hook on each end of every fiber. The tensile strength of the fibers is 1,345 N/mm$^2$ (195 ksi) and the Young's modulus is 210,000 N/mm$^2$ (30,500 ksi). The dosage was 4.4% by weight. This is much heavier than in typical fiber-reinforced concretes, where dosages of about 1% by weight are the norm. 4.4% by weight results in approximately 1.3% by volume. If the fibers are oriented randomly, it can be shown that the fibers confer on the concrete a tensile strength of

$$f_t = 0.125\rho_v f_y \qquad \textbf{2-1}$$

where $f_t$ = effective tensile strength of concrete

$f_y$ = yield strength of steel fiber

$\rho_v$ = volumetric ratio of fibers

Using $\rho_v$ = 0.013 and $f_y$ = 195 ksi, the contribution of the fibers to $f_t$ is predicted to be 0.317.

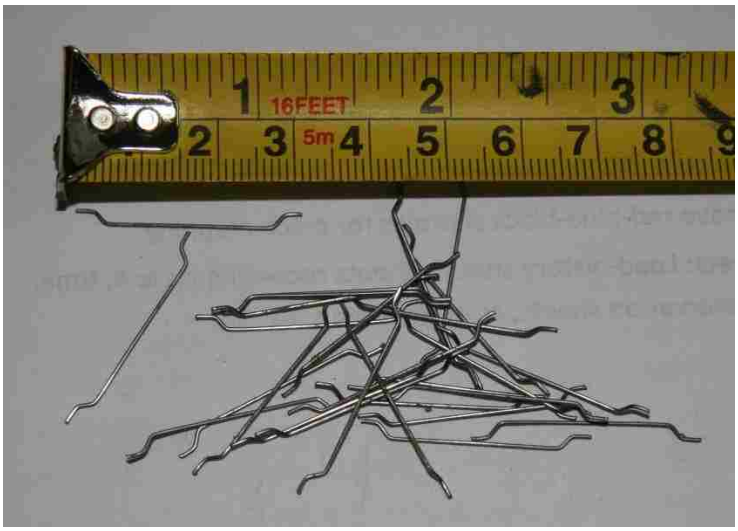


**Figure 2-6: Dramix ZP 305 steel fibers.**

The polymer fibers were Kuralon RECS 15x8mm. Their function was to make the concrete more ductile and to minimize crack opening. They were much smaller than the steel fibers, both in diameter and length. The length of each fiber was 8 mm (0.31 in.) but the diameter was very small. The amount of polymer fibers in the HyFRC was only 0.1 % of the total weight of the mix. The tensile strength of the fibers is 1,300 N/mm$^2$ (190 ksi)and the Young's modulus is 40,000 N/mm$^2$ (5,800 ksi), (Kuraray 2012).


**Figure 2-7: Kuralon RECS 15x8mm polymer fibers.**

The mix for the HyFRC consisted of both regular cement, type 1/type 2, and fly ash. Both the cement and the fly ash provide strength to the concrete paste that binds all the aggregate together. The

cement gives the mix strength more quickly. The fly ash, which is a byproduct from coal production, gives the paste strength slower than does cement. Figure 2-8 shows the strength gain of the HyFRC over time.

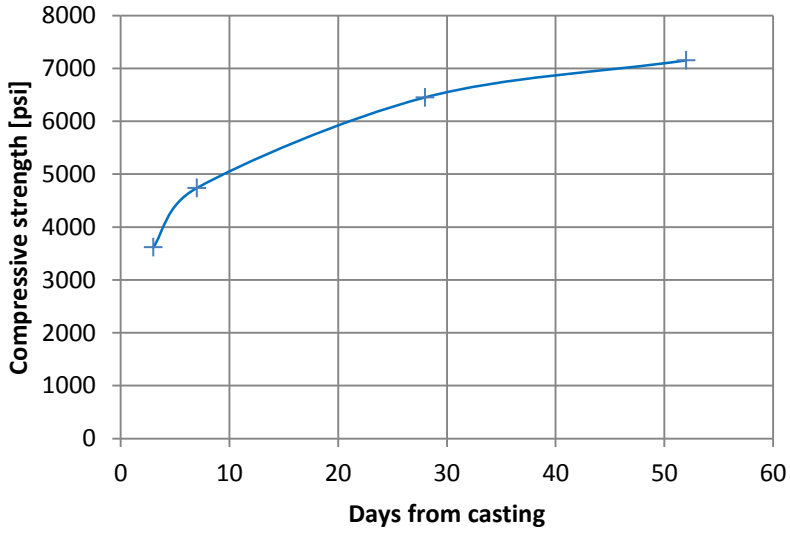


**Figure 2-8: Strength gaining of batch #5 of the HyFRC.**

### 2.2.4 Concrete

The concrete was supplied by CalPortland, a local readymix company. The mix is given in Table 2-1, and the goals were to achieve a slump of 7.0 inches and a compressive strength of 5,000 psi when the tendons were released. Data on the strength gain with time can be seen in Appendix A.

**Table 2-1: Design mix for one cubic yard of concrete used for both column and footings.**

| Material | Design Quanity |
|---|---|
| Fine Aggregate | 1250 lb |
| Pea Gravel | 1980 lb |
| Cement Type I/II | 752 lb |
| Water | 240.0 lb |
| Water Reduce Admixture | 30.00 oz |
| High-Range Water Reducer | 30.00 oz |

The columns and footings were cast in separate batches. Some difficulty was experienced with the column concrete because it started to set before casting was complete. This was due partly to the mix design, partly to the fact that the truck was delayed on the way to the site and partly to the difficulty of casting the columns with their tight spiral spacing. The design mix had the mix code 0171 (at

CalPortland) and the design water cement ratio was 0.319. However, all the concrete reached strength of at least 6000 psi at release, which easily exceeded the design value of 5000 psi.

## 2.3 Detailed Design of the Socket Connection

The socket connection was developed by Haraldsson et al. (2011). The connection makes it possible to accelerate bridge construction since by using this connection it is possible to prefabricate columns in a fabric and simply ship the columns to site and cast the foundation around the column.

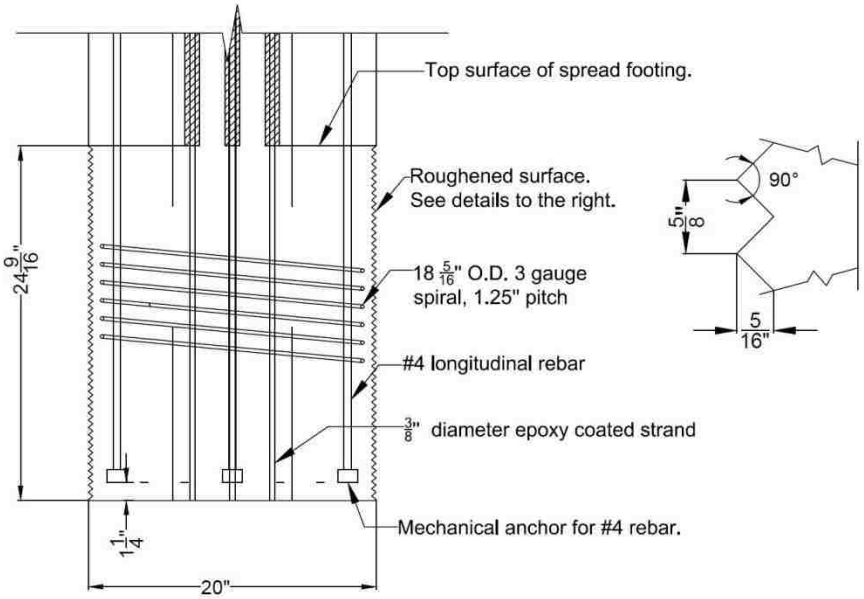


**Figure 2-9: Details of the socket connection.**

Since the footing was cast around the column the only thing that connects the column to the footing was the roughened surface at the bottom of the column. Haraldsson et al. (2011) showed that this connection works very well. Since the longitudinal rebar was not bent out of the column other means of anchorage were needed. Therefore Erico Lenton terminator heads were put on the end of every longitudinal rebar. A strut and tie model shows that the heads help to transfer the internal force from the diagonal strut in the column to the vertical tension reinforcement by means of a CCC node. Such nodes are extremely stable and lead to excellent behavior.

Other details of the connection can best be seen in Figure 2-9.

## 2.4 Detailed Design of the Spread Footing

The design of the spread footing was almost exactly the same as used by Davis et al. (2011) specimen PreT-SF. This footing was designed according to the AASHTO Load and Resistance Factor Design Specification (2009), the AASHTO Guide Specifications for LRFD Seismic Design (2009), the WSDOT Bridge Design Manual (2008) and the Caltrans Seismic Design Criteria (2006) (Haraldsson et al. 2011). The reinforcing layout of the top mat can be seen in Figure 2-10, the detailed drawings of the footing can be found in Appendix B.

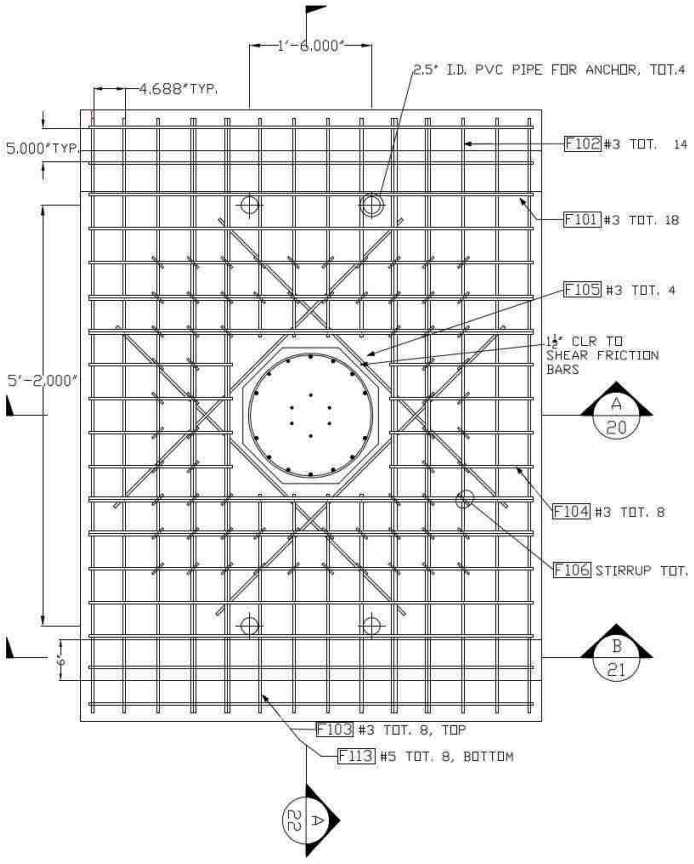


**Figure 2-10: Detailed drawing of the top steel of the footing.**

The footings were almost identical to the ones built by Davis et al. (2011). The first difference was that the footing was thicker overall, because the column had to be raised higher above the base block of the test rig to accommodate the modified (and longer) strand anchorage devices on the end of the column. The thickness of the concrete surrounding the column was the same but the void under the center of the block was higher. The second difference concerned the details of the steel plate in the

bottom of the footing that transferred shear force from the footing to the base block. Since the force was in fact all transferred by friction, those details served only as back-up and were never activated.

## 2.5 Construction of Specimens

Both specimens were constructed in the Structural Laboratory at the University of Washington. For each column, the HyFRC shell was cast first in a separate form. This was necessary because the main column was to be cast horizontally to facilitate prestressing, whereas the shell needed to be cast vertically in order for the HyFRC to flow properly into the shell form. (The shell wall was only 4" thick, but it contained spiral steel at 1.25" pitch, longitudinal rebar and inserts for instrumentation. The anticipated poor flow properties of the HyFRC and the small spacing between spiral turns were expected to make filling the forms and consolidating the material difficult.) The shell forms also had to be made to tight dimensional tolerances to ensure that the shell would fit correctly in the main form.

The HyFRC was designed to be self-consolidating, but this property was not achieved, because the workers had a little experience with this mix. Thus the design batch quantities of superplasticizer (SP) and Viscosity Modifying Admixture (VMA) were modified to achieve good flow. When the concrete was cast its workability was very good and depositing the concrete into the shell forms was relatively easy.

The available drum mixers were too small to make all the HyFRC in a single batch, so it was necessary to mix it in five batches. The three day strength tests revealed a large difference in strength between Batch #1 and Batch #5. The difference was attributed to two causes. First, the materials for Batch #5 were the first to be weighed and took gravel and sand from top of the barrels, where the materials were driest. Second, Batch #5 was the last to be mixed, so more water from the aggregates would have evaporated than in the lower numbered batches.

The HyFRC shell for the black steel column was mainly made up Batch #1 and Batch #2, only about 10% of Batch #3 (and only the top of the shell). The for the stainless steel column was made mostly out of batches #3 and #4 and 20% of the shell was from batch #5. So the HyFRC in the stainless steel shell was expected to be stronger than the material in the other shell. The fact that Batch #5 had 18 cylinders, but each of the others had only 3, made the testing procedure difficult. Every testing day of the HyFRC batch #5 was tested and the results from that batch were used to calibrate the results of the other batches.

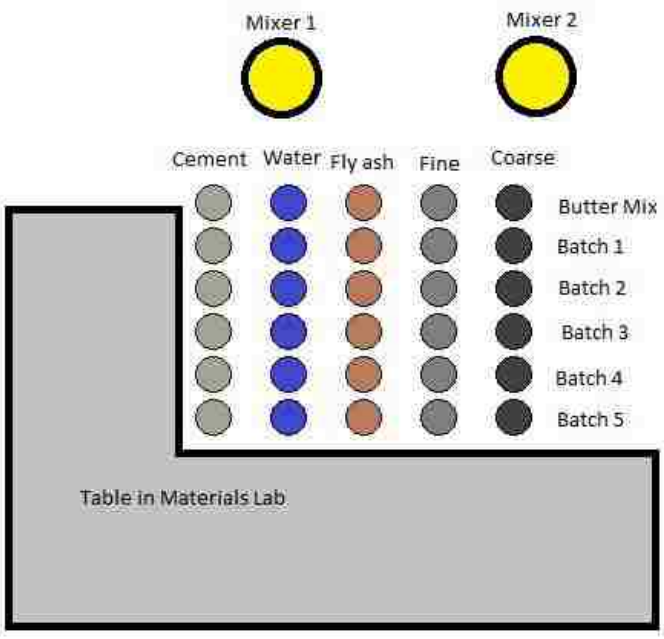


**Figure 2-11: Lineup of batches. Batch #1 mixed first, then Batch #2 and so on.**

In the mid-height region of the column, all of the strands were unbonded to the concrete so the strands would remain elastic and provide a restoring force so the column would re-center itself. The strands were bonded for 2 ft. at the top and 2 ft. and $^{9}/_{16}$ in. at the bottom of the column. The central unbonded region was 4 ft. 6 in. long.

**Figure 2-12: Strands prepared for stressing. Epoxy coating taken off so chucks can grip safely to strand.**

In both of the columns the strands were put in the column in a special pattern, shown in Figure 2-13. The pattern was dictated by the hole pattern in the stressing plates of the prestressing bed. That pattern had been chosen to minimize the space used by an 8-strand pattern, while maintaining a center-to-center distance between strands of about 3 in. That spacing was governed by the need for special hardware on the ends of the strands. The pattern of the strands was different to the one used by Davis et al. (2012). Those columns were made in a different facility and used a traditional circular strand pattern.

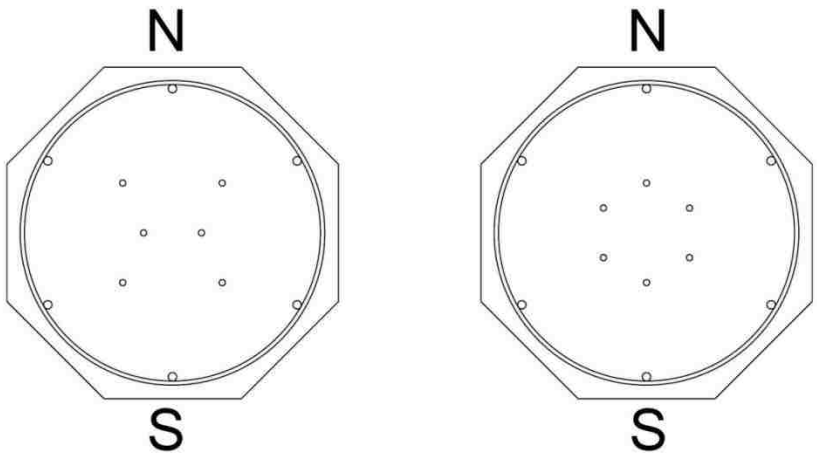


**Figure 2-13: Strand patterns for the present columns (left) and Davis' columns (right).**

The strands were stressed individually by using a 100 kip hydraulic ram powered by an electric pump. The goal was to jack each strand to 14.4 kips, corresponding to 170 ksi. Immediately after seating the chucks, the average force in each strand was 14.48 kips.

The columns were stressed at two different days; therefore the compressive strength of the concrete was collected twice since the column concrete was so young. Since the HyFRC was about 50 days when the columns were stressed it was decided only to collect data on the compressive strength once. Since the cross section of the columns was 20 in. diameter octagon the total area of column was 331.4 $in^2$. Remembering that the minimum thickness of the HyFRC shell was 4 in. it can be calculated that the area of HyFRC in the cross section was 218.3 $in^2$ therefore the area of the regular concrete in the plastic hinge region was 113.1 $in^2$.

The properties of the HyFRC and conventional concrete and the geometry for the column were used to estimate the elastic shortening loss at 2.2 ksi. The shrinkage loss was assumed to be the same 9

ksi as taken by Davis (based on 300 $\mu\varepsilon$ free shrinkage strain), and the creep loss of 4.4 ksi was taken as twice the elastic shortening loss. Thus the total losses are as shown in Table 2-2.

**Table 2-2: Loss factors of prestressing.**

| **Loss factor** | **Stress loss [ksi]** |
|---|---|
| Elastic shortening | 2.2 |
| Shrinkage | 9.0 |
| Creep | 4.4 |
| Total loss | **15.6** |
| Loss per strand | **2.6** |

From Table 2-2 and the initial stress in each strand the stress after every loss factor the final stress in the strand could be calculated. The result for the final force was 14.26 kips per strand. And therefore a stress of 167.8 ksi per strand.

The results on stress calculations are presented in Table 2-3.

**Table 2-3: Stresses after releasing prestressing strands, $f_c'$ uses average strength of batches and batches are scaled from batch #5.**

| Column | Part of conlumn | $f_c'$ [psi] | $E_c$ [ksi] | $E_{c,meas.}$ [ksi] | Stress after stressing [psi] |
|---|---|---|---|---|---|
| Black steel column | HyFRC shell | 5353.7 | 4170.6 | 4688 | 170.1 |
| | Concrete inside of HyFRC | 5289.4 | 4145.5 | 2894 | 88.1 |
| | Above/below HyFRC shell | | | | 258.2 |
| Stainless steel column | HyFRC shell | 6407.1 | 4562.5 | 4306 | 170.1 |
| | Concrete inside of HyFRC | 5406.3 | 4191.1 | 2911 | 88.1 |
| | Above/below HyFRC shell | | | | 258.2 |

**Figure 2-14: Strands stressed inside the HyFRC shells, ready for casting.**

Both columns were cast at the same time. The columns were cast inside the prestressing rig seen in Figure 2-14 and the forms were filled directly from a concrete truck. Since the HyFRC shells were pre-positioned in the column forms, the conventional concrete had to flow into the void in the center of the shells. To be sure that the concrete had filled up the void in the HyFRC shell, a small bleed vent was made through the shell wall on the top through which the height of the concrete could be detected.

The strands were released after the concrete had cured for a week. After the release of the strands the STDs, load cells and chucks were placed on the ends of the column. Then the columns were removed from the stressing rig and erected and braced in the footing forms. The two specimen footings were planned to be cast from a single truck, but were in fact cast separately. That was mainly because when the concrete arrived it had started to cure. The measured slump was much lower than the design slump. The footing for PreT-BS was cast with the partly cured concrete but the concrete had cured so much it was decided to get another truck later (to cast the PreT-SS footing). When the PreT-SS footing was cast a retarder was added to the concrete to delay the curing of the concrete. Casting the second column was much smoother and the concrete was workable all the time during the casting. That was not only because the retarder was added, it was also because the second concrete truck driver was more experienced and took less time to arrive at the Structural Laboratory at the laboratory.

# 3 Experimental Setup

This chapter describes the test setup (Section 3.1), instrumentation (Section 3.2), and testing protocol (Section 3.3) for the two subassembly tests.

## 3.1 Test Setup

The loading configuration for both tests is shown in Figure 3-1.

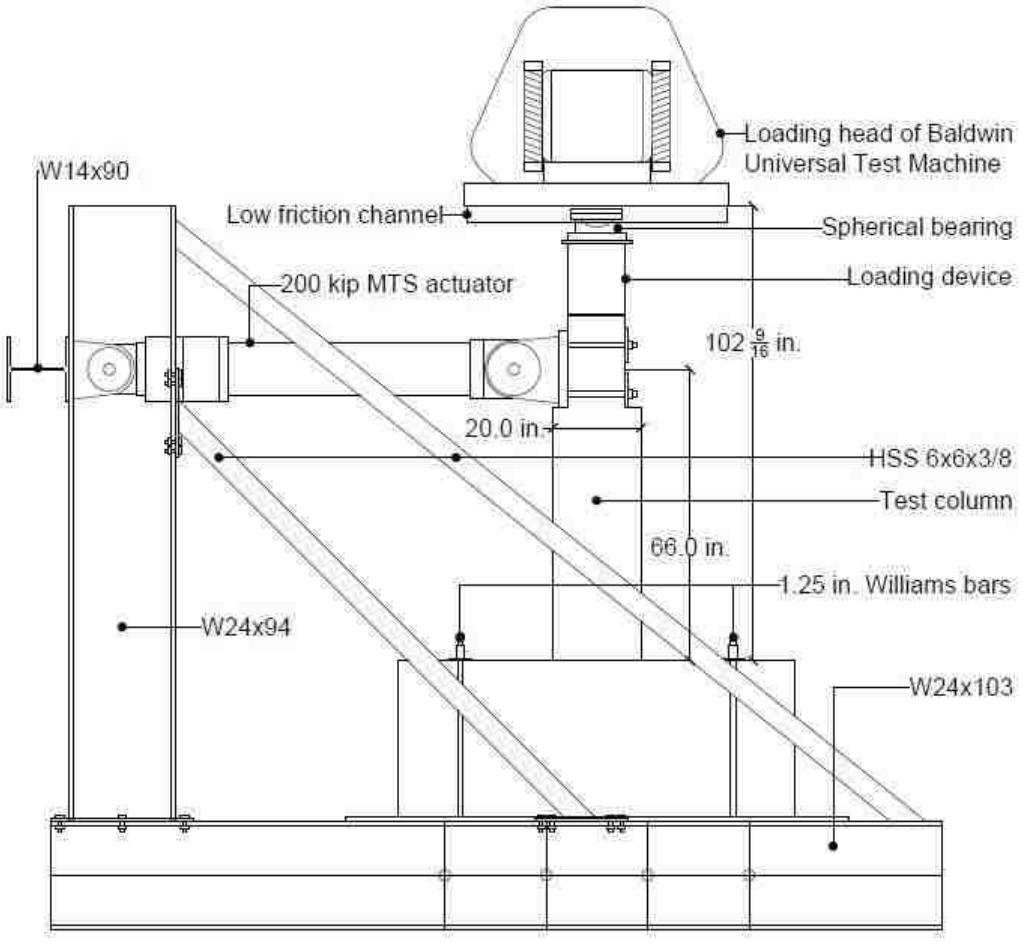


**Figure 3-1: Testing rig.**

The columns were subjected to a constant vertical load and cyclic horizontal loads. The vertical load was provided by the laboratory's 2.4-million-pound Baldwin Universal Test Machine. The horizontal load was applied by a 220-kip capacity MTS actuator bolted to a self-reacting steel reaction frame, which was attached to a large concrete base block. The specimens were anchored to the block using four 1.25-in. diameter Williams bars, each stressed to 100 kips.

Each specimen was placed on the concrete block, centered and leveled. Hydro-stone (a high-strength gypsum plaster) was then poured under the specimens to ensure that all of the footing was in touch with concrete block.

To transfer the axial load from the Baldwin Universal Testing Machine to the column a special loading cylinder had to be used since the strands were sticking out of the ends of the columns, along with the screw threading device (STD), load cells and pre-stressing chucks (Figure 3-2). The loading device consists of a circular steel tube (with 12 in. inner diameter and 0.5 in. thick). To transfer the vertical load, 16 in. x 16 in. x 7/8 in. steel plate was welded on top of the cylinder. To accommodate rotation of the column, a spherical bearing was placed on the steel plate. To minimize friction and to ensure that the column moved in the desired vertical plane, the top of the bearing contained a greased PTFE pad that slid against a stainless steel sheet placed inside steel channel that was attached to the head of the Baldwin Universal Testing Machine.

**Figure 3-2: Strand slip detecting setup (left) and the setup covered by the vertical loading device (right).**

The MTS actuator was attached to the column using four 1-in. diameter threaded rods. To ensure that the actuator was always tightly packed against the column, the threaded rods were prestressed to 15 kips. The stroke of the 200-k actuator was two feet.

## 3.2 Instrumentation

The specimen instrumentation is summarized in Table 3-1.

**Table 3-1: Instrumentation summary.**

| Instrument | Measured response | Number used |
|---|---|---|
| Strand load cell | Detect slip in strands | 6 |
| MTS load cell | Horizontal load | 1 |
| Baldwin load cell | Axial load | 1 |
| Linear potentiometer | Horizontal and vertical movement<br>Rotation w/ curvature rods | 11 |
| String potentiometer | Horizontal displacements | 5 |
| Linear variable differential transformer | Deflection of testing rig | 1 |
| Inclinometer | Rotation of specimen | 4 |
| 2-wire strain gauge | Strain in reinforcement steel | 20 |
| 3-wire strain gauge | Strain in pre-stressing stands | 12 |

Figure 3-3 shows the locations of each external instrument (internal strain gauges not shown). In Figure 3-3, items 1-11 are linear potentiometer, items 12-16 are string potentiometers, 17 is the Baldwin load cell, 18 is the MTS load cell, 19 is the linear variable differential transformer and 20-23 are inclinometers.

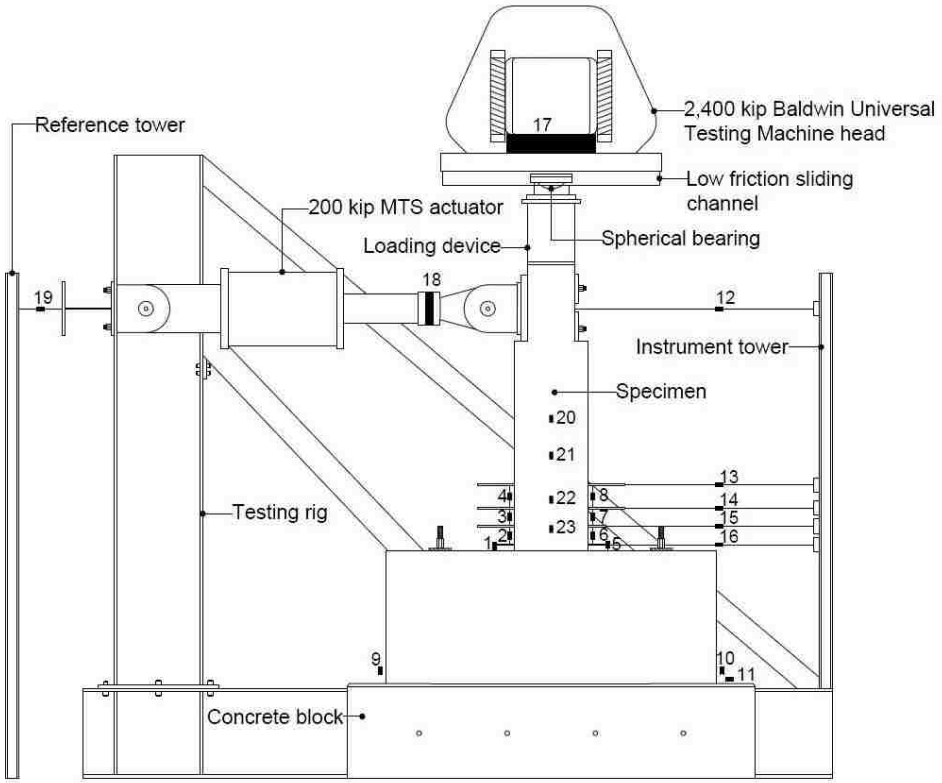


**Figure 3-3: Instrumentation setup.**

### 3.2.1 Applied Loads

The vertical load from the Baldwin and the horizontal load from the MTS actuator were measured using internal load cells in both devices.

### 3.2.2 Strain Gauges

Strain gauges were used to measure strains in the longitudinal steel, transverse steel and the prestressing strands. The strain gauge configuration (Figure 3-4) was the same for both columns. Both 2-wire and 3-wire gauges were used during the test. It would have been preferable to use only 3-wire strain gauges, because the 3-wire gauges are less sensitive to temperature changes. The 2-wire gauges were used in some locations, because they were immediately available, whereas the delivery time for the 3-wire gauges was longer than expected.

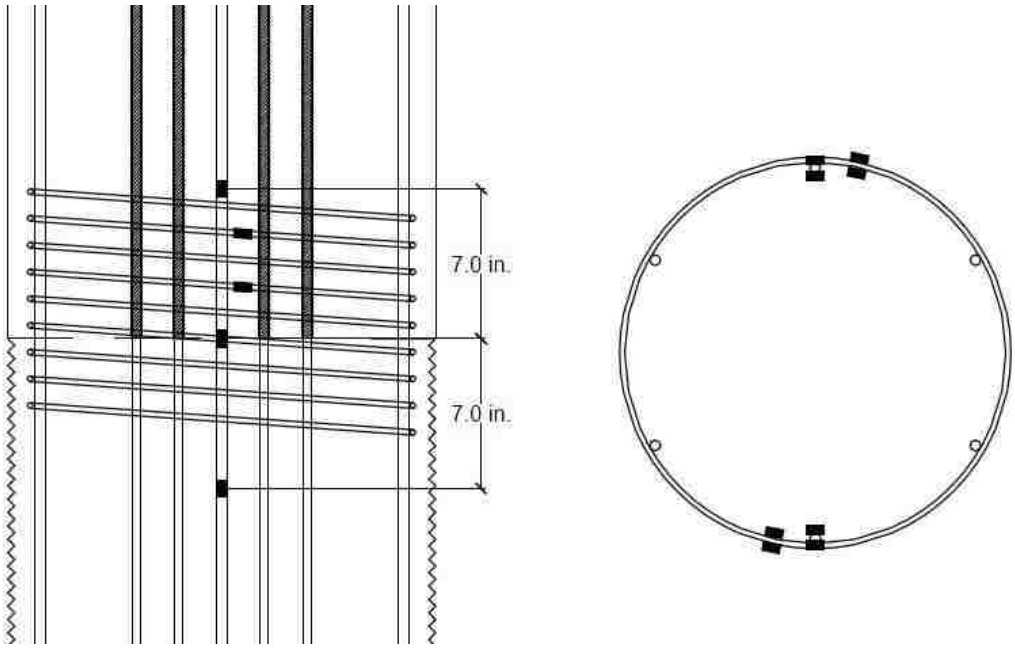


**Figure 3-4: Strain gauge setup. Figure only shows 2-wire gauges. Middle strain gauge pairs on longitudinal reinforcement bars are on the column-footing intersection.**

Two-wire gauges were placed on the longitudinal reinforcement at the column-to-footing interface, 7 in. above the interface, and 7 in. below the interface. At each location, pairs of strain gages were placed on the North and South bars (total of 12 gauges). The gauges above the column-footing intersection were placed to monitor the strain distribution over the length of the longitudinal rebar within the column. The pair 7 in. below the interface was placed there to verify that the longitudinal reinforcement was anchored within the footing, even before the anchor heads were activated.

Two pairs of two-wire gages were placed on the spiral reinforcement on each side of the column at two elevations (total of 8 gages). The two lower pairs were placed (at about 3 in. above the interface) to measure the strains where the longitudinal rebar was likely to buckle. The higher pair was placed 2.5 in. above the lower pair to measure the strains in the spiral and detect if buckling occurred higher than expected.

To monitor strand strain, 3-wire strain gauges were placed on the unbounded region of the pre-stressing strands, near the middles of the unbounded region. The 3-wire gauges were designed to be placed on pre-stressing stands, so the gauge itself is smaller than a gauge for regular rebar.

### 3.2.3 Load Cells on Pre-Stressing Strands

To measure if slip occurred in the strands, load cells were placed at the end of the strands at the top of each column, as shown in Figure 3-5. The anchorage length of the strands were a little bit longer at the bottom of the columns than the top, so slip was less likely to occur at the bottom, so no load cells were placed there.

The same strand load cells were used when the pre-stressing strands were stressed. When the columns had been cast and the strands were released to transfer the stress in the strands to the column, concrete chucks were placed at both ends of the columns on top of the STD. On the top of the columns load cells were placed between the STD and the strand chucks. The bolts in the STD were twisted to touch the load cells, and the goal was to place a force in the part of the strands above the top of the column close to 5 kips. This load was applied to ensure that the STD, load cells and the strand chucks were tightly packed together. These load cells would then detect any potential slipping in the strands.

**Figure 3-5: System of STD, strand load cells and strand chucks on top of one specimen.**

### 3.2.4 Curvature Rod System

A curvature rod system was used to measure relative rotations of the columns. The setup of the system can be seen in Figure 3-6 (the setup was the same on both sides of the column). The lowest linear potentiometer measured the changes in distance between the column-footing interface and the lowest threaded rod. The other linear potentiometers measured the change in lengths between pairs of threaded rods.

The threaded rods were placed in a vertical line. The lowest rod was placed 1.5 in. from the column-footing interface, the second lowest 6.75 in. from the interface, the third lowest 11.75 in. from the interface and the highest rod 17.5 in. from the interface. To be able to fit the curvature rods between the spiral reinforcement, the height where the coupler for the threaded rod was placed had to be adjusted when it interfered with a spiral. Four linear potentiometers where used on each curvature rod system on both sides of columns, resulting in a total of eight potentiometers for the curvature rod system.

**Figure 3-6: Curvature rod tracking system.**

### 3.2.5 Potentiometers to Measure Specimen Displacement

Both linear potentiometers and string potentiometers were used to measure displacements of the specimen. The linear potentiometer had a plastic plunger sticking out of the main part of the device, whose movement was measured by the device. The string potentiometers on the other hand had a string on a drum attached to a circular spring, and the string could be dragged out of the main part of the string potentiometer. The potentiometer measured how much the string is extended in each direction. The string potentiometers can measure larger displacements, whereas the linear potentiometers are better suited for measuring smaller length changes.

**Figure 3-7: Linear potentiometer**

**Figure 3-8: String potentiometer**

The setup of the potentiometers can be seen in Figure 3-3. The instrumentation tower shouldn't have moved when the tests were performed, because the tower was only attached to the specimen through the string potentiometers. One of the string potentiometers was attached to the middle of the reaction region (where the MTS actuator was attached to the specimens).

Linear potentiometers were also used to see if the specimens (column and footing) was sliding or rocking. Vertically placed linear potentiometers were used to detect rocking and the horizontal one to detect sliding of the specimens.

### 3.2.6 Linear Variable Differential Transformer

Only one linear variable differential transformer (LVDT) was used for each specimen. The LVDT is more accurate than the linear potentiometer and therefore it was decided to use a LVDT to measure how much the testing rig deformed during testing. That was done because the displacements of the rig were expected to be small compared to the column displacements.

**Figure 3-9: Linear variable differential transformer**

### 3.2.7 Inclinometers

Four inclinometers were used to measure rotations at elevations of 4 in., 12 in., 24 in. and 34 in. above the column-footing interface. Davis had a crack plane in his spread footing column therefore the height of the inclinometers from the column-footing intersection was not the same as in his test. His crack plane was 6 in. above the column-footing intersection, so therefore, the inclinometers were placed 6 in. closer to the column-footing intersection in these tests.


**Figure 3-10: Inclinometer**

### 3.2.8 Motion Capture System

An Optotrac motion capture system was used in both tests to track the three-dimensional motion of points during the tests. The system consists of LEDs that were attached to the column and two cameras that captured the motion of the LEDs. The configuration of LEDs (Figure 3-11) was similar to that used in Phil Davis' tests. LEDs were attached to three sides of the column; the north side, the west side and the south side. The west side has three lines of LEDs, and two other faces had a single line.

Over the first 24 in. above the column-footing interface, the LEDs were placed at 2 in. spacing. Above that elevation, the LEDs were spaced at 4 in., and only one LED was placed at each elevation on each face. This configuration was chosen, because most of the rotation was expected to be concentrated at the bottom of the column.

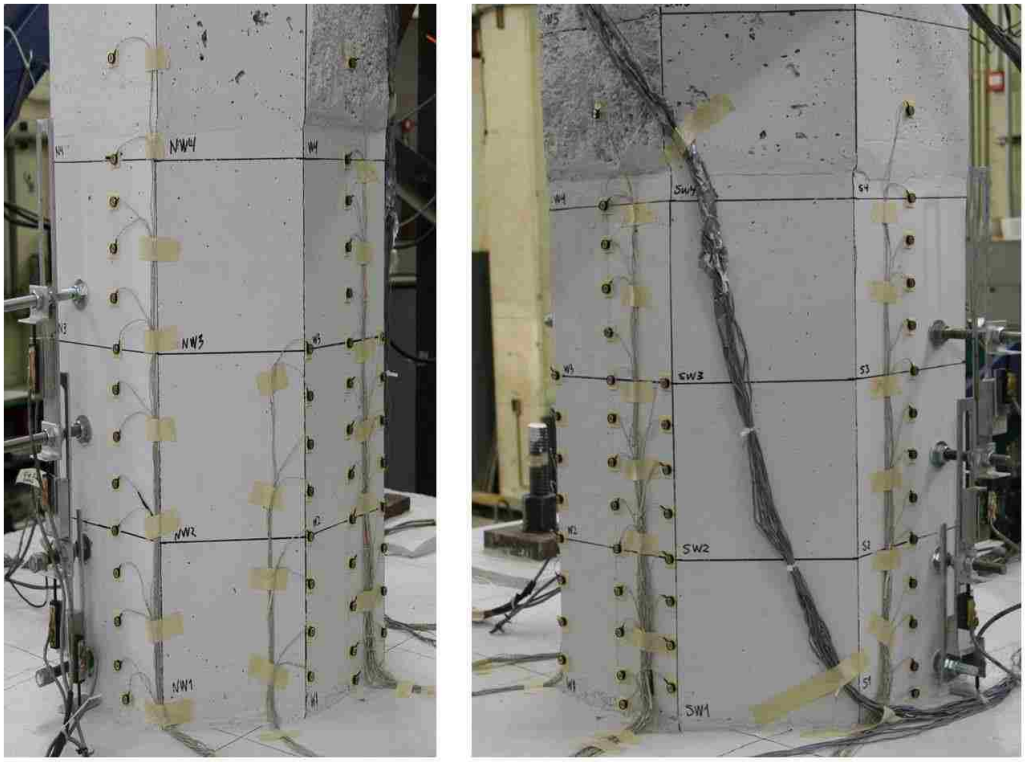


**Figure 3-11: Setup of LEDs, left picture shows north and west sides and the right picture shows the south and west sides of the column**

## 3.3 Testing Protocol

Both specimens were subjected to axial and horizontal loads. The axial load applied to the specimen was 159 kips. The axial load was calculated as the un-factored dead load on a prototype bridge according to the AASHTO LRFD 2009 Specification and scaled down to 42% scale (AASHTO, 2009). The lateral displacement history applied to the columns was a modified version of the NEHERP recommendations for precast structural walls (Building Seismic Safety Council, 2004). Both the axial load and the lateral displacement history were the same as used by Davis et al. (2011) and Haraldsson et al. (2011).

A test cycle was run the day before the both actual test. To ensure that no damage would occur in the columns during the test cycle the axial load was reduced to 90 kips and the lateral drift was only

0.05%. The main reason for doing this test cycle was to make sure that all instruments were working properly; if some instrument were not working, it was fixed or replaced.

The lateral displacement history consisted of 10 set of 4 cycles each, resulting in a total of 40 cycles. The target lateral displacement history is displayed in Table 3-2 and shown graphically in Figure 3-12. The four-cycle sets had peak drift values of close to 1.2X, 1.44X, 1.44X and 0.48X where X is the maximum drift from the previous set. Notice that $1.2^2 = 1.44$ and $1.44/3 = 0.48$. The first set was chosen so that the columns would remain elastic. The drift values controlled the experiments and the lateral displacement was found by multiplying the distance from the center of the action area of the MTS actuator to the column-footing interface (66 in.).

**Table 3-2: Target displacement history.**

| Set | Cycle | Drift [%] | Displacement [in.] |
|---|---|---|---|
| 1 | 1 | ± 0.33 | ± 0.22 |
| | 2 | ± 0.40 | ± 0.26 |
| | 3 | ± 0.40 | ± 0.26 |
| | 4 | ± 0.13 | ± 0.09 |
| 2 | 1 | ± 0.48 | ± 0.32 |
| | 2 | ± 0.58 | ± 0.38 |
| | 3 | ± 0.58 | ± 0.38 |
| | 4 | ± 0.19 | ± 0.13 |
| 3 | 1 | ± 0.69 | ± 0.46 |
| | 2 | ± 0.83 | ± 0.55 |
| | 3 | ± 0.83 | ± 0.55 |
| | 4 | ± 0.28 | ± 0.18 |
| 4 | 1 | ± 1.00 | ± 0.66 |
| | 2 | ± 1.19 | ± 0.79 |
| | 3 | ± 1.19 | ± 0.79 |
| | 4 | ± 0.40 | ± 0.26 |
| 5 | 1 | ± 1.43 | ± 0.94 |
| | 2 | ± 1.72 | ± 1.14 |
| | 3 | ± 1.72 | ± 1.14 |
| | 4 | ± 0.57 | ± 0.38 |
| 6 | 1 | ± 2.06 | ± 1.36 |
| | 2 | ± 2.48 | ± 1.64 |
| | 3 | ± 2.48 | ± 1.64 |
| | 4 | ± 0.83 | ± 0.55 |
| 7 | 1 | ± 2.97 | ± 1.96 |
| | 2 | ± 3.57 | ± 2.36 |
| | 3 | ± 3.57 | ± 2.36 |
| | 4 | ± 1.19 | ± 0.79 |
| 8 | 1 | ± 4.28 | ± 2.82 |
| | 2 | ± 5.14 | ± 3.39 |
| | 3 | ± 5.14 | ± 3.39 |
| | 4 | ± 1.71 | ± 1.13 |
| 9 | 1 | ± 6.16 | ± 4.07 |
| | 2 | ± 7.40 | ± 4.88 |
| | 3 | ± 7.40 | ± 4.88 |
| | 4 | ± 2.47 | ± 1.63 |
| 10 | 1 | ± 8.87 | ± 5.85 |
| | 2 | ± 10.65 | ± 7.03 |
| | 3 | ± 10.65 | ± 7.03 |
| | 4 | ± 3.55 | ± 2.34 |

The columns were pushed and pulled towards north and south end of the building respectively. Columns displacement to the South was defined as positive, and therefore, displacements toward north were negative. The maximum displacement in each cycle the South direction was called “peak”, and the maximum displacement in the North direction was called “valley”. For the first two cycles of each set the specimens were held at the maximum displacement in both north and south direction. That was done so the specimens could be inspected and the crack progression mapped. The last two cycles of each set were run without any stop between cycles. To ensure that the lateral displacement would not be applied too fast, sets 1 to 6 took 20 seconds to reach maximum displacement, sets 7, 8 and 9 took 30 seconds to reach maximum displacement and set 10, the final set, took 60 seconds to reach its maximum displacement. A small-displacement cycle at the end of each set was applied to be able to measure the residual stiffness of the columns.

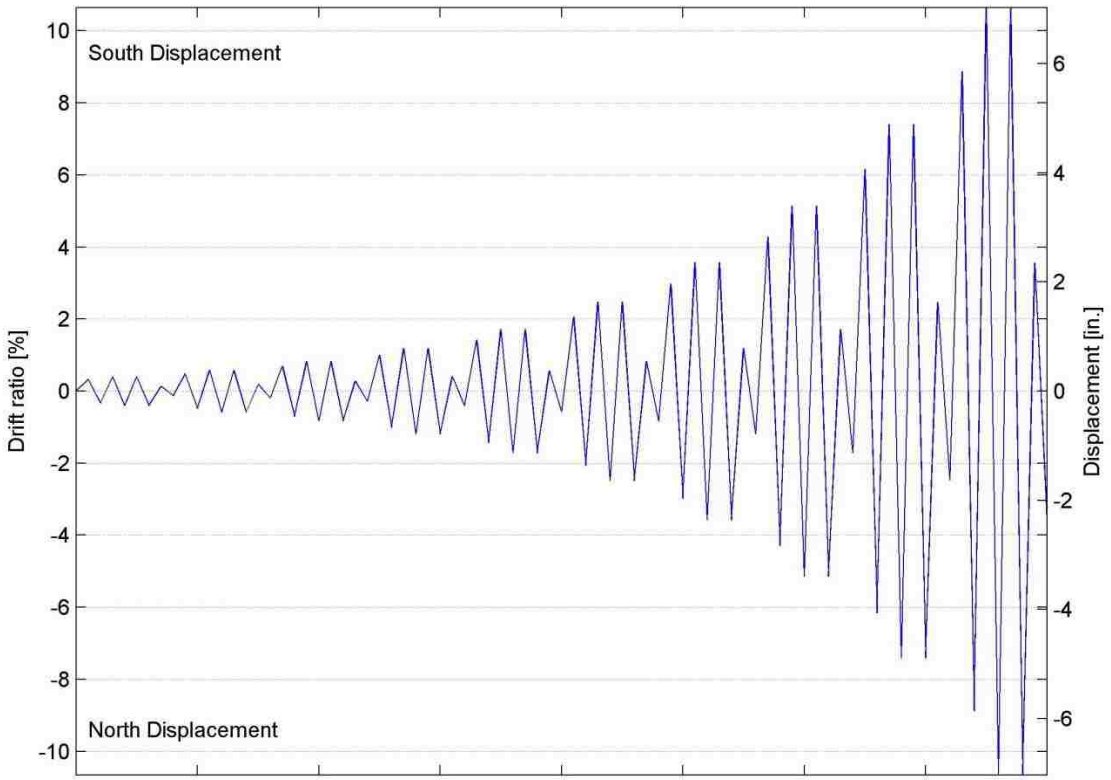


**Figure 3-12: Graphical representation of the target displacement history.**

# 4 Observed Response

While the columns were being tested, the damage was recorded, cracks were marked, the width of the cracks was measured and the columns were photographed. The pictures can be seen in Appendix C. The main purpose of this chapter is to document the progression of damage to the specimens.

## 4.1 Definitions of Damage States in Columns

While the specimens were being tested, they were monitored closely to identify the occurrence of the key damage states defined previously by Barry and Eberhard (2004). In previous experiments at the University of Washington, these definitions of damage states have also been used. Using the same definitions as previous researches makes it easier to compare the levels of damage between specimens. Table 4-1 lists the definitions of the damage states.

**Table 4-1: Definitions of damage states in specimens.**

| Damage state | Description/observation |
|---|---|
| First significant horizontal crack | Crack width ≥ 0.5 mm |
| First significant diagonal crack | Crack width ≥ 0.5 mm and crack extends 1/4 of column diameter |
| First open residual crack | Residual crack width ≥ 0.25 mm |
| First yield of longitudinal rebar | First strain gauge that reaches yield strain |
| First yield of transverse reinforcement | First strain gauge that reached yield strain |
| First spalling in footing | Observed spalling on surface |
| First spalling in column | Observed flaking, minor spalling |
| Significant spalling in column | Spalled height ≥ 1/4 of column diameter |
| Fully spalled | Spalling height no longer increases with increasing deformation |
| Exposure of longitudinal reinforcement | First observation of column longitudinal reinforcement |
| Buckling of longitudinal reinforcement | First observation of buckling of longitudinal reinforcement bars |
| Large cracks in concrete core | Crack width ≥ 2.0 mm |
| Fracture of transverse reinforcement | Observation or sound |
| Fracture of longitudinal reinforcement | Observation or sound |
| Loss of axial capacity | Instability of member (column) |

## 4.2 Damage Progression

The day before each test, the specimen was subjected to a test cycle to verify that all instruments were working and, after the test cycle, the specimens were checked for damage. As noted in Section 3.3, the specimens were only loaded axially to 90 kips and the lateral target drift was 0.05% for these test cycles. In the actual tests, the specimens were loaded axially to 159 kips and subjected to 10 sets of lateral displacement that each consisted of 4 cycles (total 40 cycles) where the maximum target drift was 10.65%.

During the tests, the specimens were carefully monitored for damage. During both tests, each damage state was noted down as it occurred. The only damage stage that could not be recorded during the tests was the yielding of the longitudinal rebar and spiral, because these were detected by the strain gages and not visual observation.

Table 4-2 lists the set, cycle and drift ratio when each defined damage state was reached in both specimens. The positive and negative values correspond to the maximum south drift (peak) and north drift (valley) respectively. The main reason why the values for the north and south drift are not the same is due to deflections of the test frame during test. The configuration of the frame connections results in its having different stiffnesses in the two directions. The onset of bar buckling was also difficult to detect with any accuracy, because he HyFRC cover did not fall away after it was cracked, and therefore obscured the view of the rebars.

In most cases, the two columns reached a given state at approximately equal drift ratios. The most notable differences occurred with bar buckling and bar fracture. The buckling observations should be regarded as unreliable, for the reasons stated above.

**Table 4-2: Summary of damage state progression for both specimens.**

| Damage state | PreT-SS | | | PreT-BS | | |
|---|---|---|---|---|---|---|
| | Set | Cycle | Drift [%] | Set | Cycle | Drift [%] |
| First significant horizontal crack | 3 | 2 | 0.54/-0.73 | 3 | 1 | 0.46/-0.62 |
| First significant diagonal crack | 7 | 2 | 3.29/-3.40 | 6 | 2 | 2.24/-2.36 |
| First open residual crack | 5 | 2 | 1.38/-1.63 | 4 | 1 | 0.73/-0.88 |
| First yield of longitudinal rebar | 3 | 2 | 0.54/-0.73 | 3 | 1 | 0.46/-0.62 |
| First yield of transverse reinforcement | 5 | 2 | 1.38/-1.63 | 5 | 2 | 1.46/-1.61 |
| First spalling in footing | n/a | n/a | n/a | n/a | n/a | n/a |
| First spalling in column | 6 | 2 | 2.12/-2.37 | 5 | 2 | 1.46/-1.61 |

| | | | | | | |
|---|---|---|---|---|---|---|
| Significant spalling in column | 7 | 2 | 3.29/-3.40 | 7 | 1 | 2.77/-2.88 |
| Fully spalled | 9 | 1 | 5.97/-5.98 | 9 | 1 | 6.07/-6.01 |
| Exposure of longitudinal reinforcement | 7 | 2 | 3.29/-3.40 | 8 | 1 | 2.32/-2.47 |
| Buckling of longitudinal reinforcement | 8 | 1 | 4.01/-4.11 | 9 | 1 | 6.07/-6.01 |
| Large cracks in concrete core | 8 | 2 | 4.91/-4.98 | 9 | 1 | 6.07/-6.01 |
| Fracture of transverse reinforcement | 8 | 2 | 4.91/-4.98 | 10 | 1 | 8.90/-8.66 |
| Fracture of longitudinal reinforcement | 9 | 2 | 7.17/-7.17 | 8 | 1 | 4.14/-4.23 |
| Loss of axial capacity | n/a | n/a | n/a | n/a | n/a | n/a |

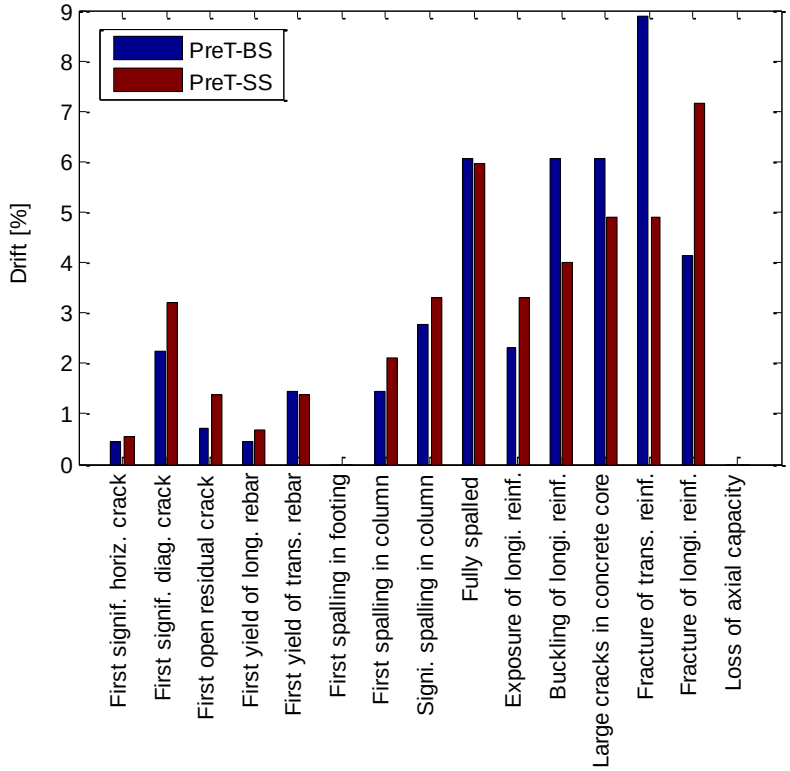


**Figure 4-1: Comparison of drift levels when each damage state was reach between both specimens.**

### 4.2.1 Crack Development and Initial Yield

In both columns little damage occurred during the first four cycle sets (drift ratios up to 1.19%) other than opening of new cracks and yielding of longitudinal rebar. During the first 12 cycles (first 3 sets) of PreT-BS all cracks closed after returning to zero displacement and for the PreT-SS specimen the same happened but all the cracks remained closed during the 16 cycles (first 4 sets). All the cracks that formed in the first four sets of cycles were horizontal cracks. During the first set, all the cracks were only

hairline cracks. During set four the biggest crack had opened up to 4 mm in the PreT-BS specimen, and for the PreT-SS specimen, the biggest crack opened up to 1.5 mm.


**Figure 4-2: PreT-BS after cycle 4-1 when first residual crack was observed.**

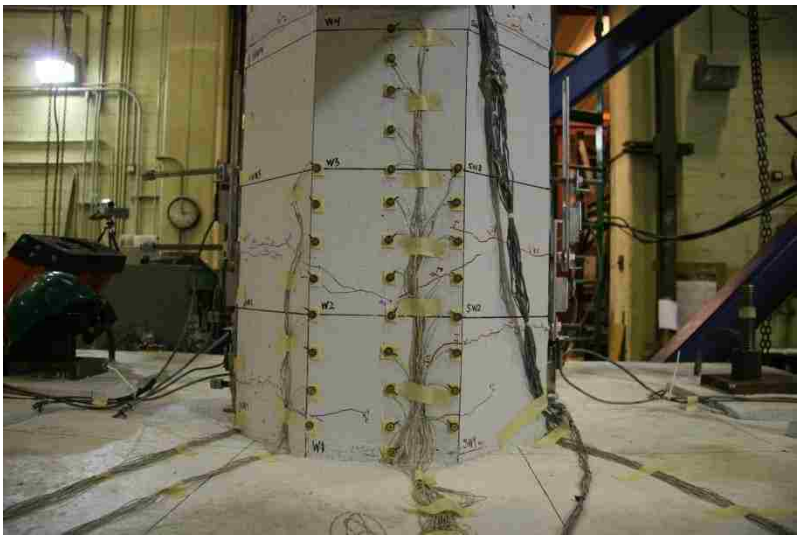


**Figure 4-3: PreT-SS after cycle 5-2 when first residual crack was observed.**

### 4.2.2 Crack Widening and Spalling

The damage in the specimens for the next three sets was more dramatic. The main damage that was observed during sets 5 to 7 (drift ratios up to 3.57%), were that the existing cracks from the first four sets started to widen, and some new cracks formed. But at the later stages of the testing both columns started to rock in the plane of the biggest cracks. One surprising thing happened during the test of the PreT-BS test; on the north side of the column two cracks opened equally and therefore spread the strains

in the longitudinal rebar between those two cracks. Diagonal cracks formed in both specimens during those sets, but the diagonal cracks formed earlier in the PreT-BS specimen than in specimen PreT-SS.

It is worth noting that all of the large cracks that formed in the columns did not form at the height of the maximum moment, the bottom of the columns. Only hairline cracks opened at the column-footing interface. The larger cracks all opened from 4 in. to 10 in. above the column-footing interface. The addition of the HyFRC caused the cracks to open higher than at the top. That might have been because the fibers were not uniformly distributed in the HyFRC and giving the section at the column-footing interface higher strength than higher in the HyFRC shell.

Both columns started to spall during sets 5 to 7. The PreT-BS specimen began to spall in Cycle 5-2 but specimen PreT-SS in Cycle 6-2. The difference between those cycles can possibly be explained by the fact that the HyFRC shell of the PreT-SS specimen was stronger than the HyFRC shell of the PreT-BS specimen, as explained in Section 2.5. Another explanation is that the damage states identified by the researchers depend on their judgment, although the damage states are well defined. After those two cycles, both specimens continued to spall and reached the state of significant spalling, as defined in Table 4-1, during cycles 7-1 (PreT-BS) and 7-2 (PreT-SS).


**Figure 4-4: PreT-BS significant spalling in column during Cycle 7-1.**

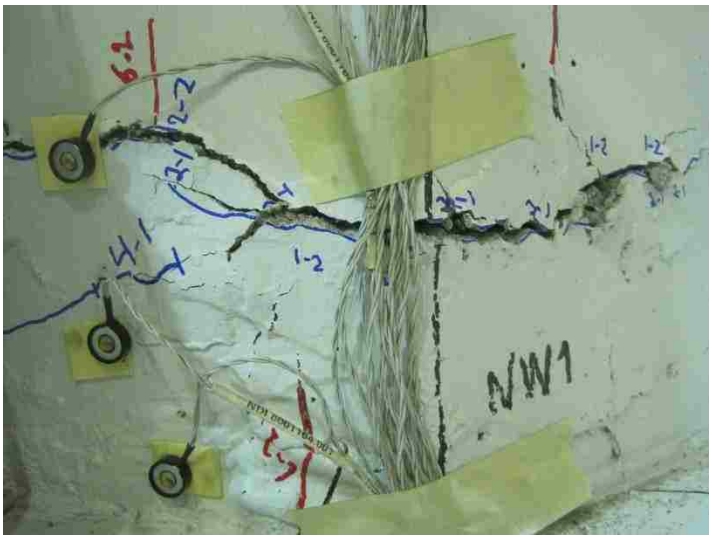


**Figure 4-5: PreT-SS significant spalling in column during Cycle 7-2.**

When the significant spalling damage state had been reached there were only two damage states related to concrete damage that were yet to be observed in both tests. These were the states of fully spalled column and large cracks in column core. In both specimens the spalling height of the concrete in the plastic hinge region stopped increasing in Cycle 9-1 (Drift ratio of 6.16%). Even though the height of the spalling area did not continue to grow the spalling area continued to grow slightly at the sides. That is mainly because the outermost concrete in the specimens had lost most of its strength. The specimens could still have had the same strength (or close to the same strength) the concrete closer to the core of the concrete had to contribute to the strength. At this stage in the tests, the spalling continued on the sides as the concrete closer to the core of the specimen contributed more strength to the specimens.

By the time the columns reached the fully spalled state, large cracks were found in the concrete core. The cracks in the core might have occurred earlier, but they could not be seen because the fibers in the HyFRC prevented the spalled pieces of cover concrete from falling away. The cracks in the core were observed in Cycle 9-1 for Specimen PreT-BS and in Cycle 8-2 for Specimen PreT-SS. This level of damage might have happened earlier for the PreT-BS specimen since the cracks on the north and south side of the HyFRC did not form at the same elevation as the core crack. That probably happened because the bond between the conventional concrete and the HyFRC was not perfect. To make the void in the HyFRC shell, a 12-in. Sonotube was placed inside the HyFRC form. Having a Sonotube made the inside face of the HyFRC too smooth so the bond between the two concretes types was not good enough to form both

the outside cracks and the core crack at the same elevation. Since it was very hard to get good pictures of the core cracks, only the fully spalled column is shown in Figure 4-6 and Figure 4-7.

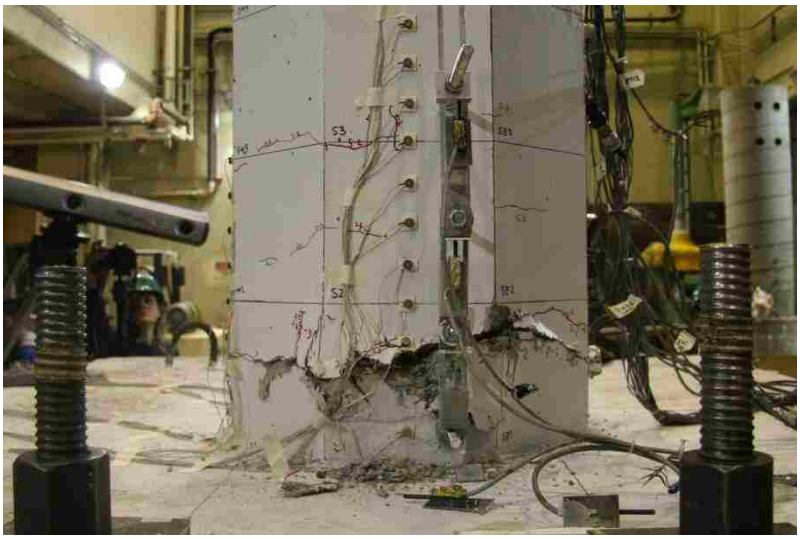

**Figure 4-6: PreT-BS fully spalled.**

**Figure 4-7: PreT-SS fully spalled.**

### 4.2.3 Damage to Longitudinal and Transverse Reinforcement

Table 4-1 lists four damage states related to the reinforcement other than first yield. They are: exposure of longitudinal reinforcement, buckling of longitudinal reinforcement, fracture of transverse reinforcement and fracture of longitudinal reinforcement. In both specimens all those damage states were reached during the later stages of the tests. In both tests the exposure of the longitudinal rebar was the first damage state out of those four mentioned before to occur. Therefore point at which the

longitudinal rebar was visible, through cracks, is listed into Table 4-2. During the tests, the longitudinal rebar was never fully exposed, except when the spalled part of the HyFRC was pulled away from the rest of the column.

After the column had spalled there was less material to prevent the longitudinal rebar from buckling. For both columns the rebar buckled after significant spalling occurred, and the first buckling of the longitudinal rebar was first noticed in Cycle 9-1 for PreT-BS and in Cycle 8-1 for PreT-SS. It's likely that the longitudinal rebar in Specimen PreT-BS might have bucked earlier but it was not observed from the outside of the column, probably because the spalled part of the HyFRC blocked the view and the buckling couldn't be seen through the cracks. Another reason why that it is likely that the rebar had probably buckled earlier in Specimen PreT-BS is that the north rebar fractured during Cycle 8-1 and the south rebar during Cycle 8-3. Therefore the noted Cycle 9-1 for buckling in PreT-BS was when first buckling of rebar was actually seen and that was the north-east bar that buckled at that time.

The fracture of the longitudinal rebars in PreT-BS happened somewhat earlier than expected, especially the north bar. Since stainless steel is more ductile than conventional rebar, it was expected that the rebars would fracture later than the longitudinal rebar of specimen PreT-BS. That was actually what happened, and both the north and the south reinforcing bars fractured during Cycle 9-2 or at drift ±7.17%, but the rebar of specimen PreT-BS fractured at drift levels of -4.98% and 4.01%. This difference is very significant. When the south bar of the PreT-SS specimen broke a video was captured where the breaking of the longitudinal rebar was very obvious. The final damage related to the reinforcement of both specimens was the fracture of the transverse reinforcement. In both columns the fracture was detected by the sound of the spiral breaking. The fracture of the spiral happened much earlier for the PreT-SS specimen then for the PreT-BS specimen.

**Figure 4-8: PreT-BS broken longitudinal rebar.**

**Figure 4-9: PreT-SS buckled rebar and broken spiral.**


**Figure 4-10: PreT-SS broken longitudinal rebar and broken spiral after spalled concrete had been peeled off after the test was finished.**

Two of the predefined damage states never occurred during the tests; those damage stages were loss of axial capacity and spalling in the footing. This behavior was as expected since in former tests by Haraldsson et al. (2011) and Davis et al. (2011), the axial capacity was not lost nor spalling in footing was observed. In Haraldsson's tests, the axial capacity of the column-footing connection was tested after completing the combined axial and lateral loading test. When the axial load reached about 3.5 times the factored design axial load, the column exploded, but no damage was observed in the footing. Spalling in the footing was never expected since the footing was capacity-designed to force damage into the columns while leaving the footings undamaged.

# 5 Measured Response

## 5.1 Material Properties

The specimens were constructed in the Structural Engineering Laboratory at the University of Washington. The columns were constructed in a prestressing rig, and a hydraulic ram was used to prestress each strand of the columns individually. The columns were cast in the lab, cured, and then placed in the footing forms where the footings were cast around the columns. For every concrete batch (both regular concrete and HyFRC) concrete cylinders were cast: 4 in. by 8 in. cylinders were used for the HyFRC and 6 in. by 12 in. cylinders were used for the conventional concrete. The cylinders were stored in a fog room at the University of Washington where the relative humidity was kept at 100%, and the temperature remained at around 70°F.

Material tests were performed on the main structural materials of both specimens, including the HyFRC, regular concrete, regular longitudinal reinforcement bars, stainless steel longitudinal reinforcement bars and spiral reinforcement.

### 5.1.1 Conventional Concrete

For each of the three batches of regular concrete (columns, PreT-BS footing and PreT-SS footing) cylinders were tested at 3 days, 7 days, 14 days, 28 days, and the test day. Both columns were cast and released on the same day. For that concrete, cylinders were tested also on the day of release. The compressive strengths of the concrete on the test day are reported in Table 5-1. The compressive strength history for all of the batches is provided in Appendix A. Table 5-1 shows that the column concrete decreased in strength as it aged from 70 days to 89 days. This is unlikely in practice, and the small difference in strengths is attributed to random variations in strength rather than a systematic trend.

**Table 5-1: Compressive strengths of concrete on test day**

| Specimen | Column | | Footing | |
|---|---|---|---|---|
| | Strength [psi] | Age [days] | Strength [psi] | Age [days] |
| PreT-SS | 6740 | 70 | 8760 | 51 |
| PreT-BS | 6660 | 89 | 5650 | 72 |

For the column concrete, the elastic modulus of the concrete was measured on every day that the strength was measured. The elastic modulus was measured only for one batch of footing concrete, because such measurements were needed for another project. The elastic modulus of the concrete for both specimens is displayed in Table 5-2. A time history of the elastic modulus of the concrete can be found in Appendix A.

**Table 5-2: Elastic modulus of the column concrete on test day.**

| Specimen | E-mod [ksi] | Age [days] |
|---|---|---|
| PreT-SS | 3556 | 70 |
| PreT-BS | 3310 | 89 |

The split-cylinder strength was measured. The tensile strength is computed as:

$$f_{ct} = \frac{2P}{\pi l d} \quad 5\text{-}1$$

where P is the maximum load applied in the test, l is the length of the specimen (12 in. for 6x12 in. cylinders) and d the diameter of the specimen (6 in. for 6x12 in. cylinders). The split cylinder tests were only performed on the testing days, and the results are displayed here below.

**Table 5-3: Tension strength of conventional concrete on test days.**

| Specimen | $f_{ct}$ [psi] | Age [days] |
|---|---|---|
| PreT-SS | 555 | 70 |
| PreT-BS | 515 | 89 |

### 5.1.2 HyFRC

With the exception of Batch #5, only three 4 in. by 8 in. cylinders were cast for each HYFRC batch. On day 3, cylinders from Batch #1 and Batch #5 were tested, and a large difference in the compressive strengths was observed where Batch #5 was much stronger. All batches were tested on test day. Since Batch #5 included many cylinders, the compressive strength of Batch #5 was measured on days 3, 7, 28, the first day when the prestressing strands were released (day 52), and on test days. For batches 1-4 the compressive strength on the test day (and earlier days, if any were available) was used to estimate the compressive strength history. The compressive strength histories for all the batches of HyFRC can be found in Appendix A.

**Table 5-4: Compressive strength of HyFRC on test day.**

| Batch | Strength [psi] | Age [days] |
|---|---|---|
| 1 | 6980 | 134 |
| 2 | 6580 | 134 |
| 3 | 6770/6960 | 116/134 |
| 4 | 6780 | 116 |
| 5 | 8230 | 116 |

For all the batches of HyFRC, the elastic modulus was measured every day that the HyFRC was tested for strength. Table 5-5 below shows the elastic modulus of all the batches on test day. For the same reason as the strength measurement, Batch #3 was only tested once for elastic modulus. Appendix A lists the history of the elastic moduli of all the batches.

**Table 5-5: Elastic modulus of HyFRC on test day**

| Batch | E-mod [ksi] | Age [days] |
|---|---|---|
| 1 | 4718 | 134 |
| 2 | 4723 | 134 |
| 3 | 4374 | 116 |
| 4 | 4303 | 116 |
| 5 | 4830 | 116 |

Split cylinder tests were performed on the HyFRC 4 in. by 8 in. cylinders from Batch #5. The results from the split cylinder tests are reported in the Table 5-6.

**Table 5-6: Tension strength of HyFRC Batch #5 at testing day.**

| Batch | $f_{ct}$ [psi] | Age [days] |
|---|---|---|
| 5 | 1040 | 120 |
| 5 | 1160 | 139 |

The average tensile strength (1100 psi) for Batch #5 on the test days corresponds to 12.2 times the square root of the compressive strength on the test day (8230 psi). This factor is approximately twice the corresponding factor for the conventional concrete. When the HyFRC was tested for tension strength the break was very ductile. The maximum strength was reached when a crack formed. The

loading was continued and the cylinder still held together. For conventional concrete cylinder splits into two half cylinders, but that did never happen for the HyFRC cylinders.

### 5.1.3 Conventional (Black) Steel Reinforcement

Except for the longitudinal reinforcement in the PreT-SS specimen and the spiral in both columns, conventional (black) steel reinforcing bars, #3, #4 and #5, wer used for all reinforcement, both in the footings and the columns. Both columns used 3-gauge smooth wire spiral. The key features for every type of reinforcement are displayed in Table 5-7. Complete stress-strain curve for all types of the reinforcement can be found in Appendix A. It should be noted that the spiral was supplied in coils. The wire had therefore been subjected to some plastic bending, and it had to be straightened, which imposed reversed plastic bending, before testing. The absence of a yield plateau in these tests is therefore not surprising. It is not known whether the virgin wire would have a yield plateau.

**Table 5-7: Yield strength, ultimate strength and elastic modulus for black steel used in tests.**

| Type | $f_y$ [ksi] | $f_u$ [ksi] | E-mod [ksi] |
|---|---|---|---|
| #3 | 66.1 | 102.2 | 28200 |
| #4 | 67.1 | 92.6 | 28100 |
| #5 | 61.9 | 86.0 | 26500 |
| 3 gauge spiral | 86.3 | 96.0 | 30500 |

### 5.1.4 Stainless Steel Reinforcement

Since stainless steel reinforcing bars were only used for longitudinal reinforcement in the stainless steel column, only one size (#4) was tested. Two tests were performed. The gauge length used for the test was 8 in. and the stress in the bar was determined by dividing the load in the bar by the nominal bar area. The strain in the bar was measured by using two strain gauges on each side of the bar tested, and so is a local value. The main results from the tests on the bars are displayed in Table 5-8; the values in the table are averages from the two tests. Yield was taken as being the stress where the stress-strain curve crosses a line with a slope of the E-mod and crosses the strain axis at a strain of 0.2%. The complete stress-strain curves for the stainless steel can be found in Appendix A.

**Table 5-8: Summary of tests on stainless steel reinforcement bars #4**

| $f_y$ [ksi] | $f_u$ [ksi] | E-mod [ksi] |
|---|---|---|
| 91.2 | 117.7 | 22546 |

The minimum yield strength for Stainless Steel Alloy 2205 is 65 ksi (ASTM International, 2010). The test bars had yield strengths of 90.9 ksi and 91.5 ksi, or about 50% higher than the specified minimum. The Young's modulus was also lower than expected. Young's modulus varies somewhat among different stainless steels, but is generally 3 to 9% lower than that of black steel. The samples were 22% lower than the 29,000 ksi typically assumed for black steel. The reasons for the difference are unknown.

Both stainless steel specimens tested broke at a strain of approximately 0.20 in/in, which was larger than the fracture strain of the black steel bars. This value was estimated by re-assembling the broken pieces after testing. The strain gages stopped working at a strain of about 0.030 in/in so the recorded stress-strain curves for the stainless steel bars stop there and give the incorrect impression that the stainless steel was less ductile than the black steel.

## 5.2 Moment-Drift Response

Three types of external forces acted on the column, axial load (P), lateral load due to the 200 kip MTS actuator (H) and lateral load due to friction in the sliding channel (F). From those three external forces a model was created to calculate the moment at the base of the column. The model is displayed in Equation 5-2.

$$M = H \cdot h_1 + F \cdot h_2 + P \cdot \frac{h_2}{h_1} \cdot \Delta_1 \qquad 5\text{-}2$$

In this equation M is the calculated base moment; H is lateral load from the 200 kip MTS actuator; $h_1$ is the height to the center of the 200 kip MTS actuator; $h_2$ is the height to the top of the spherical bearing on top of the column; F is the estimated friction force due to the friction between the greased PTFE on the bearing and virgin stainless steel plates placed in the sliding channel; P is the vertical load from the Baldwin Universal Testing Machine, and $\Delta_1$ is the measured displacement of the column at height $h_1$ above the column footing.

Figure 5-1 shows the definitions of the forces and heights. $\Delta_2$ was not measured, so an approximation for it in Equation 5-2 was needed. It was taken as $\Delta_1 \cdot \frac{h_2}{h_1}$ because the segment of the column above the ram axis is assumed to be perfectly straight.

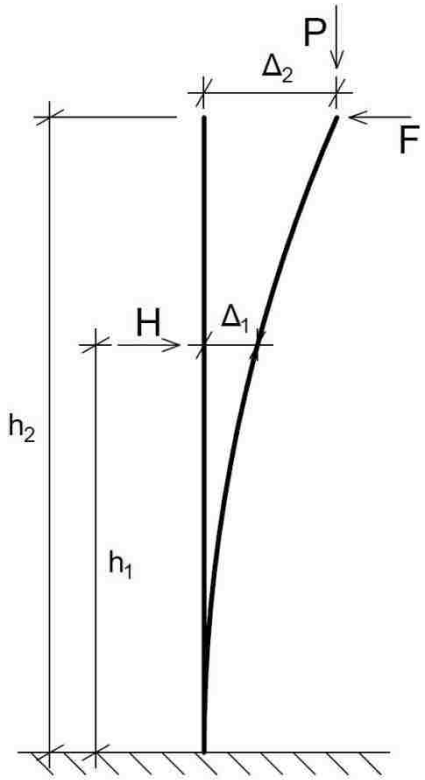


**Figure 5-1: Definitions of variables for Equation 5-2.**

As mentioned before, greased PTFE was placed on all surface of the spherical bearing in contact with the stainless steel sheet in the channel. The spherical surfaces consisted of greased steel on steel. Frictional resistance is provided by both the flat and the curved surfaces, because slip occurs at both. The friction force (F) was calculated using the model developed by Brown et al. (2008) can be seen in Figure 5-2.

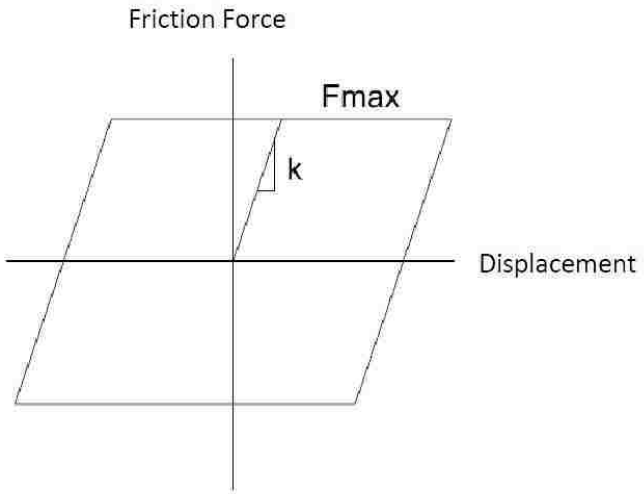


**Figure 5-2: Friction correction model, Brown et al. (2008).**

The combined motion on the flat and curved surfaces causes friction that can be modeled as an effective coefficient of friction on a single flat surface. That is given by:

$$\mu_{eff} = \mu_{flat} + \mu_{curv}\frac{R}{L_{total}} \qquad 5\text{-}3$$

In this model $\mu_{flat}$ is the friction coefficient of the flat part of the bearing and $\mu_{curv}$ is the friction coefficient between the greased spherical parts. Since R << $L_{total}$ where $L_{total}$ is the total length of the column, it was assumed that $\mu_{eff} \approx \mu_{flat}$= 1.6%. With maximum horizontal force from the 200 kip MTS actuator assumed to be close to 50 kips and the target axial load of 159 kips the friction force would be 2.54 kips or about 5% of the maximum horizontal force from the 200 kip MTS actuator.

The moment-drift response of both columns is shown in Figures 5-2 through 5-6. Because the friction correction depends on the assumed value of $\mu$, the uncorrected plots are shown first in Figures 5-2 and 5-3. In them Equation 5-2 was used to calculate the moment and the friction was assumed to be zero.

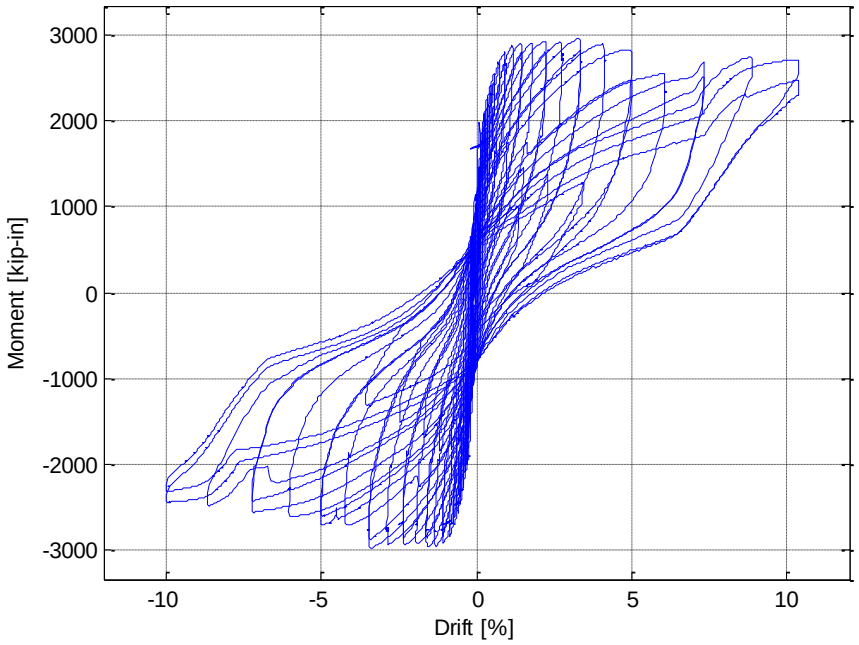


**Figure 5-3: Uncorrected moment-drift plot for Specimen PreT-BS.**

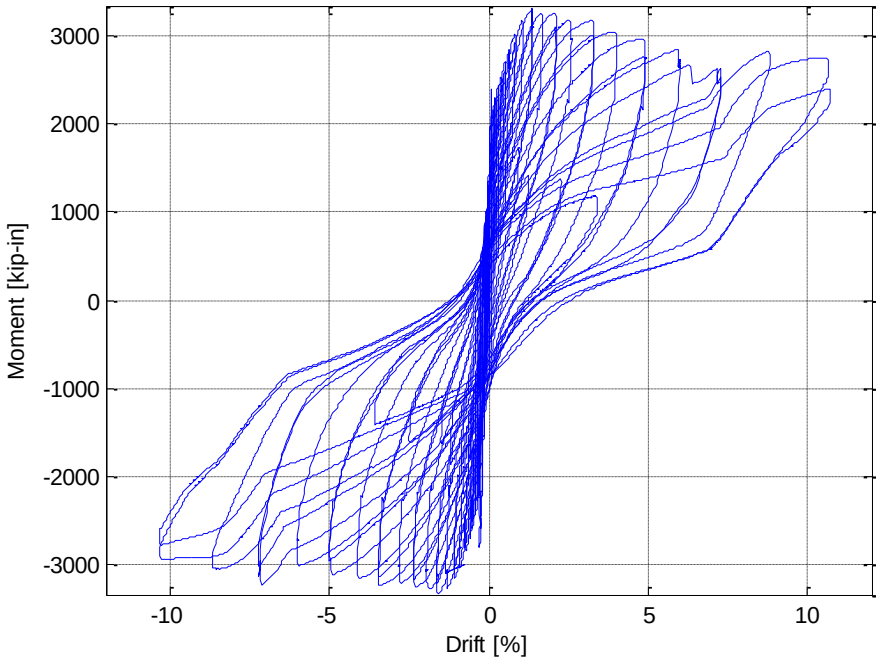


**Figure 5-4: Uncorrected moment-drift plot for Specimen PreT-SS.**

The friction model (see Figure 5-2) has an elastic stiffness component, which was taken here as 60 kips/in. and a maximum force of $F_{max} = \mu_{eff} \cdot P$ where P is the axial load. Figure 5-5 and Figure 5-6 show that use of k = 60 kips/in. resulted in sudden drop (or rise) in the peak (or valley) moment. This behavior was not observed in the figures for the uncorrected moment-drift plots.

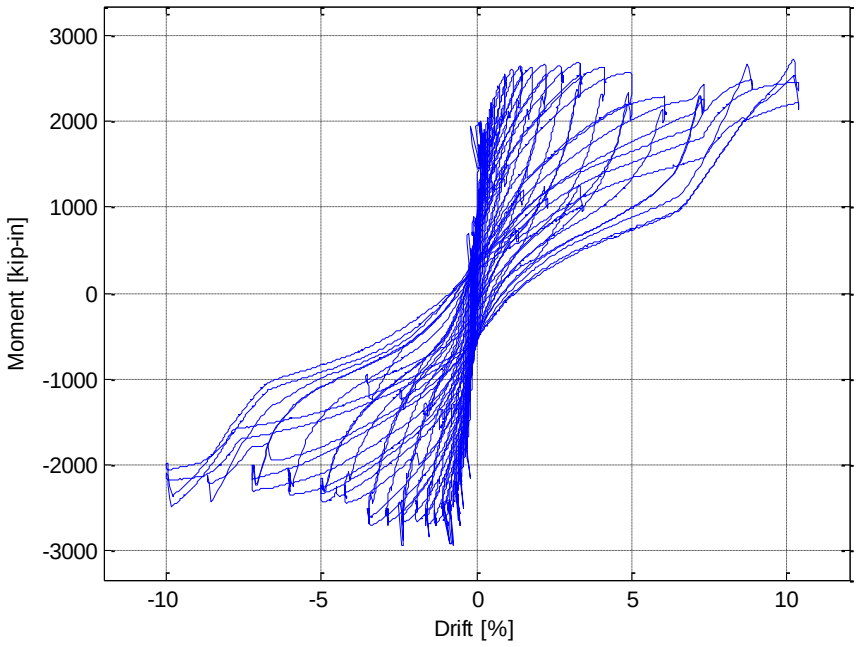


**Figure 5-5: Corrected moment-drift plot for Specimen PreT-BS using k = 60 kips/in.**

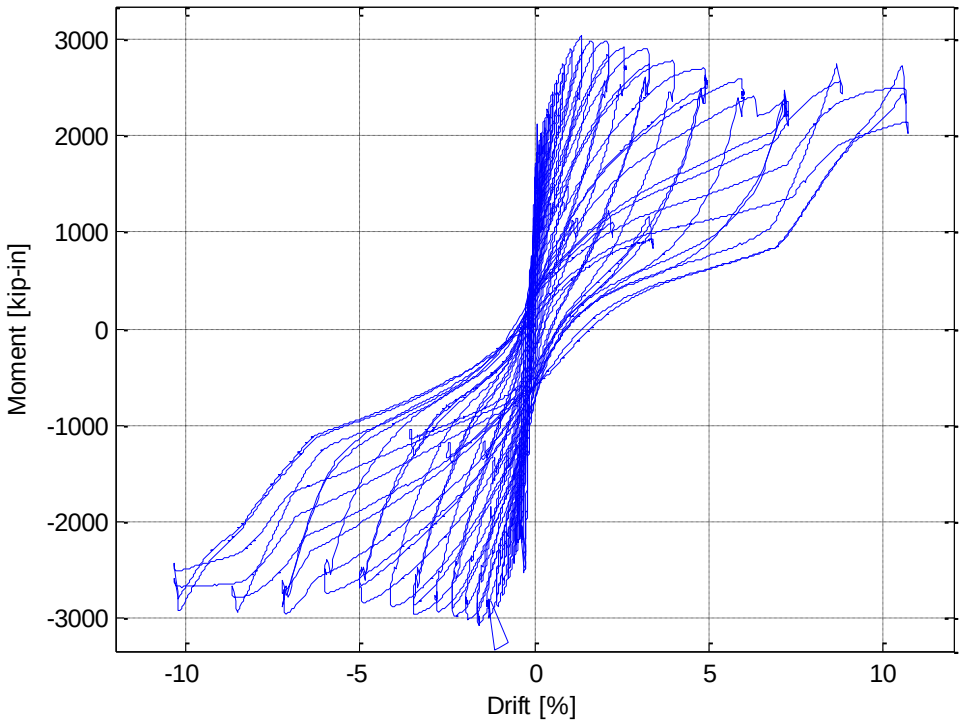


**Figure 5-6: Corrected moment-drift plot for Specimen PreT-SS using k = 60 kips/in.**

Because of those quick drops and rises in the moment-drift plots, the spring stiffness was lowered from 60 kips/in. to 5 kips/in. $\mu_{eff}$ was kept at 1.6%. After making this change, the drops and raises stopped but the peak and valley moments decreased Figure 5-7 and Figure 5-8 show the final corrected moment-drift plots for both specimens.

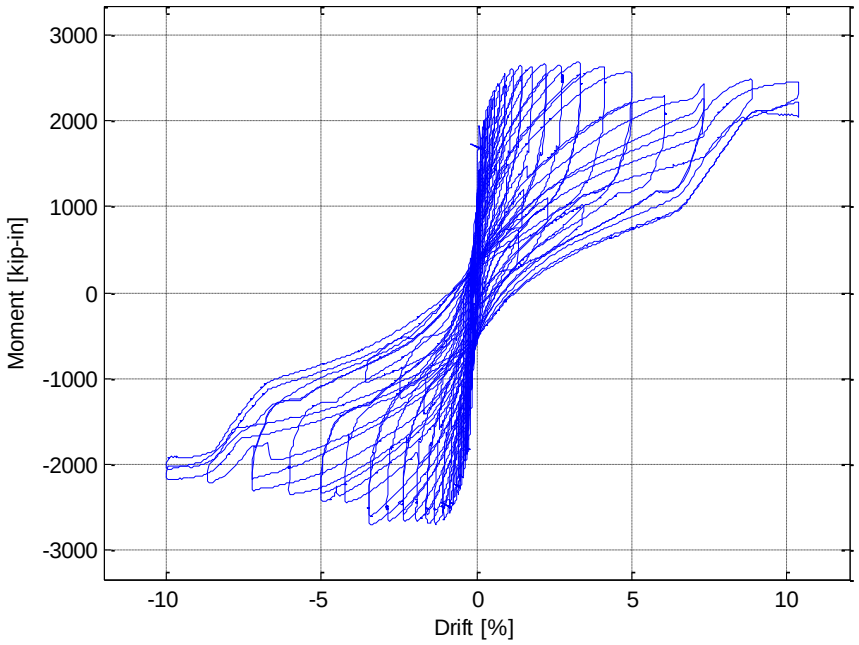


**Figure 5-7: Corrected moment-drift plot for Specimen PreT-BS using k = 5 kips/in.**

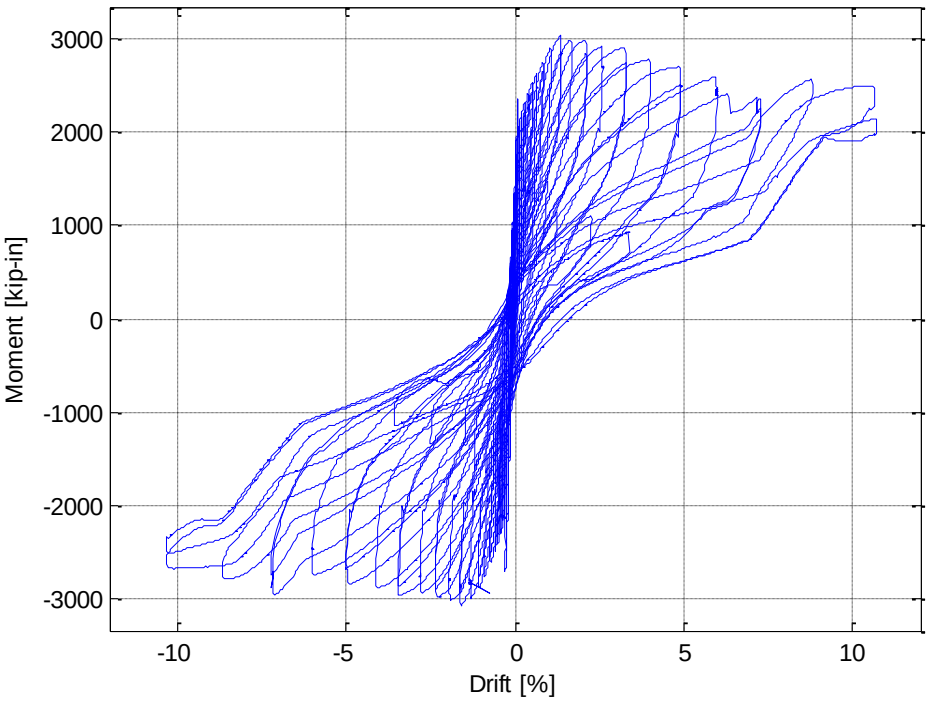


**Figure 5-8: Corrected moment-drift plot for Specimen PreT-SS using k = 5 kips/in.**

The moment-drift plots for both specimens (Figure 5-7 and Figure 5-8, and Table 5-9) show that both specimens behaved similarly. The main difference between the specimens is that the PreT-SS specimen was approximately 13% stronger than the PreT-BS specimen. This difference was as expected, since the stainless steel reinforcement was stronger than the black steel (and more ductile). One similarity was how well both specimens maintained their strengths throughout the tests. One common measure of "failure" is the point at which the moment resistance decreases to 80% of its maximum value. It can be seen that the specimens maintained this resistance during the entire test, to more than 10% drift. In comparison, the strength of the pretensioned column (PreT-SF) tested by Davis et al. (2012) dropped to 80% of the peak at a drift ratio of about 5.5%. Comparison of Davis' column with the two tested in this study shows that the addition of HyFRC to the columns allowed the columns to maintain their strength for much larger drift values.

**Table 5-9: Summary of moment-drift response.**

| Point of Interest | PreT-BS | | PreT-SS | |
|---|---|---|---|---|
| | North Direction | South Direction | North Direction | South Direction |
| Maximum Moment [kip-in.] | -2717 | 2703 | -3077 | 3044 |
| Drift Ratio at Maximum Moment [%] | -3.45 | 3.35 | -1.60 | 1.35 |
| 80% of Maximum Moment [kip-in.] | -2190 | 2180 | -2506 | 2464 |
| Drift Ratio of 80% of Maximum Moment [%] | < -9.93 | > 10.39 | < -10.31 | > 10.66 |

## 5.3 Effective Force Acting on Specimens

The effective force acting on the column was calculated by dividing the moment by the height where the 200 kip MTS actuator was acting on the column. Therefore the equation for the effective force is simply:

$$F_{eff} = H + F \cdot \frac{h_2}{h_1} + P \cdot \frac{h_2}{{h_1}^2} \cdot \Delta_1 \qquad 5\text{-}4$$

Figures 5-9 and 5-10 show the effective force versus the drift for the column specimens. They were developed using Equation 5-4, and are identical to the moment-drift plots except for the scale.

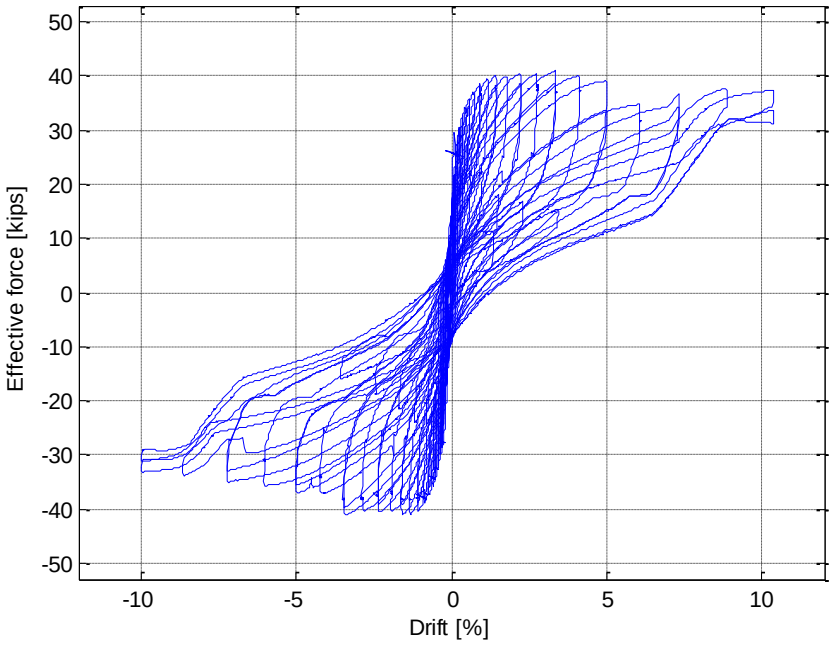


**Figure 5-9: Effective force-drift response for Specimen PreT-BS using k = 5 kips/in.**

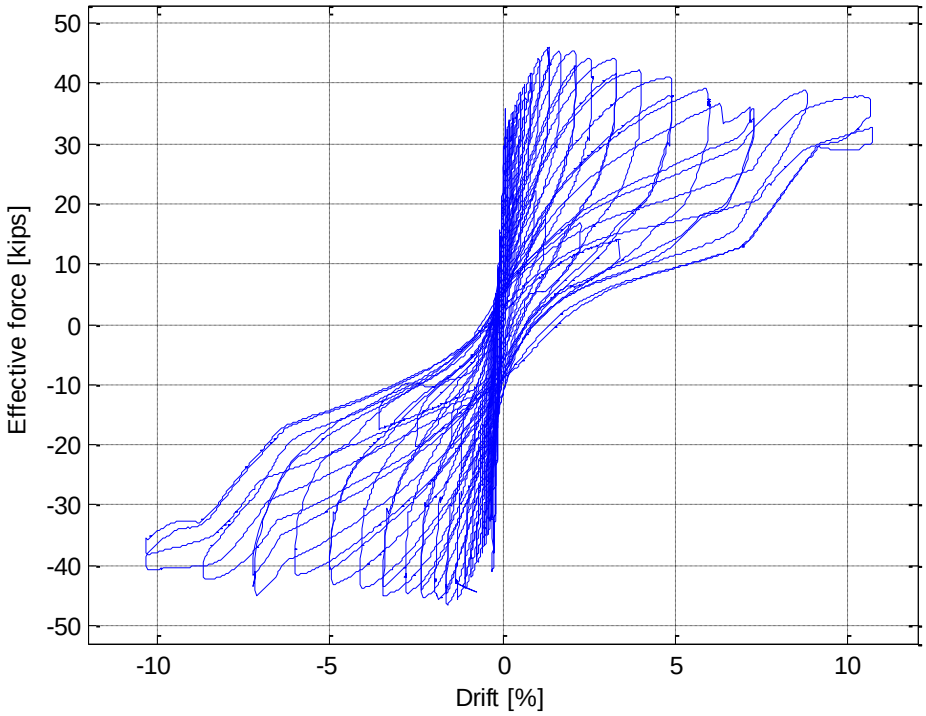


**Figure 5-10: Effective force-drift response for Specimen PreT-SS using k = 5 kips/in.**

The average of the positive and negative peak loads for the specimens was 41.1 kips for PreT-BS and 46.4 kips for PreT-SS. The addition of the stainless steel rebar to the specimens provided the columns with approximately 13% additional strength. It is worth noting that the PreT-BS specimen did not reach the targeted drift value in the north direction because the 200 kip MTS actuator reached the limit of its stroke for cycles 10-2 and 10-3.

**Table 5-10: Summary of effective force results.**

| Point of Interest | PreT-BS | | PreT-SS | |
|---|---|---|---|---|
| | North Direction | South Direction | North Direction | South Direction |
| Maximum Effective Force [kips] | -41.2 | 41.0 | -46.6 | 46.1 |
| Drift Ratio at Maximum Effective Force [%] | -3.45 | 3.35 | -1.60 | 1.35 |
| 80% of Maximum Effective Force [kips] | -33.2 | 33.0 | -38.0 | 37.3 |
| Drift Ratio of 80% of Maximum Effective Force [%] | -9.93 | 10.39 | -10.32 | 10.66 |

## 5.4 Column Rotations

The column rotations were measured by using three types of instruments: curvature rod system; inclinometers and the Optotrac LED tracking system.

The local rotation between curvature rods was calculated using Equation (5-5):

$$\theta_i = \frac{\delta_{i,N} - \delta_{i,S}}{L_i} \qquad 5\text{-}5$$

where $\theta_i$ is the rotation at specified height in the column;

$\delta_{i,N}$ is the displacement on the north side of the column;

$\delta_{i,S}$ is displacement on the south side of the column and

$L_i$ in the horizontal distance between the linear potentiometers on the north and south sides of the column.

Figure 5-11 and Figure 5-12 show the rotations in the columns at the heights of the curvature rods at drift levels of ±0.3%; ±0.7%; ±1.2%; ±2.0%; ±3.0% and ±4.0%. The rods were located 1.5”, 6.75”, 11.75” and 17.5” above the top of the footing.

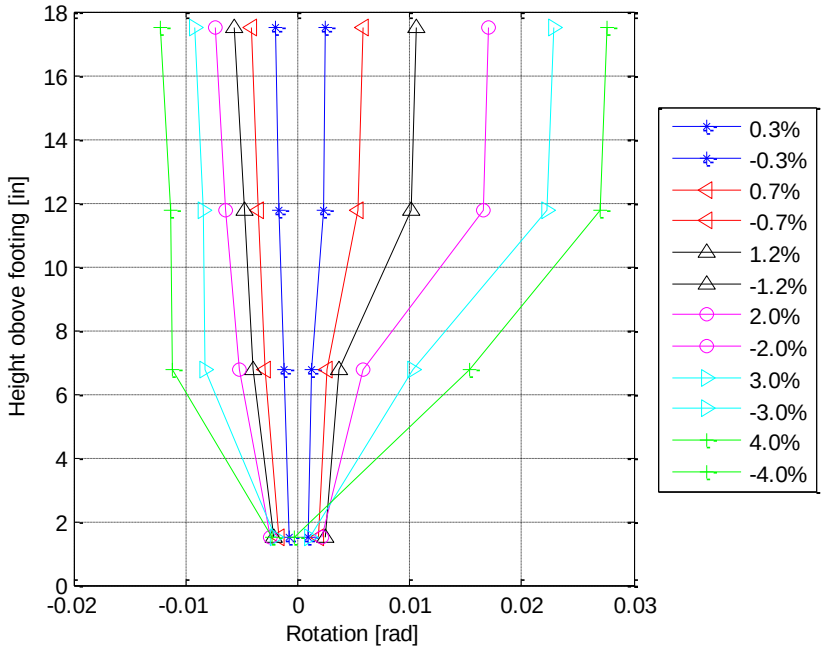


**Figure 5-11: Column rotations from curvature rod system for Specimen PreT-BS.**

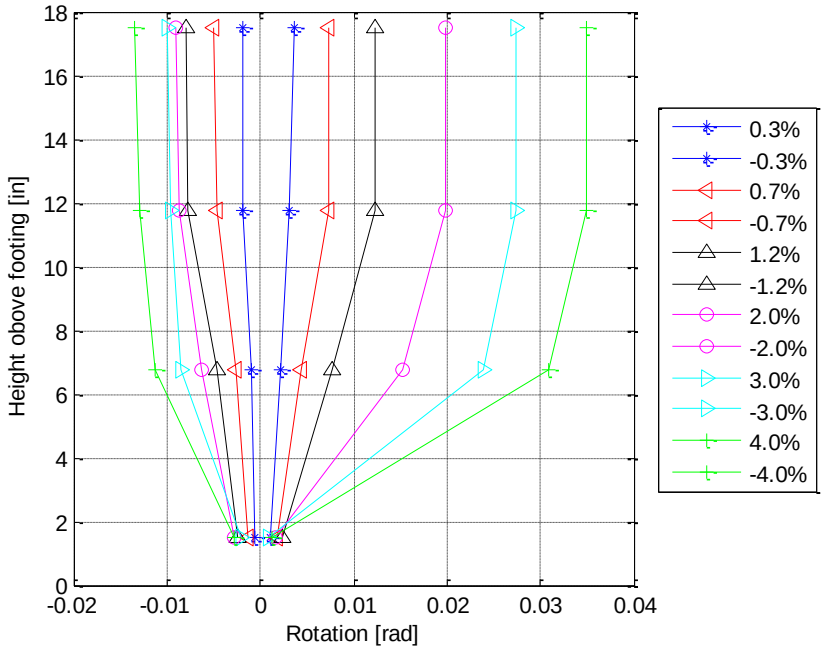


**Figure 5-12: Column rotations from curvature rod system for Specimen PreT-SS.**

The second instrument that was able to measure the rotation of the specimens was the inclinometers, and they directly measured the rotation in the column where the inclinometers are attached to the column. The results from the inclinometers can be seen in Figure 5-13 and Figure 5-14, for the same drifts as shown in Figures 5-11 and 5-12.

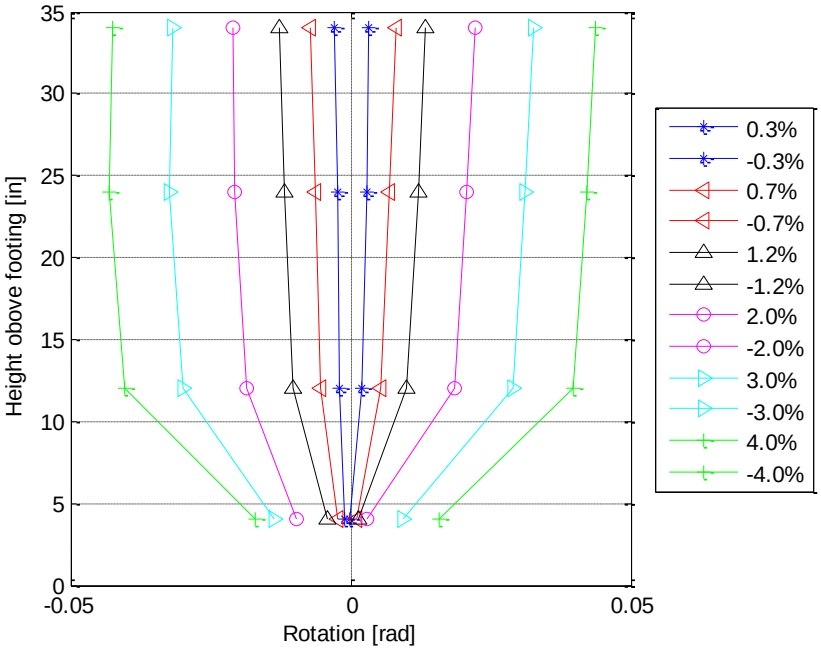


**Figure 5-13: Rotations of specimen PreT-BS from inclinometers.**

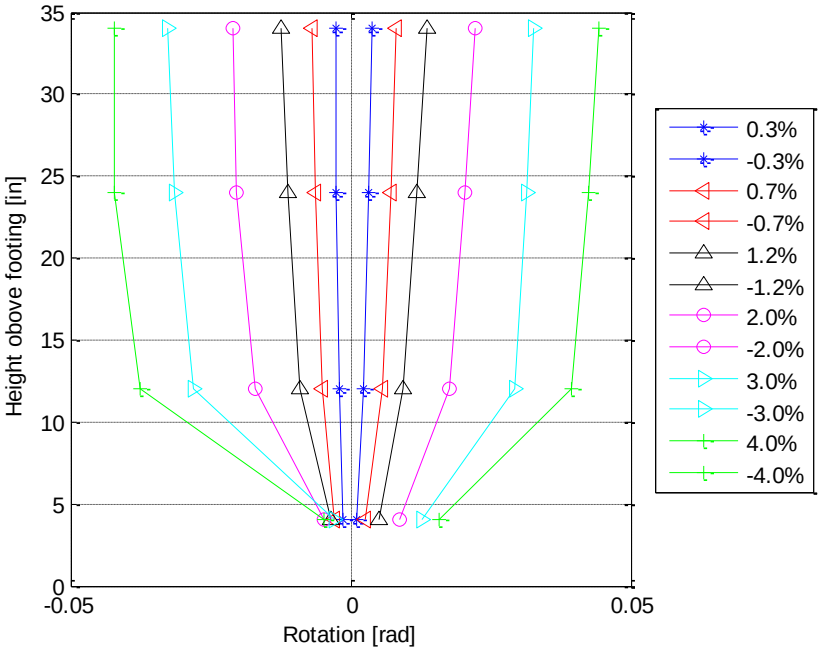


**Figure 5-14: Rotations of specimen PreT-SS from inclinometers.**

The third instrument type that was used to measure the rotation of the specimen was the LED motion capture system (Optotrac System). This system relies on LED blinking and cameras that capture the motion of those LEDs.

Some of the data for the system seemed unrealistic. This is believed to have been caused by the fact that, at times, the cameras might have been unable to see the LEDs because other equipment might have blocked the light path. A recommendation for forthcoming research would be to get tripod that allows the camera to be aligned vertically and therefore be blocked by fewer obstacles.

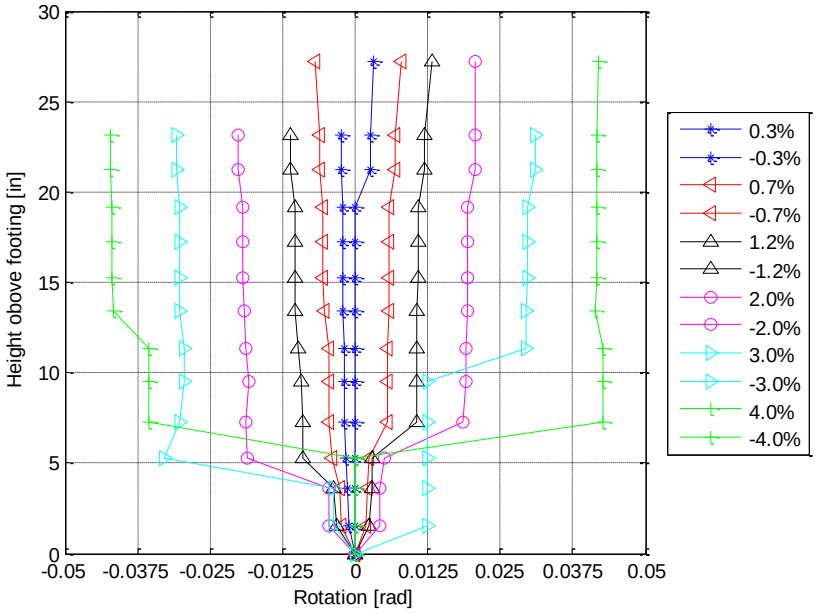


**Figure 5-15: Column rotations over the height of the column for Specimen PreT-BS, from Optotrac system.**

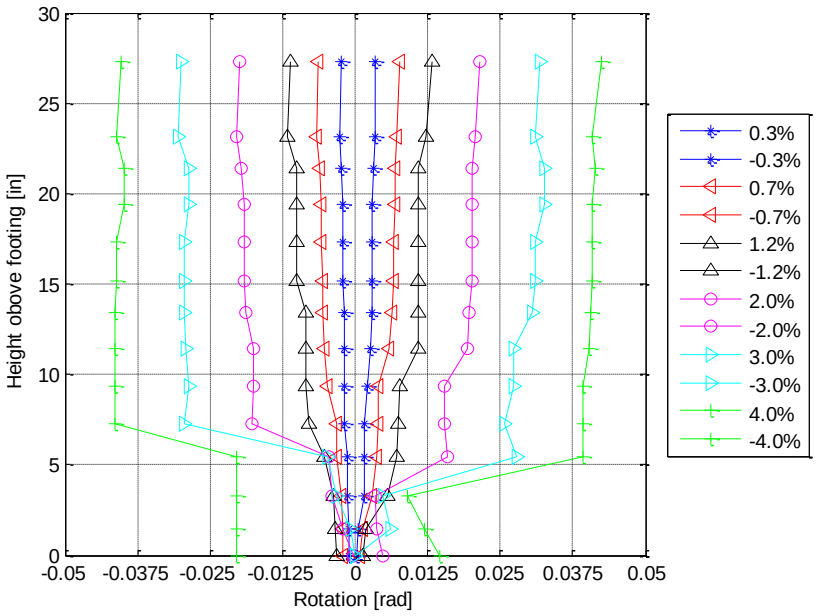


**Figure 5-16: Column rotations over the height of the column for Specimen PreT-SS, from Optotrac system.**

The deformation pattern obtained from the Optotrac system is similar to those obtained from the other two systems; the column moved essentially as a rigid body above approximately 6 in. above the base. Below that location, there was essentially no movement. That location coincides with the location of the cracks. The Optotrac system used sensors on a finer grid than in the other two systems, so provided a more detailed picture of the response.

It can be seen in Figure 5-15 that, at 3% drift, the LEDs were blocked since the rotation doesn't increases rapidly in the same height as for other drifts. The rotation should have increased in the same height because where the rapid increase is in the height level of the crack on each side of the column. The strange values for the rotation at the bottom in Figure 5-16 is because the LEDs at the bottom of the column had been removed to prevent damage to the LEDs.

The rotation measurements of the three systems are compared at ±2% drift in the figures below.

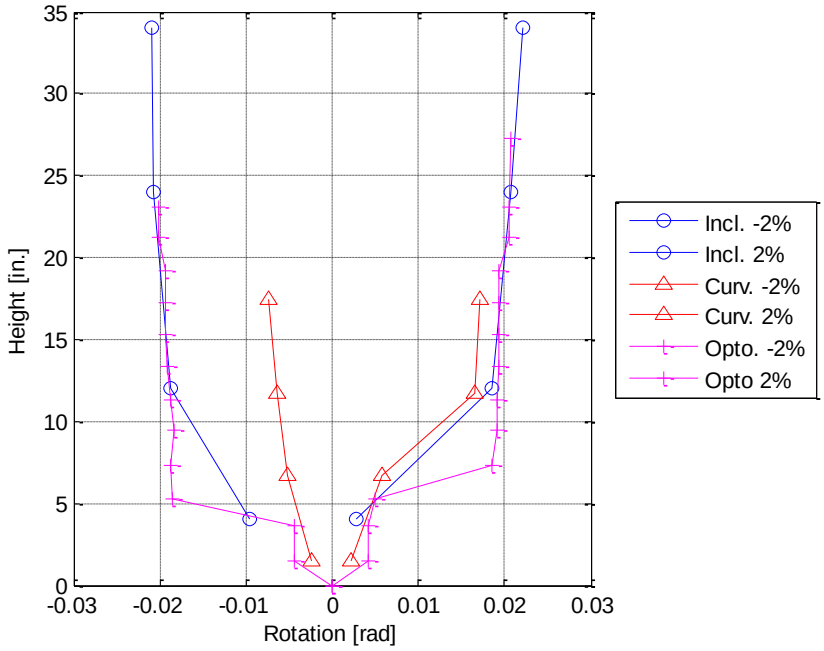


**Figure 5-17: Rotation comparison between instruments at ±2% drift in specimen PreT-BS.**

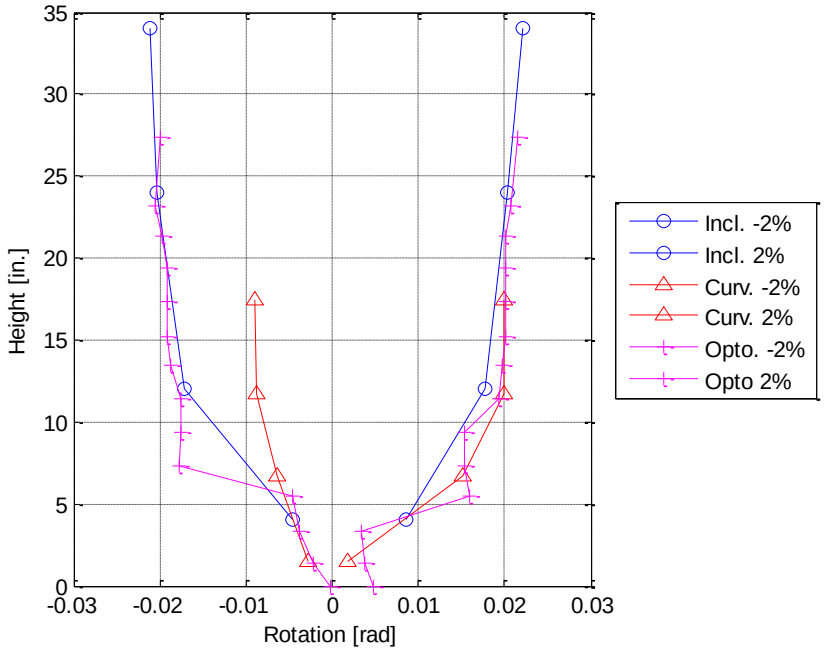


**Figure 5-18: Rotation comparison between instruments at ±2% drift in specimen PreT-SS.**

From Figure 5-17 and Figure 5-18 it can be seen that the Optotrac System and the inclinometers gave very similar results. The curvature rod tracking system gave similar results for the positive drift but

for the negative drift values the results differed greatly from those of the other two systems. They are also different from the positive drift values. The curvature rod values are therefore regarded as untrustworthy, and may have malfunctioned, perhaps by reaching the end of their stroke.

Of all those three instruments the Optotrac System gave the best results because the system provided a finer mesh of readings. However, the data is fragile because it may be lost if the camera is accidentally moved during the test.

The inclinometers provide readings of comparable accuracy, but with a coarser mesh because of the small number of instruments used.

The curvature rod tracking system is capable of giving good results but is susceptible to error if the sensors are not carefully installed.

## 5.5 Column Curvature

The column curvature was measured using two types of instruments. The instruments that were used to measure the curvature were described in Chapter 3; curvature rod system and LED motion capture system.

Results from both those measurements are displayed below. The results from the curvature rods are displayed in Figure 5-19 through Figure 5-20 for both specimens. Note that only the curvatures for drift levels of ±0.3%; ±0.7%; ±1.2%; ±2.0%; ±3.0% and ±4.0% are displayed. Curvatures were obtained from the rotations using Equation (5-6):

$$\varphi_i = \frac{\delta_{i,N} - \delta_{i,S}}{L_i} / H_i \qquad 5\text{-}6$$

where $\varphi_i$ is the calculated average curvature at a given height in the column;

$\delta_{i,N}$ is the measured displacement on the north side of the column;

$\delta_{i,S}$ is the measured displacement on the south side of the column;

$L_i$ is the horizontal length between both linear potentiometers in the height where the curvature is being calculated and

$H_i$ is the initial vertical distance between the curvature rods.

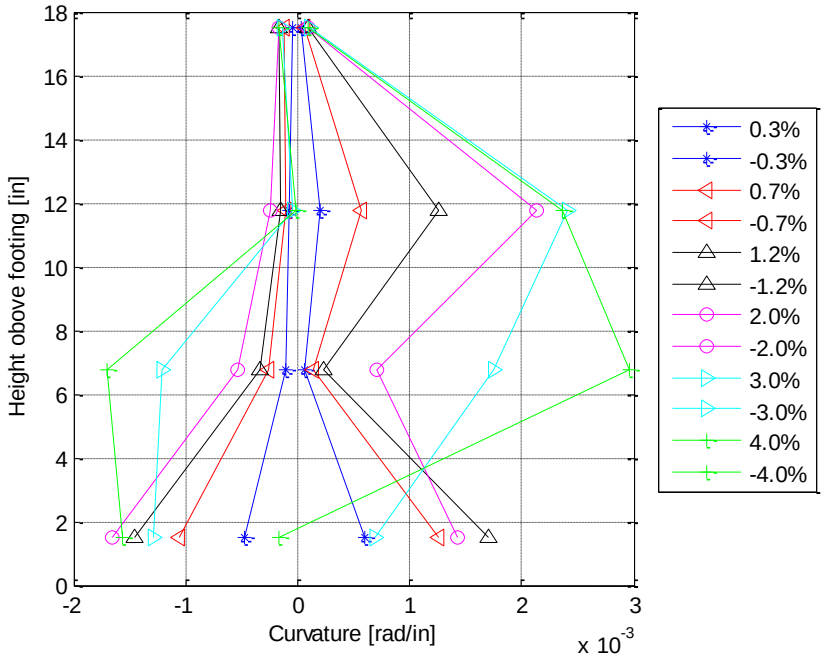


**Figure 5-19: Average column curvature for Specimen PreT-BS.**

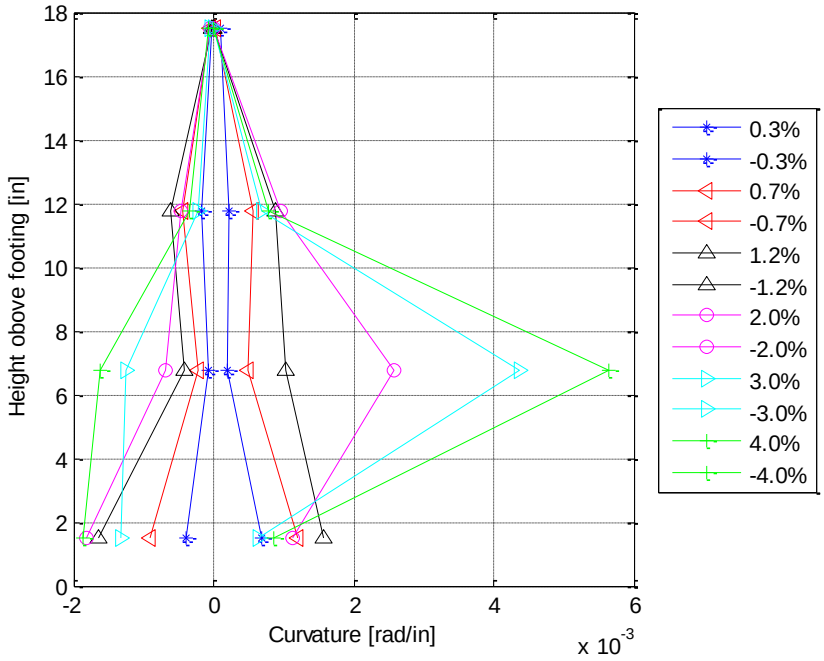


**Figure 5-20: Average column curvature for Specimen PreT-SS.**

The average column curvatures from the Optotrac system are displayed in Figure 5-21 and Figure 5-22.

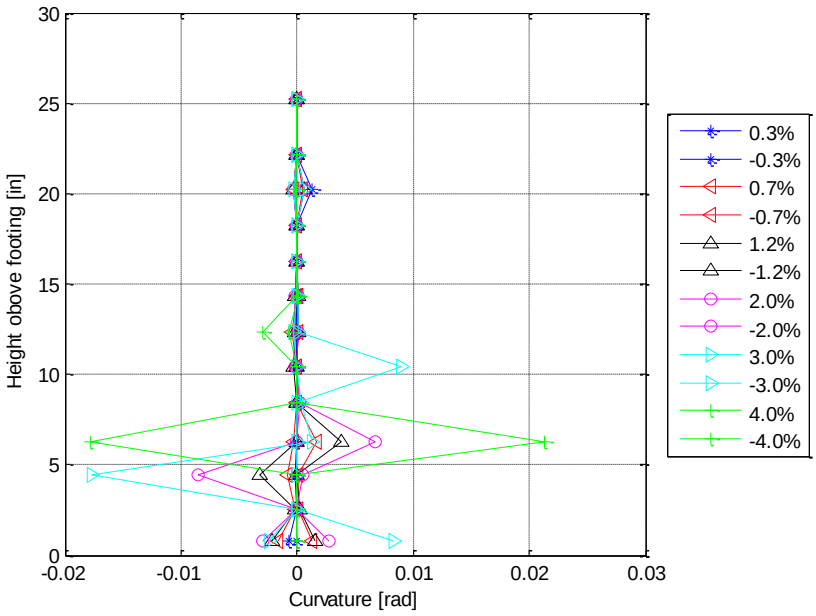


**Figure 5-21: Average column curvature from the Optotrac System for Specimen PreT-BS.**

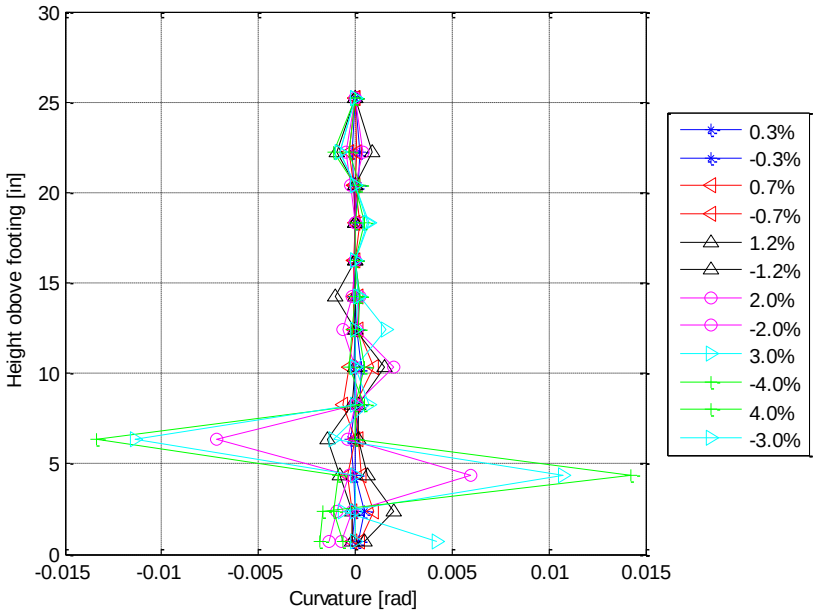


**Figure 5-22: Average column curvature from the Optotrac System for Specimen PreT-SS.**

Those results from the Optotrac System in general give very good results. A few points are anomalous and should be ignored. The readings of all systems were consistent with the existence of the large crack 5 to 7 inches above the base of the columns that was observed during the test.

## 5.6 Strains in Longitudinal Rebars

### 5.6.1 Strain Profile along Columns Height

Strain profiles for the longitudinal bars are shown in Figure 5-23 through Figure 5-26. The strains in the longitudinal reinforcement bars are plotted for specific drift values and at all three levels in the rebar where the strains were measured. These were at elevations of 7 in. below the column-footing interface; at the column-footing interface and 7 in. above the column-footing interface. In the plots height 0 in. corresponds to the height of the column-footing interface, and positive heights correspond to locations above the interface and negative values of the height denote locations below the interface.

The strain gauges all malfunctioned at relatively low drift values compared with former tests performed by Haraldsson et al. (2011) and Davis et al. (2011). Since the major difference between those tests and the present ones is the use of HyFRC , it is likely that that material in some way affected the gauges.

Consequently, only the strain at ±0.3%, ±0.5%, ±0.7% and ±1.0% drift to be consistent with earlier tests. The strain profiles for specimen PreT-BS and PreT-SS are shown in Figures 5-23 and 5-24 respectively.

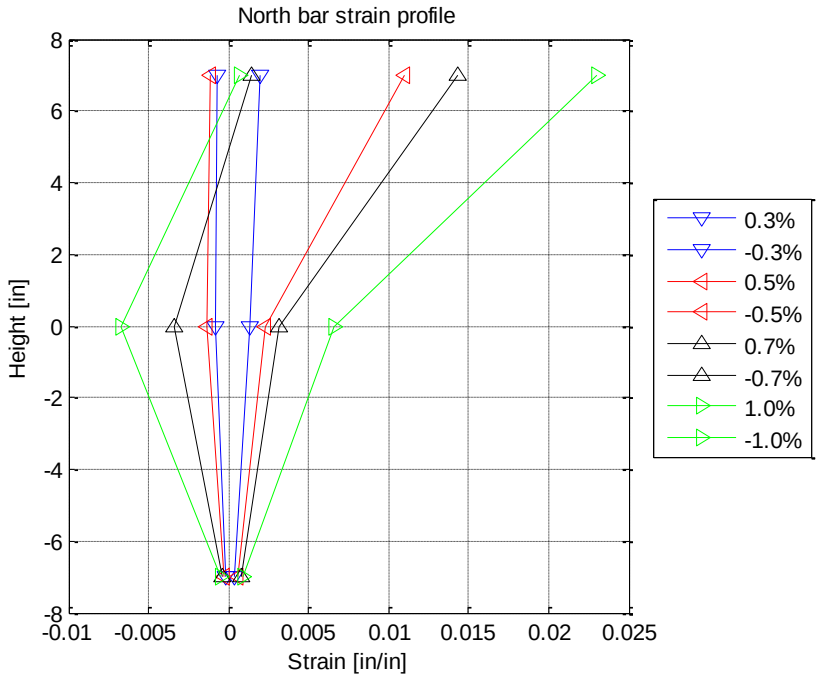


**Figure 5-23: Strain profile of north longitudinal rebar in Specimen PreT-BS.**

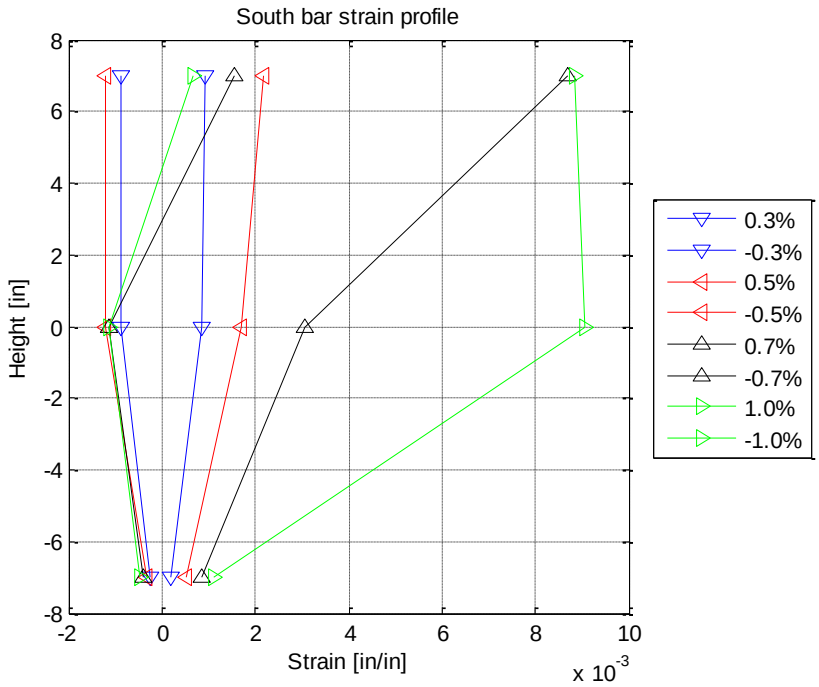


**Figure 5-24: Strain profile of south longitudinal rebar in Specimen PreT-BS.**

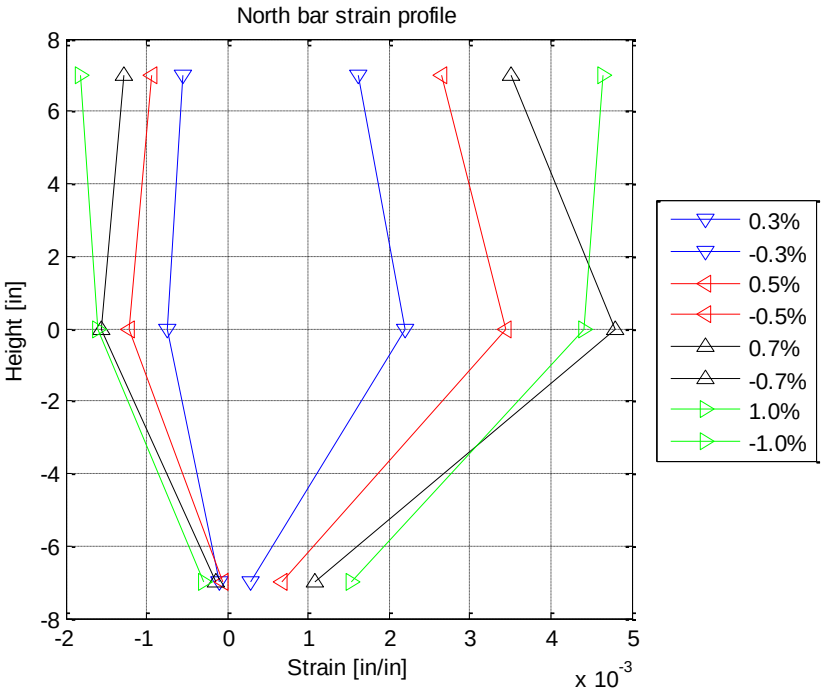


**Figure 5-25: Strain profile of the north longitudinal rebar in Specimen PreT-SS**

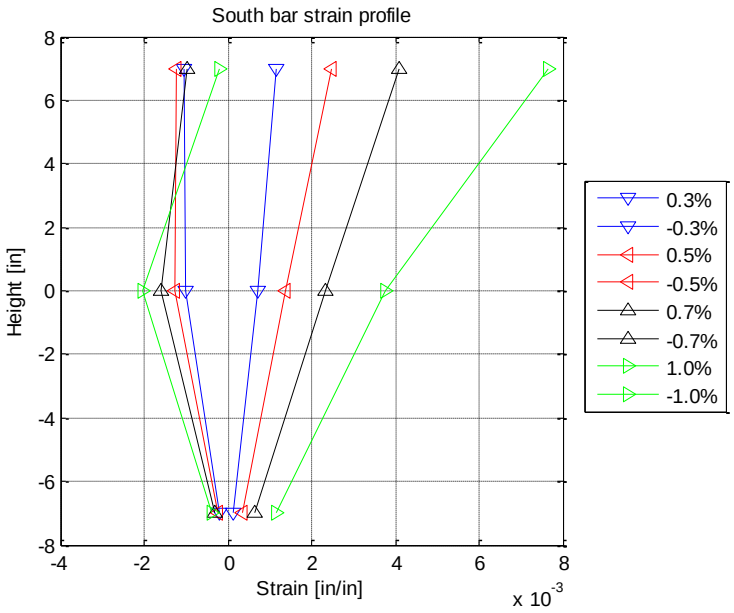


**Figure 5-26: Strain profile of the south longitudinal rebar in Specimen PreT-SS**

### 5.6.2 Strain versus Drift

The strain in both longitudinal rebars that included strain gauge pairs are plotted against drift for all the six places where the strain was measured, in the north and south bars at the column-footing interface; 7 in. above the interface and 7 in. below the interface. The measured strains were plotted over the entire testing history except if the strain gauge broke, in which case the strains were plotted until the gauge broke. The strain gauge pairs at the interface always broke; the strain gauge pairs 7 in. above the interface sometimes broke, and the pairs in the footing never broke. The results from the strain gauges in both longitudinal rebars are displayed in Figure 5-27 through Figure 5-30. Note that the scales of the plots are not all the same.

For any given drift amplitude, the strains are in general larger when the bar in question is in tension. This finding is in agreement with visual observations.

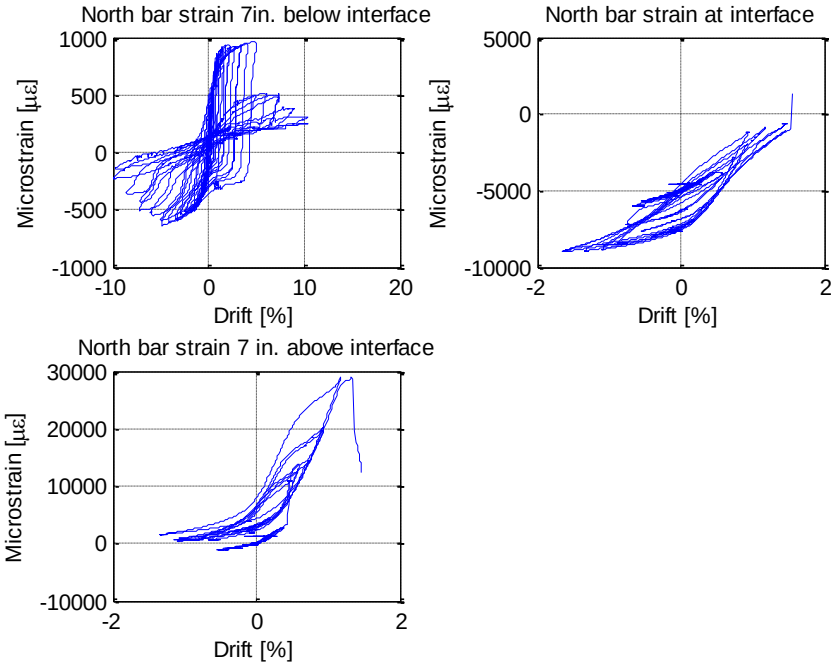


**Figure 5-27: Strain vs. drift in north longitudinal rebar in Specimen PreT-BS at all measured locations.**

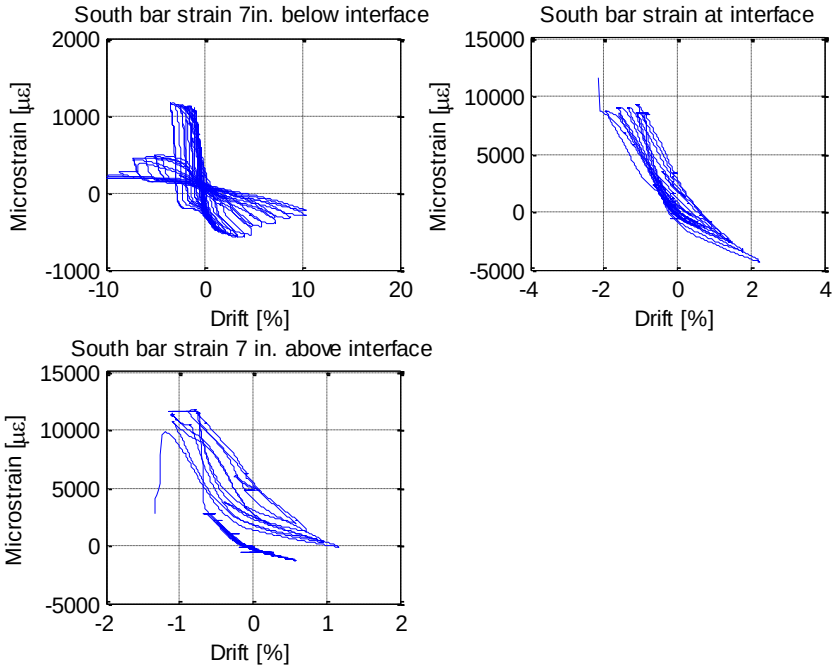


**Figure 5-28: Strain vs. drift in south longitudinal rebar in Specimen PreT-BS at all measured locations.**

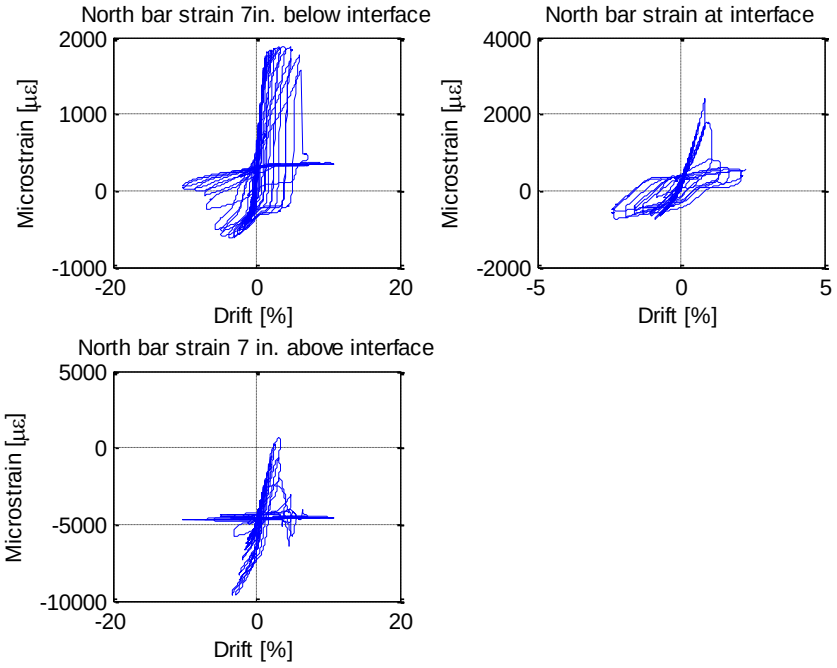


**Figure 5-29: Strain vs. drift in north longitudinal rebar in Specimen PreT-SS at all measured locations.**

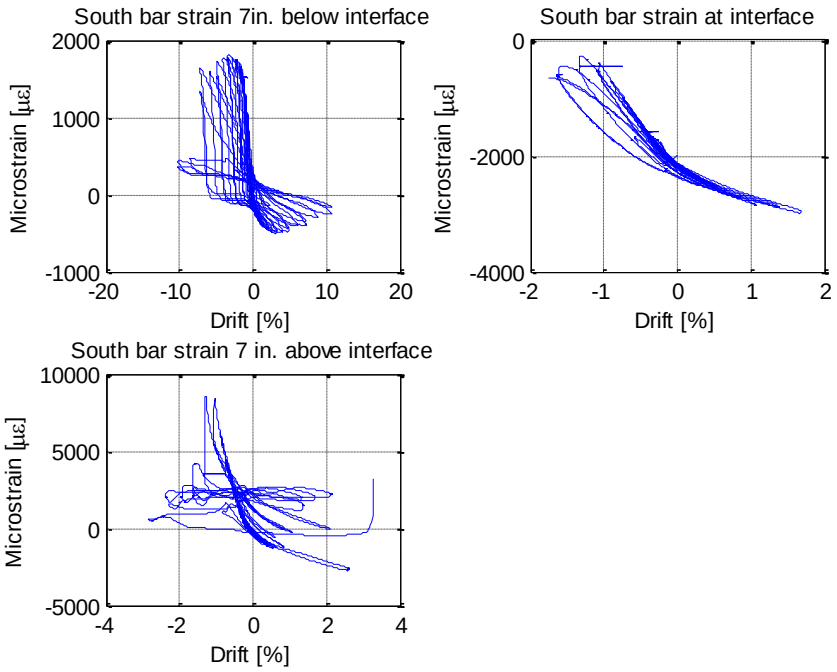


**Figure 5-30: Strain vs. drift in north longitudinal rebar in Specimen PreT-SS at all measured locations.**

## 5.7 Strains in Spirals

The strains in the spiral were measured at four places in each column. Two pairs placed were on each side of the column (north and south side). The pairs were placed about 3 in. and 6 in. above the column-footing interface. The results from the spiral strain gauge pairs are shown in Figure 5-31 and Figure 5-32, plotted against drift. The results are plotted until the strain gauge broke.

The overall pattern of behavior is that the spiral experienced tension stress that increased with drift, in either direction. This is consistent with the presence of compression stress in the concrete core. As the column was displaced back towards zero drift, the stress in the spiral diminished. However, some permanent tension strain and stress accumulated with cycling. This is attributed to the build-up of permanent vertical compressive deformation in the concrete.

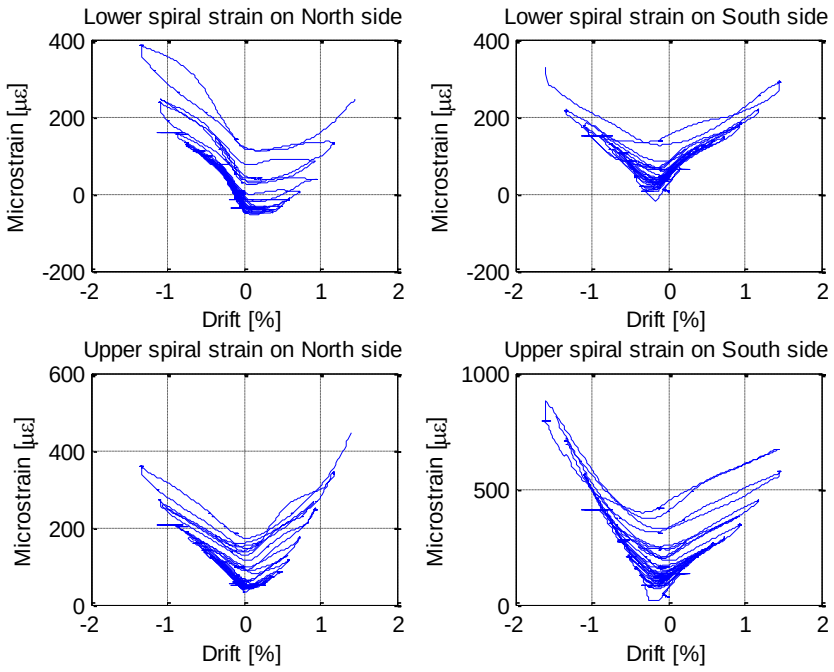


**Figure 5-31: Strain vs. drift in spiral at all four locations measured in Specimen PreT-BS.**

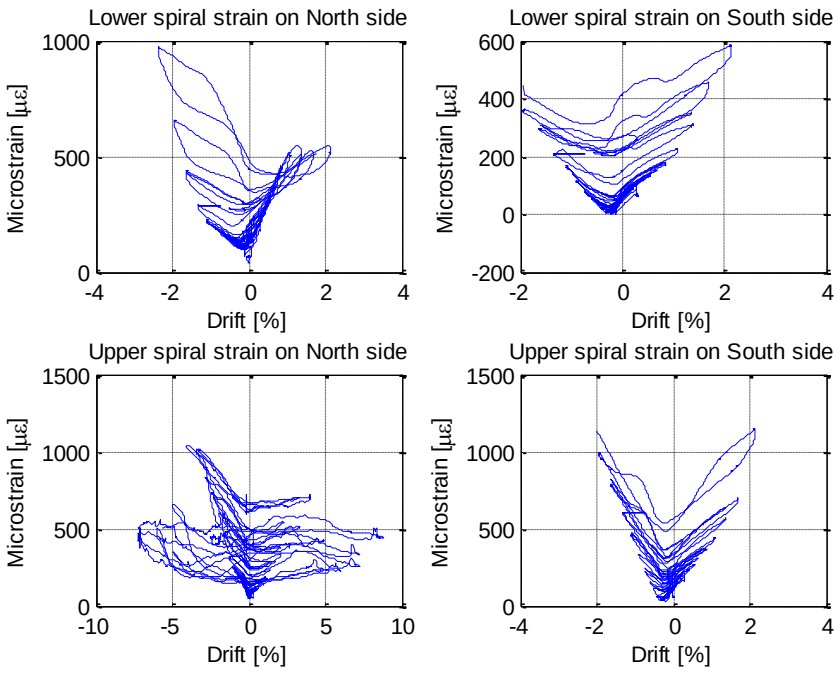


**Figure 5-32: Strain vs. drift in spiral at all four locations measured in Specimen PreT-SS.**

# 6 Analysis

In this chapter the measured responses of the two columns tested (PreT-BS and PreT-SS) are analyzed and compared with the responses of previously tested columns. The comparison tests were performed on an unbonded pretensioned concrete column that used only conventional concrete (Specimen PreT-SF from Davis et al., 2011) and on a non-prestressed precast column with a socket connection (Specimen SF2 from Haraldsson et al., 2011).

## 6.1 Strength Degradation

The strength envelopes for both specimens are shown in Figure 6-1 for both the positive and negative peaks. To ensure that the plot wouldn't be too crowded the results were only plotted for the peak and valley of the second cycle of each set.

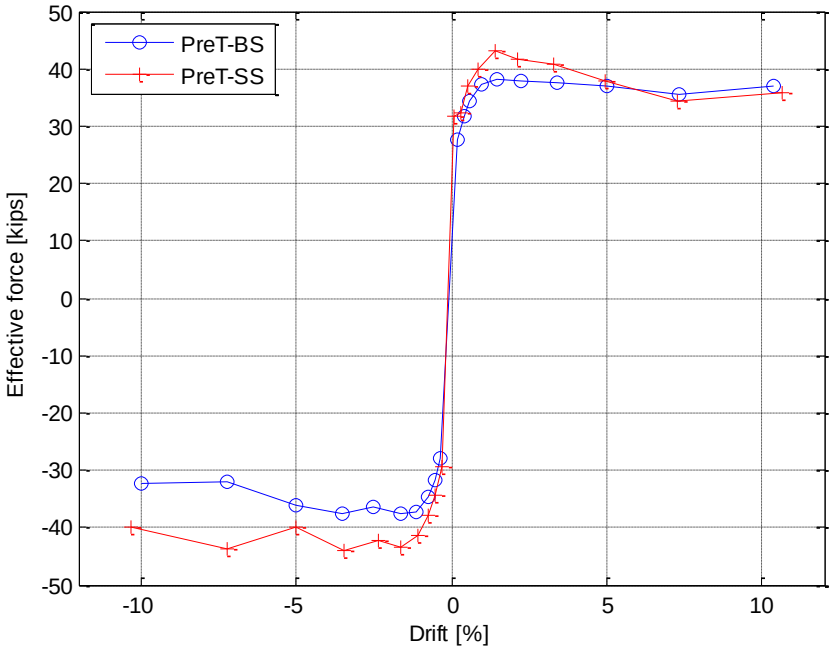


**Figure 6-1: Effective force vs. drift envelopes.**

The envelopes were similar in shape, but the stainless steel specimen was slightly stronger. The strength difference was attributed to the fact that, although the bar sizes were the same for both specimens, the stainless steel was stronger that the black steel (see Figure A - 13 and Figure A - 15). In addition, Specimen PreT-BS lost more strength in the negative direction, and PreT-SS lost more strength

in the positive direction. These differences were small and may have been caused by random differences in the spalling patterns.

Most importantly, the strength degradation was minimal for both specimens. At a 10% drift ratio, the strength loss in the positive direction was 2.9% for PreT-BS and 16.9% for PreT-SS. The corresponding reductions in the negative direction were 14.0% for PreT-BS and 9.0 % for PreT-SS. These reductions can be compared with a common definition of failure, namely a 20% drop in strength from the peak. By that definition, neither column had failed at 10% drift.

To compare the strength degradation for the two specimens tested (PreT-BS and PreT-SS) with the previously tested specimens (PreT-SF and SF2), the envelopes were normalized by dividing the strength ordinates by the peak strength for that specimen. This normalization facilitated comparison, because both the flexural strength of the columns and the elevation of the applied load varied among the specimens.

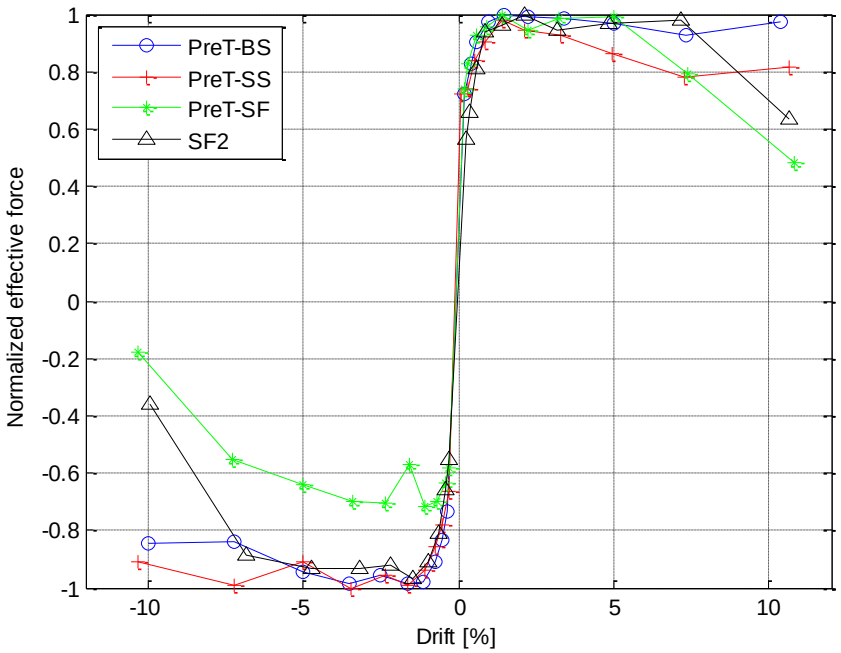


**Figure 6-2: Normalized strength degradation comparison.**

All the specimens reached their maximum absolute force close to ±2% drift. With the exception of the negative direction for Specimen PreT-SF (made with conventional concrete), all four specimens retained almost all of their strength until 5% drift ratio. Between 5% and 10% drift ratio, specimens

PreT-BS and PreT-SS (made with HyFRC) retained more of their strength than the other two specimens. The difference is attributed to the use of the HyFRC, which improved the column performance as it was intended to.

The columns that are compared in Figure 6-2 were all designed as bridge columns. For the design basis earthquakes, such columns are usually expected to be subjected to a maximum drift ratio of about 1-2%. For the maximum considered earthquake, the drift ratio might be in the range of 3-4%. If a bridge reached a drift ratio higher that 4% in a given earthquake it might impose some significant losses in strength for the PreT-SF column, but the other columns would retain their strength to much larger drift values.

## 6.2 Energy Dissipation

The energy dissipation was calculated for both columns by finding the area enclosed by each loading cycle. The numerical integration was done using the trapezoidal method.

### 6.2.1 Energy Dissipation of Specimens Tested

Figure 6-3 shows the energy dissipated in each cycle and Figure 6-4 the cumulative energy dissipated for specimens PreT-BS and PreT_SS.

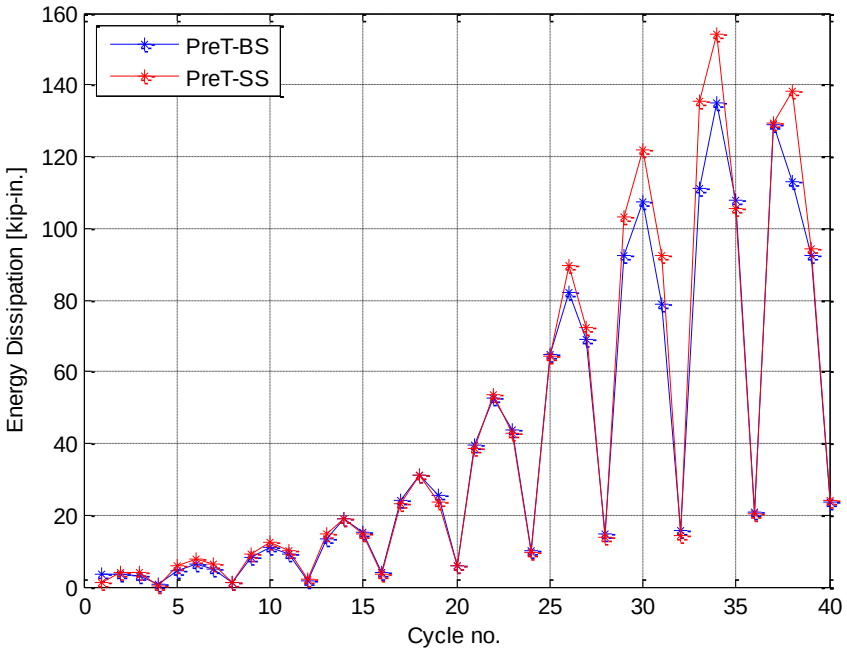


**Figure 6-3: Dissipated energy per cycle.**

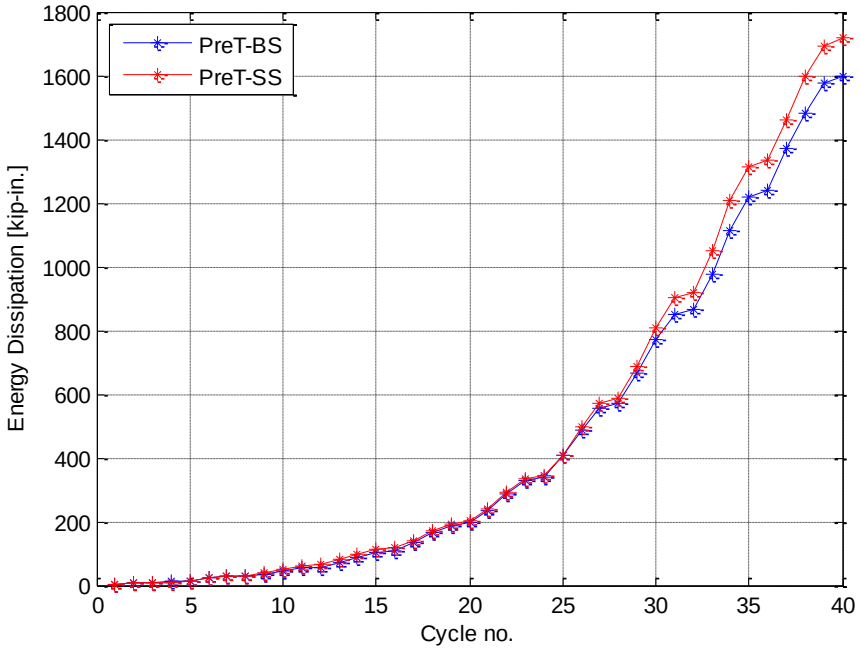


**Figure 6-4: Cumulative dissipated energy history.**

In Figure 6-3, each set of our cycles show the same pattern. The largest energy dissipated occurred in the second cycle, and the smallest occurred in the fourth cycle. This difference was attributable to the displacement history, in which the maximum displacements for all four cycles within each set had a ratio of 1.0, 1.2, 1.2 and 0.4, respectively. The energy dissipated in the third cycle was consistently lower than that dissipated in the second, because the second cycle caused some damage.

From Figure 6-3 and Figure 6-4, it can be seen that the PreT-SS specimen dissipated slightly more energy than the PreT-BS specimen, particularly in later cycles. That small difference was expected, because the stainless steel reinforcement bars used for longitudinal reinforcement in Specimen PreT-SS were both stronger and more ductile than the regular black steel in PreT-BS. The total energy dissipated by the PreT-BS specimen was calculated to be 1598 kip-in and for the PreT-SS specimen 1718 kip-in, a difference of only 7.5%. This small increase is not large enough to justify the additional expense and reduced commercial availability of stainless-steel bars.

### 6.2.2 Energy Dissipation Comparison with Previous Tests

To compare the energy dissipation among the specimens, the energy dissipated was normalized by dividing the energy dissipated per cycle by the area of a rectangular box defined by the maximum

($F_{max}$) and minimum forces ($F_{min}$) during the entire test, and the maximum ($\Delta_{max(i)}$) and minimum displacements ($\Delta_{min(i)}$) during the cycle. The normalization concenpt is illustrated in Figure 6-5.

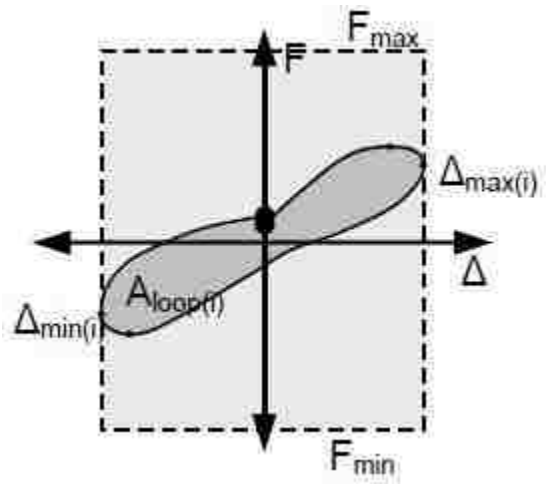


**Figure 6-5: Normalization method for energy dissipation, Pang et al. (2008).**

The normalized dissipated energy dissipated are plotted against cycle number in Figure 6-6. All four specimens were subjected to similar displacement histories. At the end of the SF2 test, the last cycle was not applied, so the cumulative curve for the specimen ends at Cycle 39.

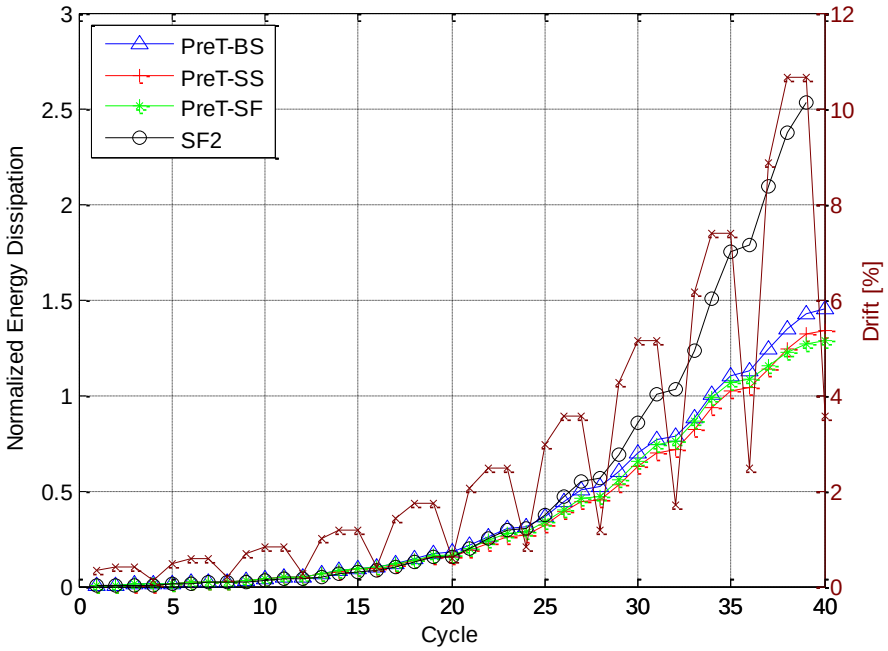


**Figure 6-6: Comparison on normalized cumulative dissipated energy. The brown line applies to the right axis and shows the corresponding maximum targeted drift per cycle.**

The normalized energy dissipation for all the four specimens was similar until the 25th cycle (3.0% target drift ratio). Then the SF2 specimen started to dissipate more energy more than the other specimens and at the end of the test, the energy dissipation for SF2 was much higher. That result was expected, because the SF2 specimen had no prestressing to re-center the column. Such prestressing reduces the area enclosed by each cycle, as can be seen in Figure 1-4. The normalized energy dissipation for the three pretensioned specimens was similar.

## 6.3 Equivalent Viscous Damping

The Equivalent Viscous Damping (EVD) is closely related to the Energy Dissipated per Cycle. It is defined (e.g. Chopra, 2007) by:

$$\zeta = \frac{2}{\pi} \cdot \frac{A_{loop}}{A_{box}} \qquad 6\text{-}1$$

where $A_{loop}$ equals the area enclosed by the force displacement curve of each cycle. $A_{box,loop}$ is the rectangular box that circumscribes each individual force-displacement loop. The EVD was calculated for the first cycle of each set for all four specimens. The results are plotted against cycles in Figure 6-7 and versus drift ratio in Figure 6-8.

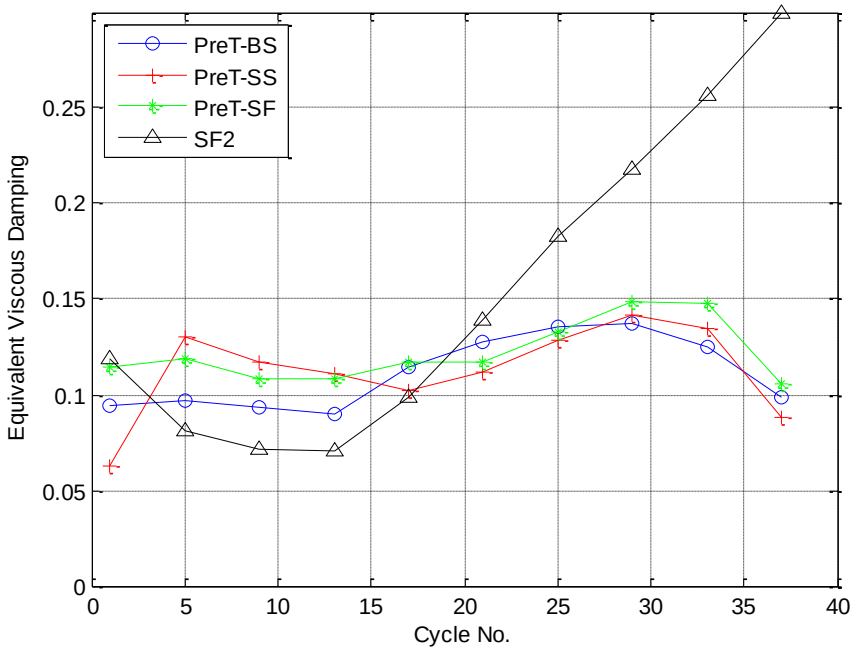


**Figure 6-7: Equivalent viscous damping versus cycle number comparison.**

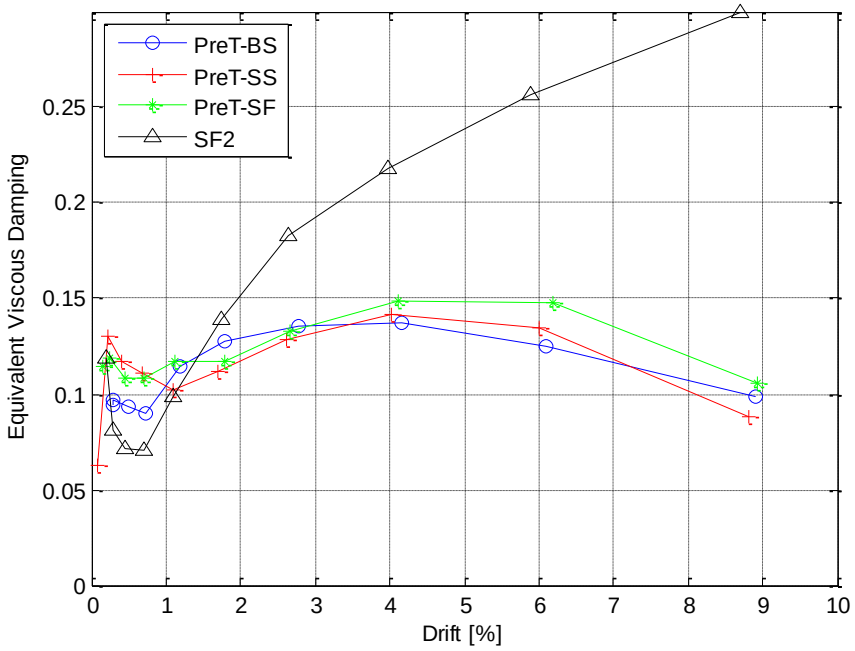


**Figure 6-8: Equivalent viscous damping versus drift ratio comparison.**

Those calculated equivalent viscous damping for the three pretensioned specimens was almost identical to each other except for the first 10 cycles (up to a drift ratio of approximately 1%). Calculations for these low drift ratios are more susceptible to errors. In Equation 6-1, $A_{box,loop}$ becomes much smaller than for the larger drift ratio cycles and therefore small changes in the value for $A_{box,loop}$ results in more change than when the value of the drift ratio is higher.

At drift ratios above 2%, the damping of the pre-stressed specimens differed greatly from the non-prestressed specimen. The equivalent viscous damping of the pre-stressed specimens was much closer to being constant (ranging from 10%-15%) than for Specimen SF2 (10%-30%). It is not surprising that the SF2 specimen has much higher values for the EVD (at drift larger than 2%), because the specimen did not have any prestressing to re-center the column, and it did have more mild steel. However, whereas, SF2 has almost three times the rebar steel, it only generated about twice the EVD at 6% drift.

## 6.4 Re-Centering of Columns

One of the main goals of both columns was to have superior re-centering effects compared to conventional concrete columns.

### 6.4.1 Re-Centering Ratio

A method to approximate the re-centering ability of the columns was developed by Hieber et al. (2005). The method calculates a ratio from the vertical forces that are working on the column. The ratio compares the restoring force from the pre-stressing strands (and the axial load) to the resisting forces from the longitudinal steel. The forces can be seen in Figure 6-9.

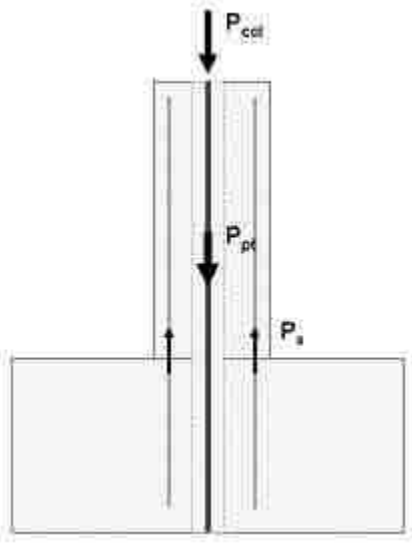


**Figure 6-9: Forces used to calculate the re-centering ratio, Cohagen et al. (2008).**

The re-centering ratio is calculated by summing the moment about the centroid of the compression block and then dividing the re-centering moment by the resisting moment. The re-centering moment can be approximated as:

$$M_{re-centering} = (P_{col} + P_{pt}) \cdot \alpha D \quad 6\text{-}2$$

Assuming that all of the mild steel is in tension, the resisting moment can be approximated as:

$$M_{resisting} = P_s \cdot \alpha D \quad 6\text{-}3$$

In those two equations αD is the distance from the center of the column to the centroid of the concrete compression stress block. The ratio of these moments is defined as the re-centering ratio:

$$\lambda_{re} = \frac{M_{re-centering}}{M_{resisting}} = \frac{P_{col} + P_{pt}}{P_s} = \frac{P_{col} + A_p \cdot f_{p0}}{A_s \cdot f_y} \quad 6\text{-}4$$

In Equation (6-4), the moments are computed at zero drift, after the column has returned from peak drift. It is thus assumed that the stress in the prestressing steel is the initial value of $f_{p0}$. Each bar is also assumed to be stressed to $f_y$ in compression. Since each bar has experienced a different strain history prior to returning to zero drift, this assumption is unlikely to be true. Therefore, Eq. (6-4) provides a simple, if not very accurate, estimate of the column's re-centering characteristic.

The re-centering ratio was calculated for both columns tested (PreT-BS and PreT-SS) and the two previously tested columns (PreT-SF and SF2).

**Table 6-1: Design re-centering ratio and actual re-centering ratio of columns.**

| Specimen | Design re-centering ratio | Actual re-centering ratio |
|---|---|---|
| PreT-BS | 3.5 | 3.1 |
| PreT-SS | 3.2 | 2.3 |
| PreT-SF | 3.5 | 3.1 |
| SF2 | 0.8 | 0.7 |

In Table 6-1 the nominal values for $f_y$ have been used to calculate the design re-centering ratio, and the actual values for $f_y$ were used to calculate the actual re-centering ratio. The actual values for the yield stress (for specimens PreT-BS and PreT-SS) can be found in Sections 5.1.3 and 5.1.4.

### 6.4.2 Normalized Cross-over Displacement

A measure of the column's tendency to re-center (as evaluated from pseudo-static tests) is the Normalized Cross-over Displacement (NCOD), illustrated in Figure 6-10. The cross-over displacement is defined as the displacement at which the effective force returns to 10% of the yield force after reaching a larger displacement (Haraldsson et al. 2011). The normalized Cross-Over Displacement is defined by dividing the range of cross-over displacements by the range of peak displacements, as shown in Eq. 6-5.

$$\text{Normalized Cross} - \text{Over Displacement} = \frac{\Delta_{\text{cross1}} - \Delta_{\text{cross2}}}{\Delta_{\text{peak1}} - \Delta_{\text{peak2}}} \qquad 6\text{-}5$$

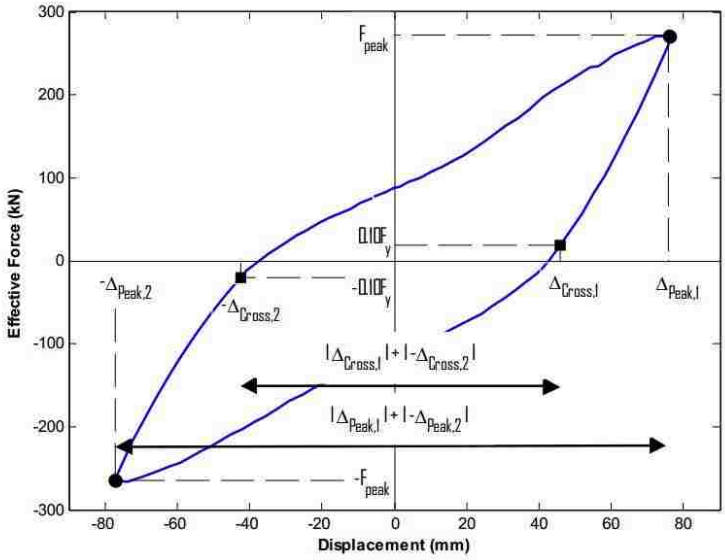


**Figure 6-10: Definition of the cross-over displacement, Haraldsson et al. (2011).**

Using this definition, an NCOD of 0.0 indicates perfect re-centering, and 1.0 indicates no re-centering, for which the residual drift is equal to the peak drift.

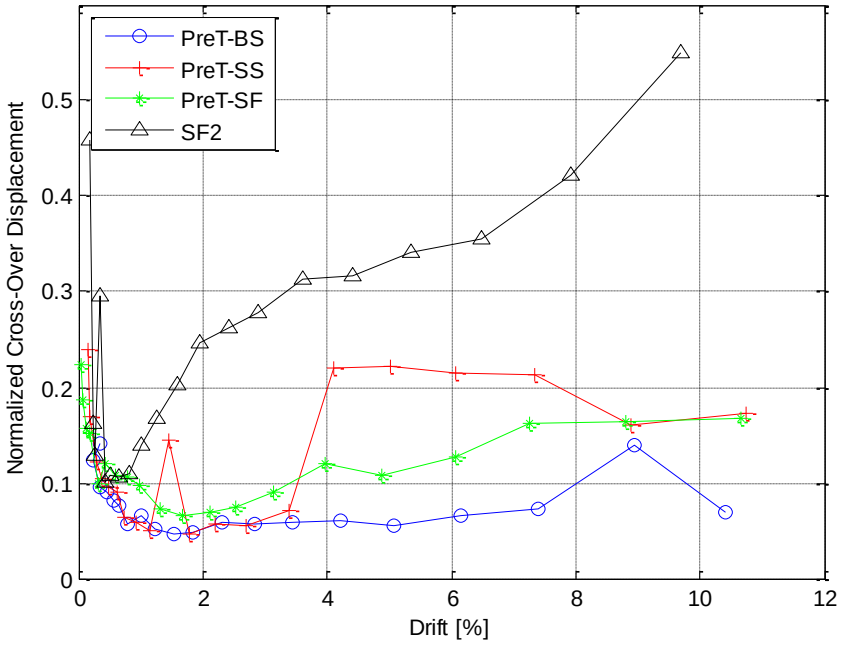


**Figure 6-11: Normalized cross-over displacement comparison.**

In Figure 6-11, the normalized cross-over displacements for two tested specimens are compared with the results of the two specimens used for comparison, SF2 and PreT-SF. Only the results for the first

and second cycles of each set were plotted. That was done so the plots wouldn't be too crowded with data points. Figure 6-11 shows the following trends:

- NCOD values at low drifts (say, less than 1%) are not reliable. This is likely because little yielding has occurred, and other devices, such as the friction in the PTFE slider at the column head, might have a relatively greater influence prior to yielding. These values are also not important because the absolute residual displacement at such drifts is small.
- The PreT columns, as a group, have significantly lower NCOD values at drifts higher than about 1%. This difference in behavior is consistent with the difference in re-centering ratios.
- PreT-SS show a sudden increase in NCOD at 4% drift. This argues against the use of stainless steel in the columns, unless smaller bars are used to compensate for the higher strength. Smaller bars have the potential for buckling at lower drifts.
  PreT-BS (made with HyFRC and conventional "black" bars) showed a lower NCOD than PreT-SF (made with conventional concrete and black bars.) This suggests that HyFRC helps to reduce residual drift.

One point on the PreT-SS curve (at about 1.6% drift) appears to be anomalous. It is most likely the result of an erroneous reading.

## 6.5 Slipping and Yielding of Strands

The performance of the strands was evaluated using the strain gages on the unbonded length of the strands and the load cells at the ends.

### 6.5.1 Strand Yielding

The strands were monitored by strain gauges attached near the center of the un-bonded region. The epoxy coating was ground off the strands to permit attachment of the gages, so it is possible that some steel was also removed and that the strand section was slightly smaller at the gages.

The results from the strain gauges are displayed in Figure 6-12 and Figure 6-13. In the plots, the nominal strand yield strain of 0.0087 in./in. (based on $f_{py}$ = 250 ksi and Ep = 28600 ksi) is also shown.

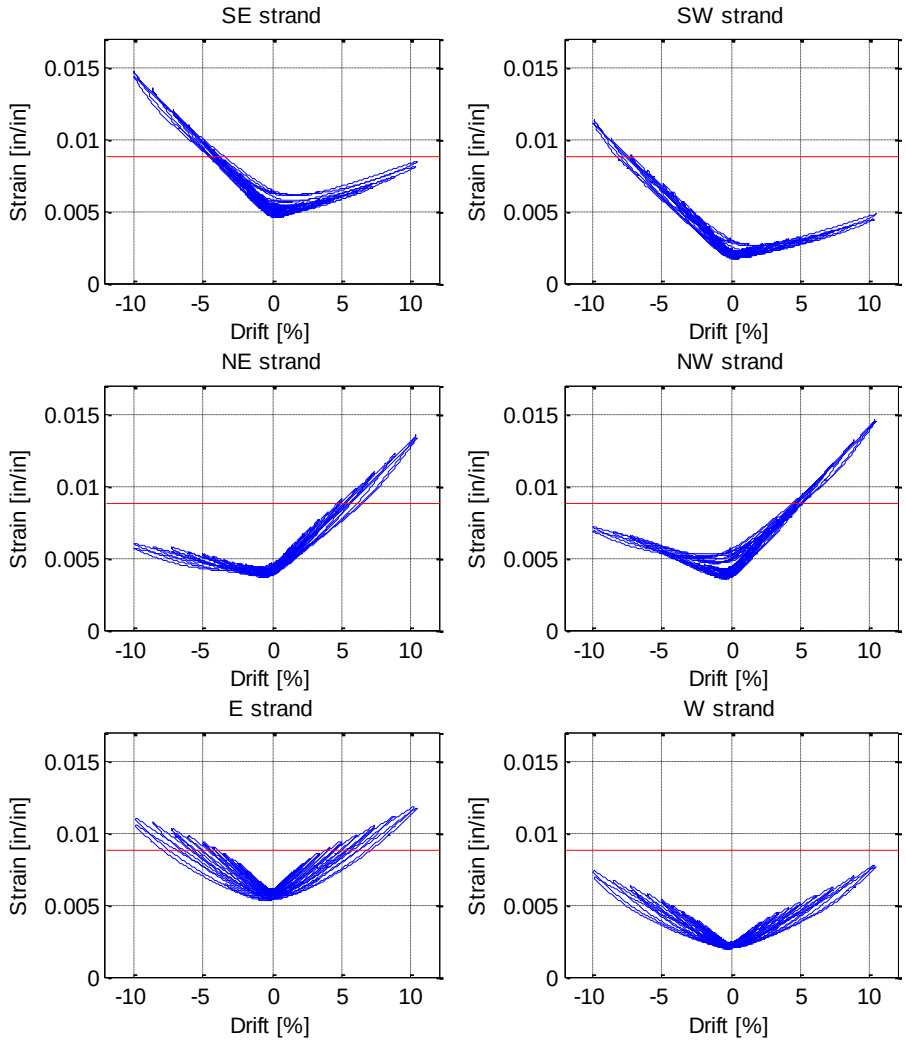


**Figure 6-12: Strand strain gauge data versus drift (blue) and estimated yield strain (red) for specimen PreT-BS.**

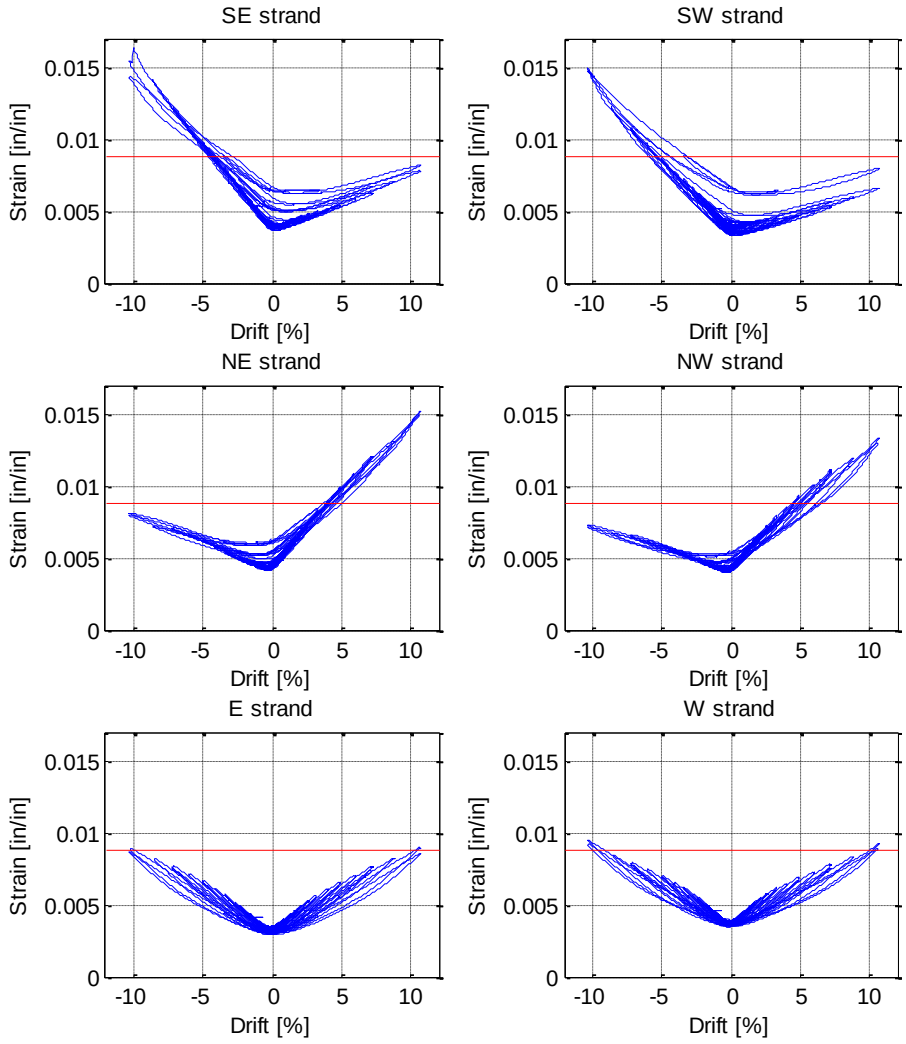


**Figure 6-13: Strand strain gauge data versus drift (blue) and estimated yield strain (red) for specimen PreT-SS.**

Figure 6-12 and Figure 6-13 have the following features:

- Each figure has a similar V-shape; the strand strain increases with either positive or negative drift. The strands on the transverse axis (E and W strands) show a symmetric response. Those nearer one face show an asymmetric response in which they elongate more when that side is placed in tension. This behavior is consistent with their locations.
- The E and W strands appeared to just remain elastic, whereas in the off-axis strands the strain reached yield at approximately 5% drift ratio and exceeded it by a considerable margin at 10% drift ratio.

- The strain at zero drift changes slightly with cycling. The change is attributed to a combination of slip at the ends (which reduced the remaining tension strain) and yielding, which tends to increase the strain. The change is always positive (i.e. increasing tension strain) and is larger in the off-axis strands. Both results indicate that yielding was more influential than slipping.
- It can be seen that all strands except one yielded during the test. The two strands in the center of the column were closest to not yield. The east strand of the PreT-BS specimen yielded at about 5% drift, but the west strand never yielded. On the other hand, both the east and west strands in the PreT-SS specimen yielding during the last set. From this data it is easy to see that the outermost strands pick up more strain and therefore contribute more to the re-centering of the column and are more likely to yield.

### 6.5.2 Strand Slipping

To detect possible slip at the end of the strands, a load cell was placed between the screw thread device (STD) and the chuck on each strand (Section 3.2.3). Chucks were installed at both ends, but a load cell was installed at only one end. If a strand slipped over its whole bonded length (of 24”) the load cell would pick up the load. Monotonic tests on the same strand (Jimenez et al., 2012) showed that the anchorage length of the strand should be long enough (24’’ for 3/8’’ strand), but cyclic loading may be more damaging.

Figure 6-14 and Figure 6-15 show the force in each load cell on every strand in both tests. A change in force indicates partial strand slip. In the test of the PreT-BS specimen all the load cells functioned. In the tests of the PreT-SS specimen, the load cell on the south east strand did not work properly (probably a connection problem), so the forces are not are not shown for that strand.

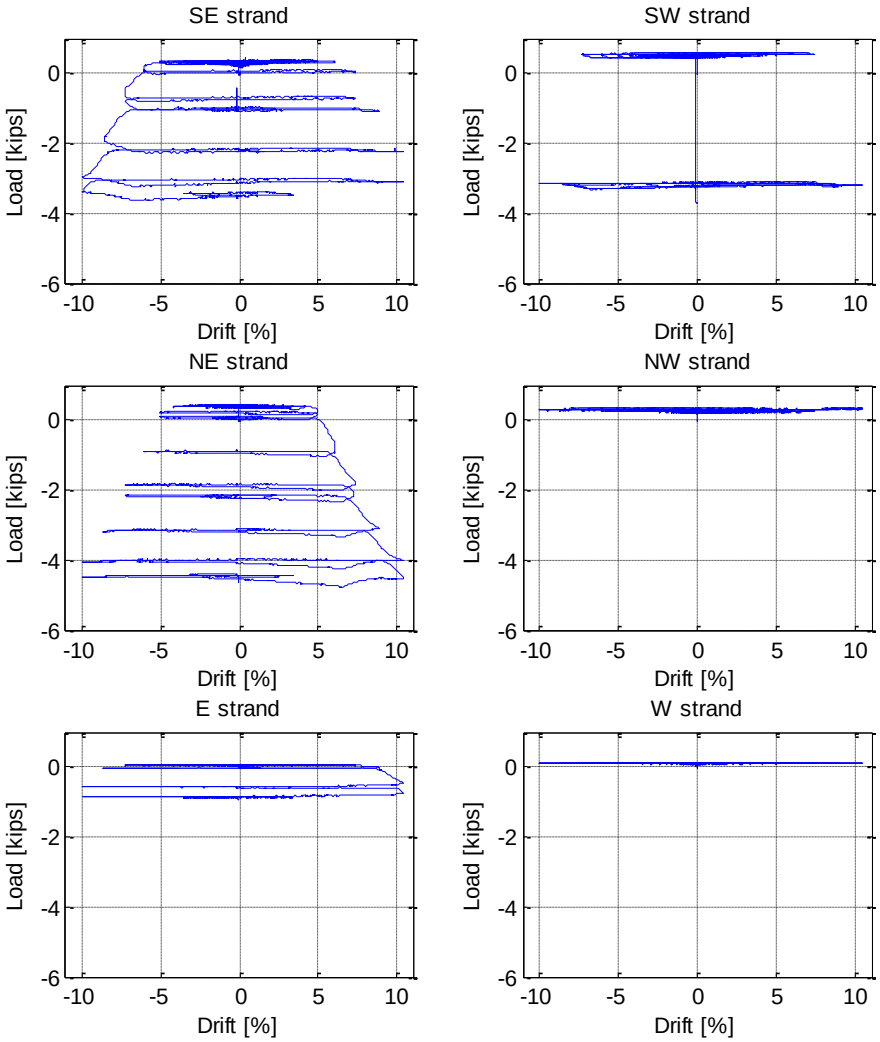


**Figure 6-14: Load vs. drift on strand load cells for specimen PreT-BS.**

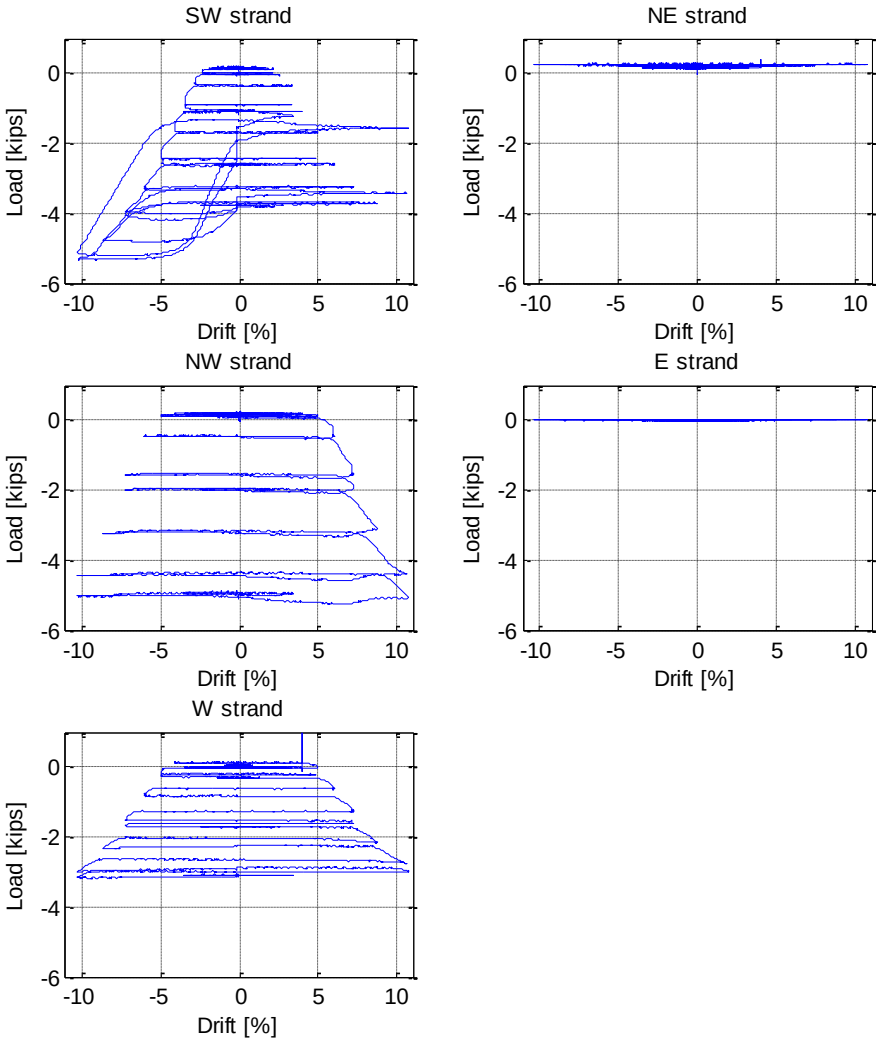


**Figure 6-15: Load vs. drift on strand load cells for specimen PreT-SS.**

Figure 6-14 and Figure 6-15 show that some slip occurred in seven of the eleven strands with functioning load cells. The slip occurred below a drift ratio of 5% in only one strand. As shown in Section 6.5.1, the strand yielded at about 5% drift, so the first slip coincided approximately with strand yield. Given that the bond stresses were artificially high, because the strand diameter was larger than the correct scaling would require, this result is encouraging. However a closer investigation is desirable of the cyclic bond properties of the strand to be used.

The fact that some strands did not slip at all and others lost as much as 5 kips suggests considerable variation in bond strength from one strand to another. This reflects the variability observed

by other researchers (e.g., Cousins et al. 1990) for black strand, although the surface conditions of black and epoxy-coated strand might be expected to differ.

The bond capacity of the stand can be estimated from the results. In the worst case (PreT-SS, NW strand); the load cell read 5.28 kips at 10% drift ratio. At that time the strain was 0.014 in./in. If the corresponding stress is taken as 250 ksi (yield stress), the force in the strand was 21.5 kips, of which the chuck was resisting 5 kips and the bond, 16.5 kips. The average bond stress was then 580 psi. To anchor a strand stressed to 250 ksi by bond alone would have required a bonded length of 31.3 inches, or $L$ = 83 $d_b$. Note that ACI procedures lead to a development length of approximately 150 $d_b$.

In the prototype, the length available would be approximately 48 in., so the maximum permissible strand diameter would be $d_b$ = 48/83 = 0.575 inches. Thus the use of ½" diameter strand in the prototype would lead to anchorage without slip. The safety margin associated with this conclusion depends on the variability of bond capacity among strands. However the foregoing estimate was made using data from the worst case of the 11 available, and still has a safety margin of 0.575/0.5 = 1.15.

## 6.6 Column Stiffness

The effective stiffness of the columns was calculated by finding the secant stiffness at first yield of the reinforcement:

$$\text{Effective Stiffness} = \frac{F_{eff,y}}{\Delta_y} \quad \text{6-6}$$

where $F_{eff,y}$ and $\Delta_y$ are the effective force and displacement at first yield. The yield point was defined by Elwood and Eberhard (2009) as the point where tensile yield was first observed in the longitudinal rebar or the concrete reached a strain on 0.002, whichever occurred first. The effective stiffness was calculated in both north and south direction, and then the results where compared to the results for specimens PreT-SF and SF2.

**Table 6-2: Results from the column secant stiffness at first yield.**

| Specimen | North Direction Stiffness [kip/in.] | South Direction Stiffness [kip/in.] | Average Stiffness [kip/in.] |
|---|---|---|---|
| PreT-BS | 128 | 116 | 122 |
| PreT-SS | 146 | 112 | 129 |
| PreT-SF | 180 | 175 | 178 |
| SF2 | 127 | 149 | 138 |

The columns' effective flexural rigidity was also calculated using the Equation 6-7.

$$EI_{eff,meas} = \frac{F_y \cdot l^3}{3 \cdot \Delta_y} \quad 6\text{-}7$$

where $F_y$ is the effective force at first yield, l is the length of the column from the column-footing interface to the center of the actuator and $\Delta_y$ is the measured displacement at the actuator height at first yield. Those values were then compared to the recommendations of Elwood and Eberhard (2009) using this equation.

$$\frac{EI_{eff,calc}}{EI_g} = \frac{0.45 + 2.5 \cdot \frac{P}{A_g \cdot f'_c}}{1 + 110 \cdot \frac{d_b}{D} \cdot \frac{D}{a}} \quad 6\text{-}8$$

where P is the axial load on the column, $A_g$ is the gross cross sectional area of the column, $f'_c$ is the compressive strength of the concrete (weighted average was used for the concrete in the plastic hinge region), $d_b$ is the bar diameter, l is the cantilever length (height from mid actuator height to column-footing interface) and D is the column diameter. The unbonded prestressing force was treated as extra axial load on the column. When the column displaces, the strands take up more force and therefore the prestress force increases, but at yield, the column displacement is very small and therefore the increase in the prestress force was ignored. Table 6-3 compares the measured and calculated values of the modulus of rigidity for both columns tested and the columns used for comparison.

**Table 6-3: Comparison of measured and calculated EI.**

| Specimen | $EI_{eff,meas}/EI_g$ [kip-in$^2$] | $EI_{eff,calc}/EI_g$ [kip-in$^2$] | Difference [%] |
|---|---|---|---|
| PreT-BS | 0.30 | 0.34 | 13 |
| PreT-SS | 0.34 | 0.34 | 0 |
| PreT-SF | 0.31 | 0.39 | 25 |
| SF2 | 0.28 | 0.29 | 4 |

## 6.7 Shear Strength of Columns

The shear strength of the columns was estimated by using equations from ACI 318-11, which are presented here as equations (6-9) through (6-11)

$$V_c = 2 \cdot \left(1 + \frac{N_u}{2000 \cdot A_g}\right) \cdot \sqrt{f'_c} \cdot b_w \cdot d \quad 6\text{-}9$$

$$V_s = \frac{A_v \cdot f_{yt} \cdot d}{s} \quad 6\text{-}10$$

$$V_n = V_c + V_s \quad (6\text{-}11)$$

where $V_n$ = is the nominal shear strength

$V_c$ = the contribution from the concrete and

$V_s$ = the contribution from the steel.

$N_u$ = the axial load on the specimens (here taken as axial load and the pre-stressing load and both calculated with initial prestressing load and the yielded prestressing load),

$A_g$ = the gross cross sectional area of the specimens,

$f'_c$ = the compression strength of the concrete,

$b_w$ = the diameter of the column,

d = the distance from the outermost side of the compression face to the center of the tension steel,

$A_v$ = the area of the spiral reinforcement,

$f_{yt}$ = the yield strength of the spiral and

s = the spacing of the spiral reinforcement.

The results are displayed in Table 6-4 and compared to the demands on the columns.

**Table 6-4: Results for shear strength calculations**

| | $V_c$ [kips] | $V_s$ [kips] | $V_n$ [kips] | $V_{meas}$ [kips] | $V_{meas}/V_n$ |
|---|---|---|---|---|---|
| **PreT-BS – initial** | 70.0 | 89.4 | 159.4 | 41.5 | 0.26 |
| **PreT-BS – yield** | 73.7 | | 163.1 | | 0.25 |
| **PreT-SS – initial** | 71.0 | 89.4 | 160.4 | 46.6 | 0.29 |
| **PreT-SS – yield** | 74.8 | | 164.2 | | 0.28 |

For both columns, the nomincal shear strength capacity was much higher that the demand. That was expected since no shear failure was observed during the testing.

## 6.8 Flexural Strength of Columns

The flexural strength of the columns was compared with the observed flexural strength in Table 6-5. The pre-stressing force from the unbonded pre-tensioning was treated as an external force, because the strands are unbonded and do not satisfy strain compatibility. The moment strength was calculated both when the strands were elastic (initial prestressing) and when they were yielded. The concrete was modeled using the Kent-Park concrete model. The longitudinal reinforcement bars were modeled using a trilinear steel model defined by the elastic modulus of the steel, the yield stress of the steel, the strain hardening strain (0.4%), the ultimate strain and the ultimate strength of the steel.

The observed flexural strengths were between the values calculated for the initial strand stress and the values calculated for the yielded strand.

**Table 6-5: Calculated moment strength and observed moment strength for both columns, using initial pre-tensioning force and yielded pre-tensioning force.**

| Specimen | $M_{observed}$ [k-in.] | Strand Condition | $M_{calculated}$ [k-in.] | $M_{observed}/M_{calculated}$ |
|---|---|---|---|---|
| **PreT-BS** | 2718 | **initial** | 2609 | 0.96 |
| | | **yield** | 2889 | 1.06 |
| **PreT-SS** | 3077 | **initial** | 2835 | 0.92 |
| | | **yield** | 3125 | 1.02 |

## 6.9 Comparison with Damage Progression Models

Three damage states of the columns were compared to models proposed by Berry and Eberhard (2004 and 2005). The damage models were developed to estimate the drift values at which certain damage states would be reached in a column. The chosen damage states were: first spalling in the column, buckling of longitudinal rebar, and fracture of longitudinal rebar. The model equations are given as Equations 6-12 through 6-14.

Spalling:
$$\frac{\Delta_{calc,sp}}{L}[\%] = 1.6 \cdot \left(1 - \frac{P}{A_g \cdot f'_c}\right)\left(1 + \frac{L}{10D}\right) \quad 6\text{-}12$$

Bar Buckling:
$$\frac{\Delta_{calc,bb}}{L}[\%] = 3.25 \cdot \left(1 + 150 \cdot \rho_{eff} \cdot \frac{d_b}{D}\right)\left(1 - \frac{P}{A_g \cdot f'_c}\right)\left(1 + \frac{L}{10D}\right) \quad 6\text{-}13$$

Bar Fracture:
$$\frac{\Delta_{calc,bf}}{L}[\%] = 3.5 \cdot \left(1 + 150 \cdot \rho_{eff} \cdot \frac{d_b}{D}\right)\left(1 - \frac{P}{A_g \cdot f'_c}\right)\left(1 + \frac{L}{10D}\right) \quad 6\text{-}14$$

where:

P = axial load, including the load provided by the unbounded pre-stressing strand;

$A_g$ is the gross cross-sectional area of the column;

$f'_c$ is the weighted average compression strength of the HyFRC and the conventional concrete;

l is the distance between the column-footing interface and the mid height of the actuator;

D is the diameter of the column;

$\omega = \rho_s f_{ys}/f'_c$ where

$\rho_s$ is the transverse volumetric ratio and

$d_b$ is the diameter of the longitudinal rebar.

For comparison the models used both the initial pre-stressing force and the fully yielded force to calculate the predicted drift values of the damage states. The results from those calculations are reported in Table 6-6 and Table 6-7.

**Table 6-6: Comparison between predicted and observed drift values of three damage states using the initial pre-stressing force.**

| Specimen | PreT-BS | | | PreT-SS | | | PreT-SF | SF2 |
|---|---|---|---|---|---|---|---|---|
| **Drift ratio [%]** | **Pred.** | **Obs.** | **Obs/Pred** | **Pred.** | **Obs.** | **Obs/Pred** | **Obs/Pred** | **Obs/Pred** |
| **Spalling** | 1.90 | 1.46 | 0.77 | 1.91 | 2.12 | 1.11 | 0.63 | 0.58 |
| **Bar Buckling** | 4.99 | 6.01 | 1.20 | 5.46 | 4.01 | 0.73 | 0.65 | 1.22 |
| **Bar Fracture** | 5.38 | 4.14 | 0.77 | 5.88 | 7.17 | 1.22 | 0.77 | 1.68 |

**Table 6-7: Comparison between predicted and observed drift values of three damage states using the force for the yielded pre-stressing strands.**

| Specimen | PreT-BS | | | PreT-SS | | | PreT-SF | SF2 |
|---|---|---|---|---|---|---|---|---|
| **Drift ratio [%]** | **Pred.** | **Obs.** | **Obs/Pred** | **Pred.** | **Obs.** | **Obs/Pred** | **Obs/Pred** | **Obs/Pred** |
| **Spalling** | 1.86 | 1.46 | 0.78 | 1.86 | 2.12 | 1.14 | 0.63 | 0.58 |
| **Bar Buckling** | 5.36 | 6.01 | 1.12 | 5.34 | 4.01 | 0.75 | 0.65 | 1.22 |
| **Bar Fracture** | 5.77 | 4.14 | 0.72 | 5.75 | 7.17 | 1.25 | 0.77 | 1.68 |

Table 6-6 and Table 6-7 show the damage states models overestimate the measured drift values for the PreT-BS specimen, but they estimate the damage state of the PreT-SS column better. It's very likely that the bar buckling in the PreT-BS specimen happened much earlier than at 6.01% drift ratio

since the first bar fracture happend at 4.1% drift ratio. Also the spalled HyFRC in that specimen didn‘t fall off the column and longitudinal rebars never got totally visible. Therefore it wasn‘t possible to see if any rebar had buckled. So it‘s likely that the buckling occurred before the fracture of the rebar.

The results were compared to the SF2 and PreT-SF by only looking at the ratio observed drift ratio over predicted drift ratio using the yielded strand prediction, since most of the strands were close to being yielded at those drift ratios.

One of the main resons for adding the HyFRC was to delay spalling and bar buckling in the columns. Comparison of the results for specimens PreT-BS, PreT-SS (both with HyFRC) and PreT-SF (conventional concrete) in Table 6-6 and Table 6-7 show that that goal was achieved.

Evaluation of the buckling of the reinforcing bars was not possible because the HyFRC did not fall away from the column after initial cracking, so the bars could not be seen.

# 7 Summary and Conclusions

## 7.1 Summary

This thesis describes the development, design and testing of a new type of column for use in bridge bents located in seismic regions. It constitutes the latest step in a series of designs, each of which builds on previous ones developed at the University of Washington. The overall goal of this research is to develop a bridge bent system that can be constructed rapidly, that offers superior seismic resistance and that suffers little damage during an earthquake.

In all of the designs, the columns are precast and are connected on site to a cast-in-place footing and a precast cap beam. In the first designs, the columns were constructed of precast, but not prestressed, concrete. Haraldsson et al. (2011) developed a socket connection to the footing that is made by erecting the column in the foundation, placing the footing reinforcement, and casting the footing concrete around the column. The longitudinal reinforcement in the column is straight and anchored with mechanical headed anchors, rather than being bent outwards. This feature facilitates transportation as well as improving the flow of forces in the connection region. This socket connection was easy to construct and gave excellent seismic performance, so it has been used with all subsequent designs.

In a second development, Davis et al. (2012) designed and tested a column similar to Haraldsson's, except that it was reinforced with a combination of deformed bar reinforcement and pre-tensioned strands. The deformed bars were all fully bonded. The strands were bonded at their ends but unbonded in the central region of the column by placing a plastic pipe around each one. The unbonded strands remained elastic to high drift ratios and brought the column back to vertical when the lateral load was removed. This re-centering, or absence of residual drift, constitutes an improvement in seismic performance. However, Davis' two columns spalled at a drift ratio lower than that seen in Haraldsson's non-prestressed columns, and the bars buckled also earlier. This behavior was attributed to the additional axial load introduced by prestressing and the fact that the longitudinal reinforcing bars were smaller.

The columns described in this thesis constitute an effort to mitigate this early spalling observed in Davis' tests by using a special concrete, referred to as Hybrid Fiber Reinforced Concrete (HyFRC), which contains heavy dosages of both steel and polypropylene fibers. That material has been shown to

be stronger in tension and more ductile in compression than conventional concrete. It is expensive and relatively difficult to work with, so its use was minimized. It was placed in the plastic-hinge region in the form of a pre-fabricated tube, or shell, approximately 1.5 column diameters long. This shell provided HyFRC at the outside of the column, where the high compressive stresses due to bending were expected, and it left the center of the cross-section open for installing the prestressing strands. Almost all other details were similar to those used by Davis. The prime exception was that, in one of the present columns, the longitudinal deformed bars were made from stainless steel. The purpose was to delay bar fracture; stainless steel typically has a much higher elongation than does ASTM A706 bar steel. The other column used conventional ASTM A706 bars.

The columns were tested under constant axial load and cyclic transverse load. The results showed that the transverse strength was similar to that of columns made with conventional concrete of similar strength, but the use of HyFRC delayed spalling of the concrete, and to a lesser extent, buckling of the bars. Those events occurred at approximately the same drifts as in Haraldsson's columns, which contained no prestressing but used conventional concrete.

## 7.2 Conclusions

The following conclusions were drawn.

1. Adding the HyFRC to the plastic hinge region delayed spalling.
2. Use of HyFRC in the plastic-hinge region slightly delayed the buckling of the longitudinal rebars. Buckling started at approximately 4.0% drift, which was larger than the 3.3% achieved in Davis's prestressed columns, but it was still much less than the 7.1% achieved in Haraldsson's non-prestressed columns made with conventional concrete.
3. Compared with Davis' pre-tensioned columns, these columns (with HyFRC) proved to be more ductile. Both HyFRC columns tested maintained at least 80% of their strength during the entire tests, in which the largest drift ratios exceeded 10%.
4. The use of stainless steel longitudinal reinforcement increased the column strength and delayed fracture of the rebars. Those results were expected because the stainless steel rebar used is both stronger and more ductile than ASTM A706 bar. Comparison of the two columns showed that the stainless steel bar provided almost no improvement in overall ductility, because that was controlled by bar buckling. Thus its use cannot be recommended unless bar buckling can be effectively delayed.

5. Both columns re-centered well. The load-deflection curve indicated that, in a force-controlled test, the residual drift would have been essentially zero up to a peak drift of 5%.
6. The socket connection performed very well. As in former tests, it remained essentially uncracked throughout the entire test.
7. Some strand slip occurred in both columns, but only one strand slipped at drift ratio lower than 5%. It should be noted that the strand diameter was approximately twice as large as the scale demanded, but its size was controlled by commercial availability of small-diameter strands. Thus the bond demand was approximately twice as high as it would be in the prototype.

## 7.3 Recommendations

### 7.3.1 Practice and Design Recommendations

Construction of the columns required two separate operations (casting the shells then the complete column) and was the most time-consuming operation. Changes to shorten the construction time are desirable. One possibility would be to abandon the shell concept and use only one concrete form, in which both types of concrete would be cast at the same time. This procedure would shorten the construction time, but it would require a barrier to prevent the two types of concrete from mixing randomly in the form. It would also lead to a solid HyFRC section in the plastic hinge region, and thus more HyFRC and higher material costs, but these costs would be offset by the lower labor costs associated with the shorter construction time.

### 7.3.2 Recommendations for Future Research

Adding the HyFRC made the columns perform better than before, but more work still needs to be done to improve the columns. The main improvements will be to delay spalling of concrete and buckling of rebar.

It would be ideal to detail the longitudinal rebar so the buckling could be delayed. One idea that could work would be to have the buckling restrained rebar. The rebar would then work similarly as buckling restrained braces having the rebar unbonded inside some steel sleeve filled with grout or something similar.

One way to delay spalling in the columns might be to use a rocking column. By having the column rock the “crack” opening could be controlled. Some ductile material could be located close to the rocking plane for example; rubber pad, HyFRC etc.

Slipping in the columns is a problem that was encountered during the testing of the columns. Having strand chucks hooked onto each strand at top and bottom of the columns and embedded in the concrete would make it less likely that the strands would slip and should be researched further.

For the next test it is highly recommended that the Optotrac tracking system would be used to capture the movement of the column. It is easy to calculate the column rotation and curvature from the Optotrac data. When using the Optotrac system it is important that the motion capturing cameras can not be moved during the testing. It’s also important that all LEDs of the system will be seen during testing. Having the motion capture camera aligned vertically instead of the horizontal alignment that was using during the testing of PreT-BS and PreT-SS will ensure that the LEDs will be seen during the testing.

# 8 References


AASHTO Technical Committee for Seismic Design. (2009). "AASHTO Guide Specifications for LRFD Seismic Bridge Design." American Association of State Highway and Transportation Officials, Washington, D.C.

ACI Committee 318. (2011). "Building Code Requirements for Structural Concrete and Commentary." *ACI 318-11*. American Concrete Institute, Farming Hills, MI.

ASTM International. (2010). "Standard Specification for Stainless Steel Bars and Shapes." *ASTM A276-10*. ASTM International, West Conshohocken, PA.

ASTM International. (2011). "Standard Test Methods for Tension Testing of Metallic Materials." *ASTM E8/E8M – 11*. ASTM International, West Conshohocken, PA.

Bekaert. (2010). "Dramix®, Data Sheet ZP 305." <http://ncg-bg.com/assets/files/products/01_materials_for_industrial_floors/1_fibri_za_beton/Dramix%20ZP%20305_en.pdf> Retrieved, 15. July 2012. Bekeart, Kortrijk, Belgium.

Berry, M.P. and Eberhard, M.O. (2005). "Practical Performance Model for Bar Buckling." *Journal of Structural Engineering, ASCE*, Vol. 131, No 7, July 2005, pp. 1060-1070.

Berry, M.P., Parrish, M. and Eberhard, M.O. (2004). "PEER Structural Performance Database: User's Manual (Version 1.0)". Pacific Earthquake Engineering Research Center Report 2004, University of California, Berkeley, CA.

Brown, W. (2008). "Bar Buckling in Reinforced Concrete Bridge Columns." Master's Thesis, University of Washington, Seattle, WA.

Building Seismic Safety Council for the FEMA. (2004). "NEHRP Recommended Provisions for Seismic Regulations for New Buildings and Other Structures (FEMA 450-1 / 2003 Edition)." National Institute of Building Sciences, Washington, D.C.

Carpenter Technology Company. (2010). "Technical Datasheet." *Carpenter Technology Company.* <http://www.cartech.com> Retrieved May 5, 2012. Carpenter Technology Company, Wyomissing, PA.

Carpenter Technology Company. (2002). "Stainless Steel Rebar for Concrete Reinforcement where Corrosion Resistance, High Strength Are Needed." *Carpenter Technology Company - News*. Carpenter Technology Company, Wyomissing, PA.

Chopra, A.K. (2007). "Dynamics of Structures – Theory and Applications of Earthquake Engineering, Third Edition". Pearson Prentice Hall, Upper Saddle River, NJ.

Cohagen, L.S., Pang, J.B.K., Eberhard, M.O. and Stanton, J.F. (2008). "A Precast Concrete Bridge Bent Designed to Re-center After an Earthquake." *Washington State Department of Transportations*. Report No. WA-RD 684.3, Washington State Department of Transportation, Olympia, WA.

Cousins, T.E., Johnston, D.W. and Zia, P. (1990). "Transfer and Development Length of Epoxy Coated and Uncoated Prestressing Strand". *PCI Journal*. Precast/Prestressed Concrete Institute, July-August, pp. 34-49.

Davis, P. M., Janes, Todd M., Eberhard, M.O., Stanton, J.F. and Haraldsson, O.S. (2012), "Unbonded Pre-tensioned Columns for Accelerated Bridge Construction in Seismic Regions," submitted to Journal of Bridge Engineering, ASCE.

Davis, P.M., Janes, T.M., Eberhard, M.O, and Stanton, J.F. (2011). *Unbonded Pre-Tensioned Columns for Bridges in Seismic Regions*. Pacific Earthquake Engineering Research Center Report 2011.

Elwood, K. and Eberhard, M. (2009). "Effective Stiffness of Reinforced Concrete Columns", *ACI Structural Journal*", Vol. 106, No. 4, July-August 200p, pp 476-484.

Franchi, A., Crespi, P., Bennani, A. and Farinet, M. (2006). "Stainless Steel Rebar for Seismic Applications." *Advances in Engineering Structures, Mechanics & Construnction*, pp. 255-264. Springer, Netherlands.

Haraldsson, O. and Berry, M. (2011). "Accelerating Bridge Construction to Reduce Congestion." Transportation Northwest Final Report, TNW2011-08. University of Washington, Seattle, WA.

Haraldsson, O., Janes, T.M., Eberhard, M.O. and Stanton, J.F. (2011). "Laboratory Tests of Column-to-Footing Socket Connections". *Highways for LIFE Technology Partnership Program*. Federal Highway Administration, Washington, DC.

Hieber, D., Wacker, J., Eberhard, M.O. and Stanton, J.F. (2005a). "Precast Concrete Pier Systems for Rapid Construction of Bridges in Seismic Regions." *Washingon State Department of Transportation Report No. WA-RD-511.1*. Washington State Department of Transportation, Washington, 2005.

Jimenez, J.G. (2012). "Bond Capacity of Steel Epoxy-Coated and Uncoated Pre-Stressing Strands." *PEER Intership Final Report*. PEER, Berkeley, CA.

Khaleghi, B., Schultz, E., Seguirant, S., Marsh, L., Haraldsson, O., Eberhard, M.O. and Stanton, J.F. (2012). "Accelerated Bridge Construction in Washington State: From Research to Practice". *PCI Journal*. Precast/Prestressed Concrete Institute, Fall, pp. 34-49.

Kuraray. (2012). Product Data Sheet. <http://www.kuraray-am.com/pvaf/fibers.php> Retrieved 16. July 2012. Kuraray, Tokyo, Japan.

MMFX Technology Corporation. (2013). <http://www.mmfx.com> Retrieved 17. January 2013. MMFX Technology Corporation, Irvine, CA.

Ostertag, C.P., Jen, G. and Trono, W.(2013). "Self Compacting Hybrid Fiber Reinforced Concrete Composites for Bridge Columns". Cement and Concrete Composites. Submitted.

Pang, J.B.K., Eberhard, M.O. and Stanton, J.F. (2010). Large-Bar Connection for Precast Bride Bents in Seismic Regions. *Journal of Bridge Engineering, ASCE*, 15(3), 231-239.

Priestley M.J.N., Verma, R. and Xiao, Y., (1994), "Seismic Shear Strength of Reinforced Concrete Columns", *Journal of Structural Engineering*, Vol. 120, No. 8, August 1994.

Schnell, R.E., and Bergmann, M.P. (2007). *Improving Tomorrow's Infrastructure: Extending the Life of Concrete Structures with Solid Stainless Steel Reinforcing Bar*. Presented at the 2007 New York City Bridge Engineering Conference, August 28, 2007.

Stanton, J.F., Stone, W.C. and Cheok, G.S. (1997). "Hybrid Reinforced Precast Frame for Seismic Regions." *PCI Journal*, 42(2), 20-32. Precast/Prestressed Concrete Institute, Chicago, Il.

Trate, R. (2004). "Choosing Stainless Steel Rebar." *Wire Forming Technology International*. Winter, 2004, pp. 18-19. Wire Forming Technology, Akron, OH.

Zhang, G., Wang, C. and Zhang, Z. (2011). "Strength Degradation and Energy Dissipation of Stainless steel Reinforced Concrete Columns." *Applied Mechanics and Materials*. Vols. 90-93, pp. 1614-1617. Trans Tech Publications, Switzerland.

Zhou, Y., Ou Y.C., Lee, G.C. and O'Connor, J.S. (2008). "A Pilot Experimental Study on the Low Cycle Fatigue Behavior of Stainless Steel Rebars for Earthquake Engineering Applications." *Carpenter Technology Company.* Carpenter Technology Company, Wyomissing, PA.

# Appendix A: Materials

In this appendix there will be provided extra information about the structural materials used in the research. The main structural materials in the research were; regular concrete, HyFRC, regular reinforcement steel and stainless steel reinforcement.

## Concrete strength

Three casts of concrete were done in this research and strength history is provided for every cast of concrete done. Both data points and strength history graph is provided below for every cast of concrete.

### Column concrete

**Table A - 1: Column concrete compressive strength history. Day 10: stressing day 1, Day 14: stressing day 2, Day 70: testing day 1, Day 89: testing day 2.**

| Day | Strength [psi] |
|---|---|
| 3 | 4415.0 |
| 7 | 5289.4 |
| 10 | 5406.3 |
| 14 | 5902.0 |
| 28 | 6417.7 |
| 70 | 6741.1 |
| 89 | 6659.2 |

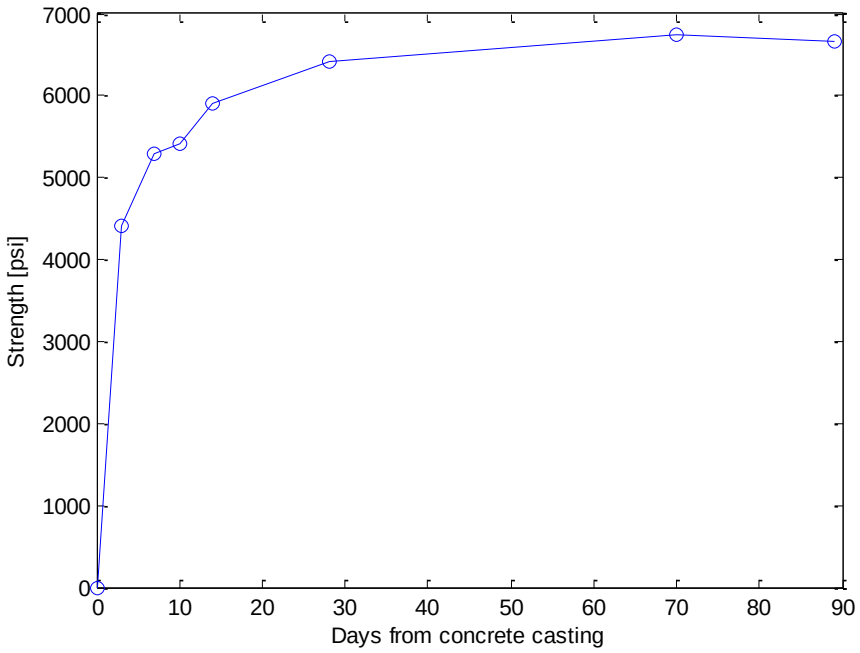


**Figure A - 1: Column concrete compressive strength history.**

## PreT-BS footing concrete

**Table A - 2: PreT-BS footing concrete compressive strength history. Day 72: testing day 2.**

| Day | Strength [psi] |
|---|---|
| 3 | 4385,8 |
| 7 | 4911,5 |
| 14 | 5604,2 |
| 28 | 5375.0 |
| 72 | 5645.2 |

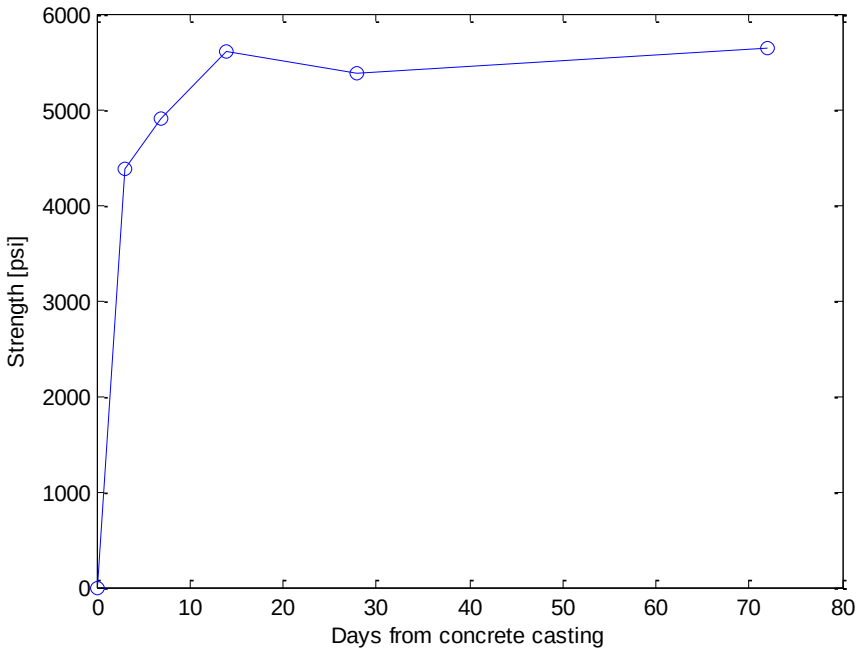


**Figure A - 2: PreT-BS footing compressive strength history.**

## PreT-SS footing concrete

**Table A - 3: PreT-SS footing concrete compressive strength history. Day 51: testing day 1.**

| Day | Strength [psi] |
|---|---|
| 3 | 5409.1 |
| 7 | 6590.8 |
| 14 | 7593.1 |
| 28 | 8150.9 |
| 51 | 8759.9 |

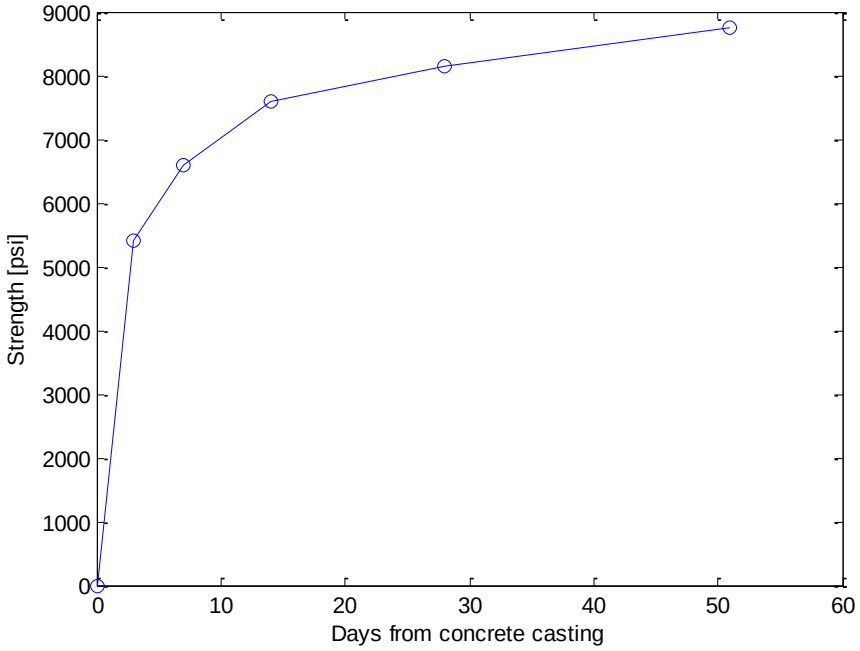


**Figure A - 3: PreT-SS footing compressive strength history.**

**E-mod history**

E-mod data was collected for the column concrete over time. E-mod data was also collected for one of the footing since another student at UW used concrete from the same concrete truck but the E-mod data of the footing is of no interest here. The data for the E-mods was obtained at days 3, 7 (de-stressing day #1 of prestressing strands), 10 (de-stressing day #2), day 14, day 68 (first actual testing day) and day 87 (second actual testing day). The collected E-mod data for the column concrete is displayed here below.

**Table A - 4: E-mod data for the column concrete.**

| Age [days] | E-mod [ksi] |
|---|---|
| 3 | 2619 |
| 7 | 2911 |
| 10 | 2894 |
| 14 | 3103 |
| 68 | 3556 |
| 87 | 3310 |

The E-mod data for the column concrete was also plotted over the history to the data can be view graphically.

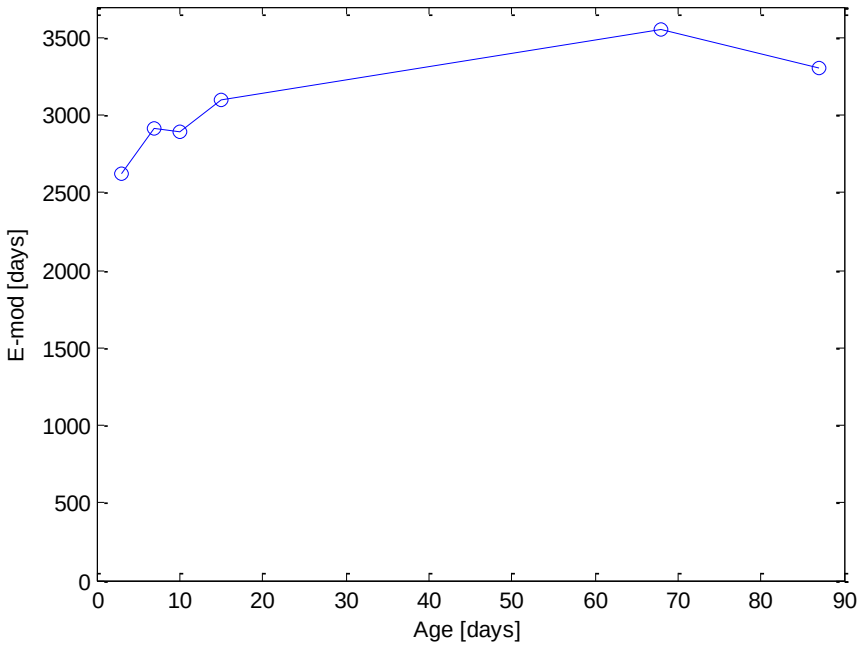


**Figure A - 4: E-mod history for the column concrete.**

## HyFRC batch strengths

As mentioned in section 2.2.3 the HyFRC five batches of the concrete were mixed and the strengths of the batches were different. Only 3 testing cylinders were cast for batches 1-4, but batch 5 had a lot of testing cylinders. Because the strength difference was encountered the strengths for batch 5 were used to estimate the strength of the other batches.

**Batch #1**

**Table A - 5: Measured and guessed compressive strength history for HyFRC batch #1. Day 52 stressing day 1; day 116 testing day 1 (for PreT-SS) and day 134 testing day 2 (for PreT-BS).**

| Day | Measured strength [psi] | Estimated strength [psi] |
|---|---|---|
| 3 | 2533.6 | 2684.9 |
| 7 | | 3515.9 |
| 28 | | 4787.7 |
| 52 | | 5306.9 |
| 116 | | 6107.4 |
| 134 | 6576.4 | 6225.5 |

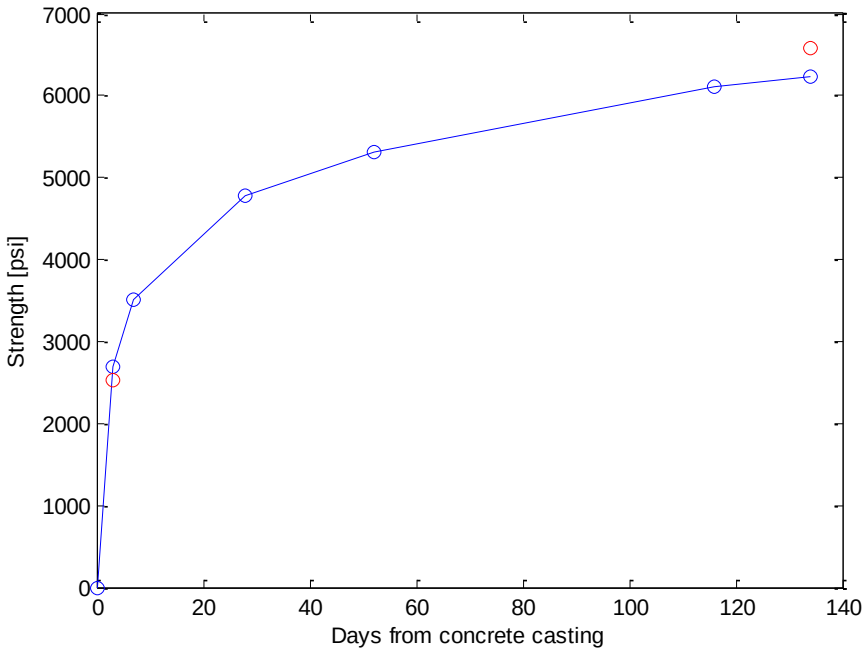


**Figure A - 5: HyFRC batch #1 compressive history. Blue: guessed history. Red: measured points.**

**Batch #2**

**Table A - 6: Measured and guessed compressive strength history for HyFRC batch #2. Day 52 stressing day 1; day 116 testing day 1 (for PreT-SS) and day 134 testing day 2 (for PreT-BS).**

| Day | Measured strength [psi] | Estimated strength [psi] |
|---|---|---|
| 3 | 2777.5 | 2812.8 |
| 7 | 3729.6 | 3683.3 |
| 28 | | 5015.7 |
| 52 | | 5559.7 |
| 116 | | 6398.2 |
| 134 | 6980.8 | 6522.0 |

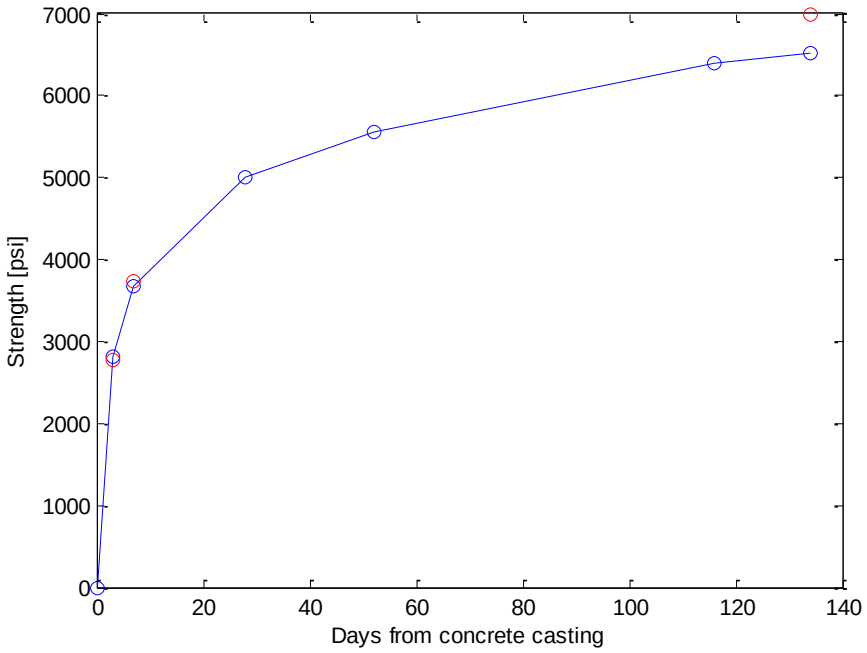


**Figure A - 6: HyFRC batch #2 compressive history. Blue: guessed history. Red: measured points.**

**Batch #3**

**Table A - 7: Measured and guessed compressive strength history for HyFRC batch #3. Day 52 stressing day 1; day 116 testing day 1 (for PreT-SS) and day 134 testing day 2 (for PreT-BS).**

| Day | Measured strength [psi] | Estimated strength [psi] |
|---|---|---|
| 3 | | 2989.5 |
| 7 | | 3914.8 |
| 28 | | 5330.8 |
| 52 | | 5909.0 |
| 116 | 6772.3 | 6800.3 |
| 134 | 6960.3 | 6931.8 |

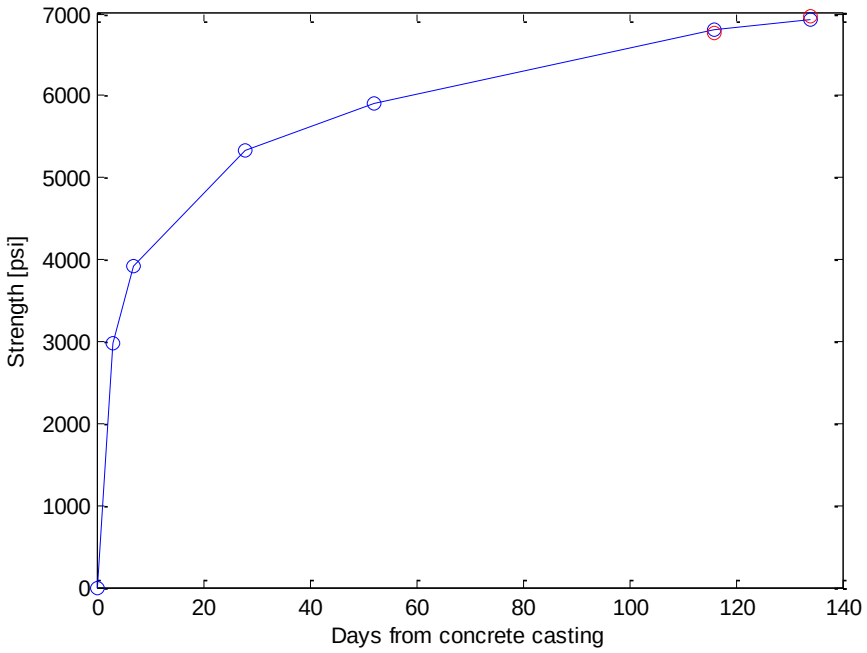


**Figure A - 7: HyFRC batch #3 compressive history. Blue: guessed history. Red: measured points.**

**Batch #4**

**Table A - 8: Measured and guessed compressive strength history for HyFRC batch #4. Day 52 stressing day 1; day 116 testing day 1 (for PreT-SS) and day 134 testing day 2 (for PreT-BS).**

| Day | Measured strength [psi] | Estimated strength [psi] |
|---|---|---|
| 3 | | 2989.5 |
| 7 | | 3914.8 |
| 28 | | 5330.8 |
| 52 | | 5909.0 |
| 116 | 6772.3 | 6800.3 |
| 134 | 6960.3 | 6931.8 |

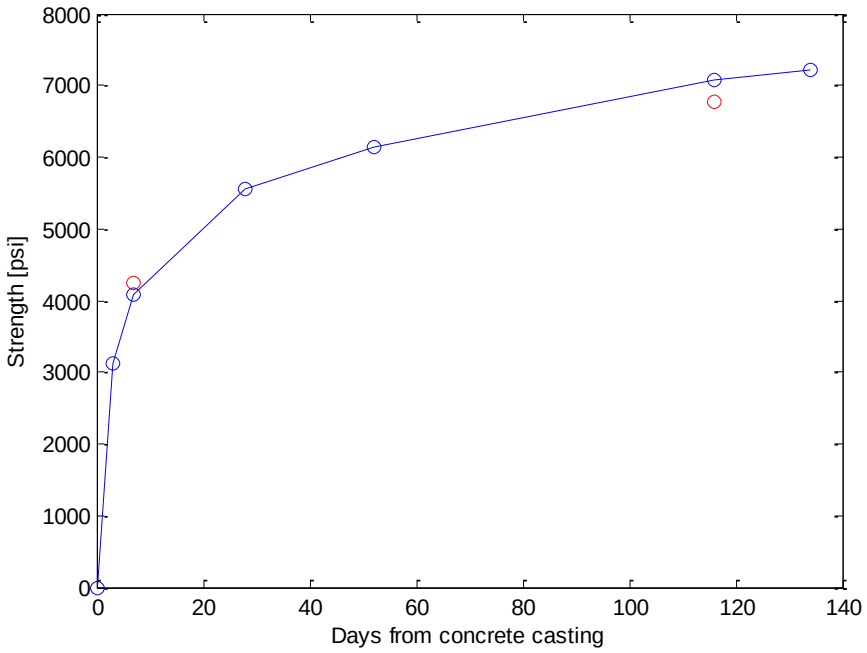


**Figure A - 8: HyFRC batch #4 compressive history. Blue: guessed history. Red: measured points.**

**Batch #5**

Batch #5 was the only batch of the HyFRC that was measured every day when the HyFRC was tested. Since batch #5 was tested all testing days the batch was used to estimate the compressive history of the other batches (#1-4).

**Table A - 9: Measured compressive strength for batch #5 of the HyFRC.**

| Day | Measured strength [psi] |
|---|---|
| 3 | 3617.8 |
| 7 | 4737.5 |
| 28 | 6451.2 |
| 52 | 7150.9 |
| 116 | 8229.5 |
| 134 | 8388.7 |

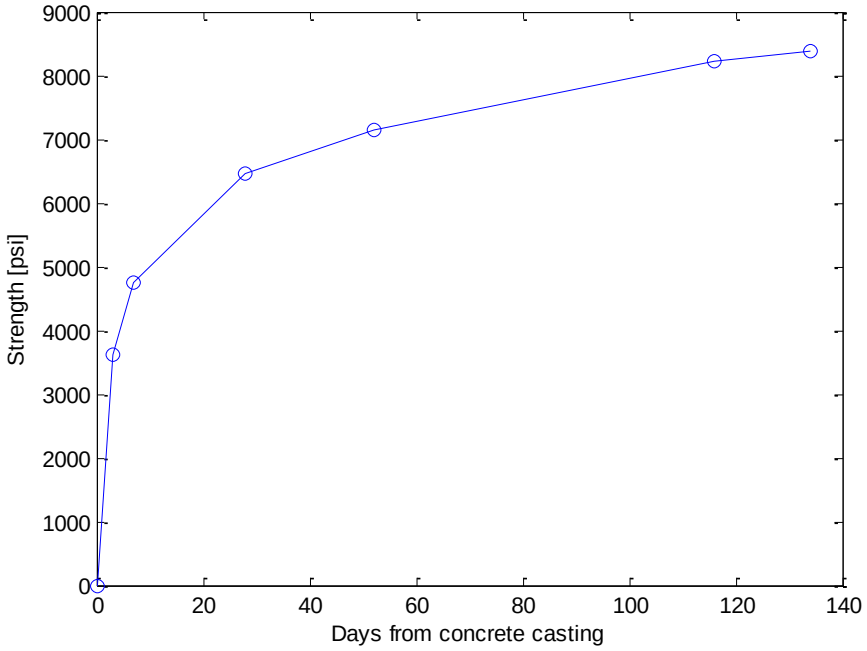


**Figure A - 9: Measured compressive strength history for batch #5 of the HyFRC.**

**E-mod history**

The E-mods for the batches were measured over time. The data for the E-mods was obtained at days 21, 28, de-stressing day 1 and during both tests (when the corresponding batch included in the tests). Since batch# 5 was used to estimate the strength of the other batches it was tested for E-mod every day when cylinders were testes, except day 7 and 14. The results of the E-mod data are displayed here below.

**Table A - 10: History of E-mod data over time for the HyFRC.**

| Age [days] | E-mod [ksi] | | | | |
|---|---|---|---|---|---|
| | Batch #1 | Batch #2 | Batch #3 | Batch #4 | Batch #5 |
| 3 | 2931 | - | - | - | 1510 |
| 21 | 3205 | 4472 | 3553 | 3767 | 4222 |
| 28 | 4501 | 4160 | 3882 | 4182 | 4214 |
| 52 | 4854 | 4594 | 4366 | 4251 | 4325 |
| 115 | - | - | 4374 | 4303 | 4830 |
| 134 | 4718 | 4723 | - | - | 5801 |

This table was then plotted so the results from the E-mod data could be seen graphically.

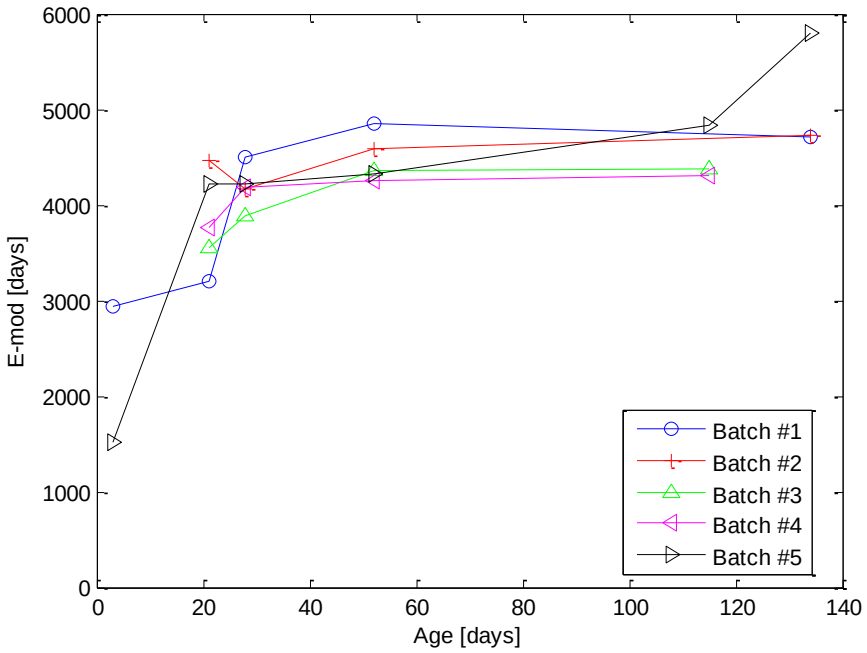


**Figure A - 10: E-mod history of all HyFRC batches.**

## Black steel strength

Below are provided the stress-strain relations plot for all the black steel reinforcement used for both specimens.

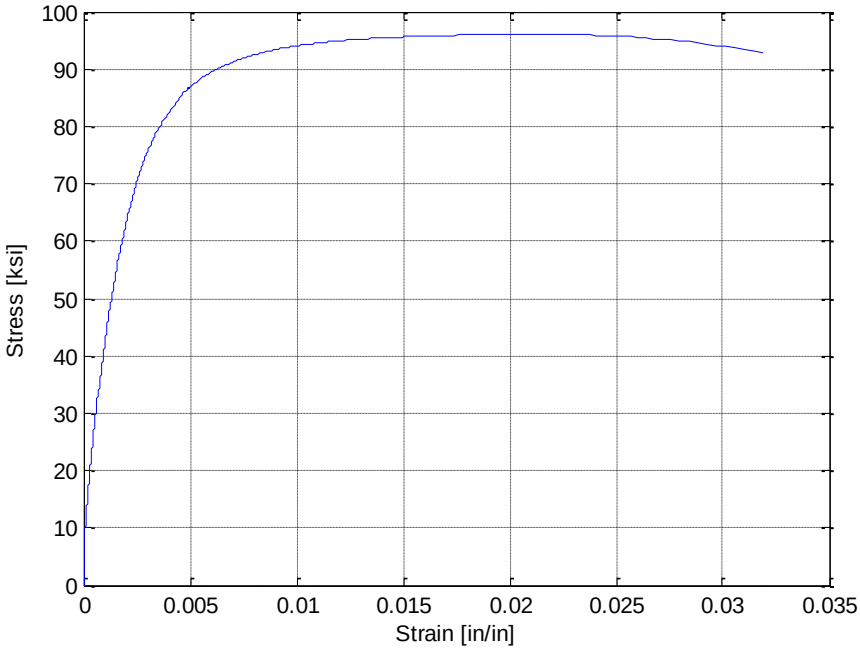


**Figure A - 11: Stress-strain relations for 3 gauge spiral reinforcement.**

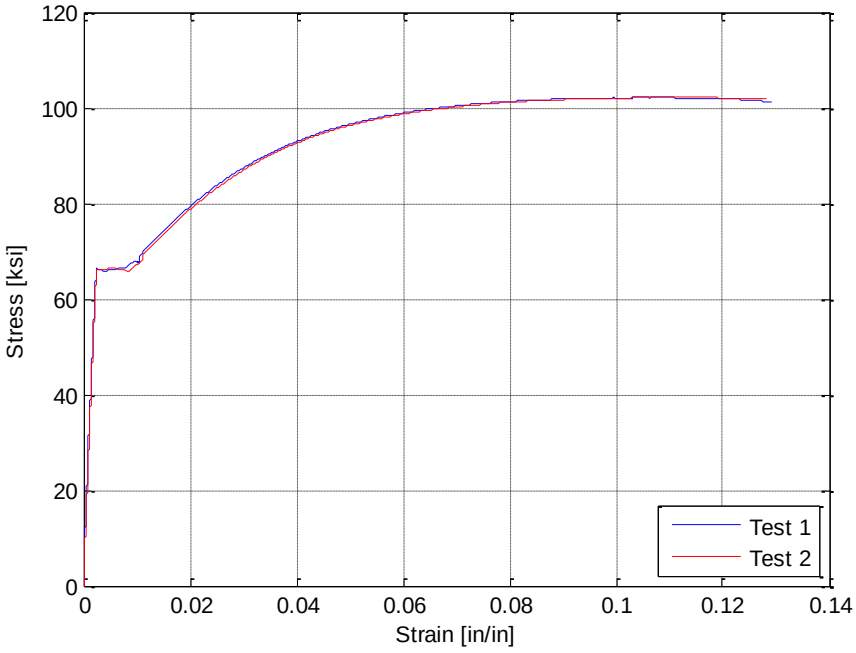


**Figure A - 12: Stress-strain relations for #3 reinforcement.**

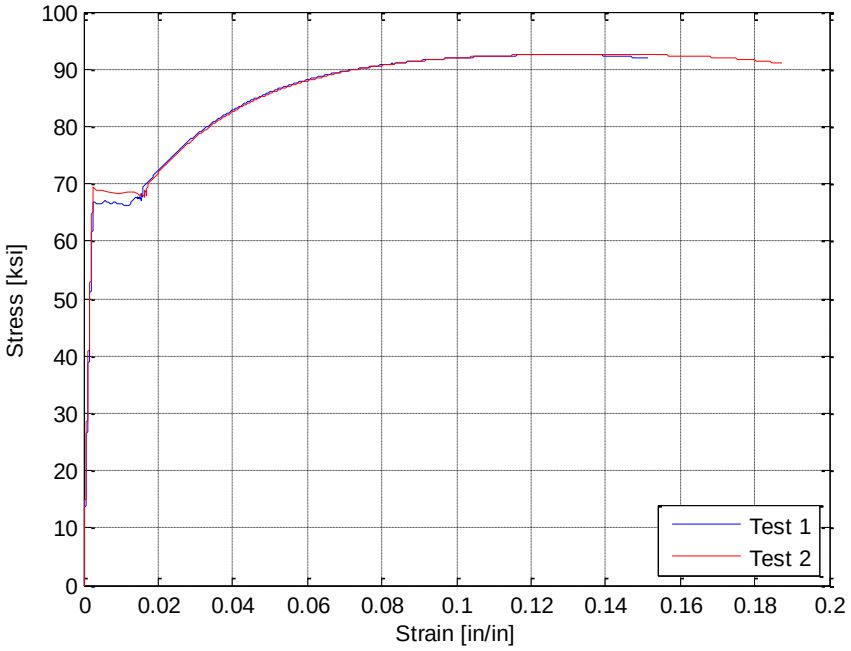


**Figure A - 13: Stress-strain relations for #4 reinforcement.**

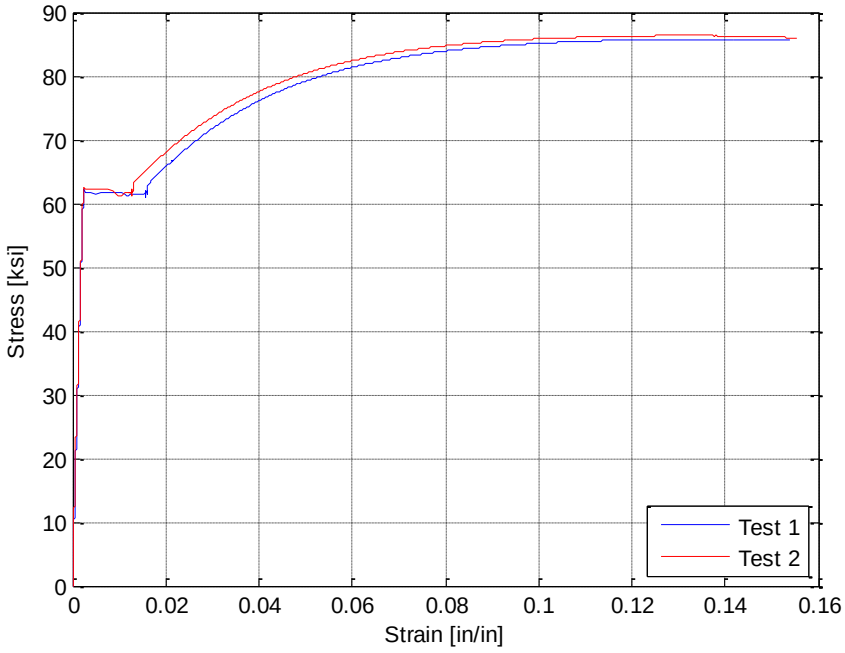


**Figure A - 14: Stress-strain relations for #5 reinforcement.**

**Stainless steel strength**

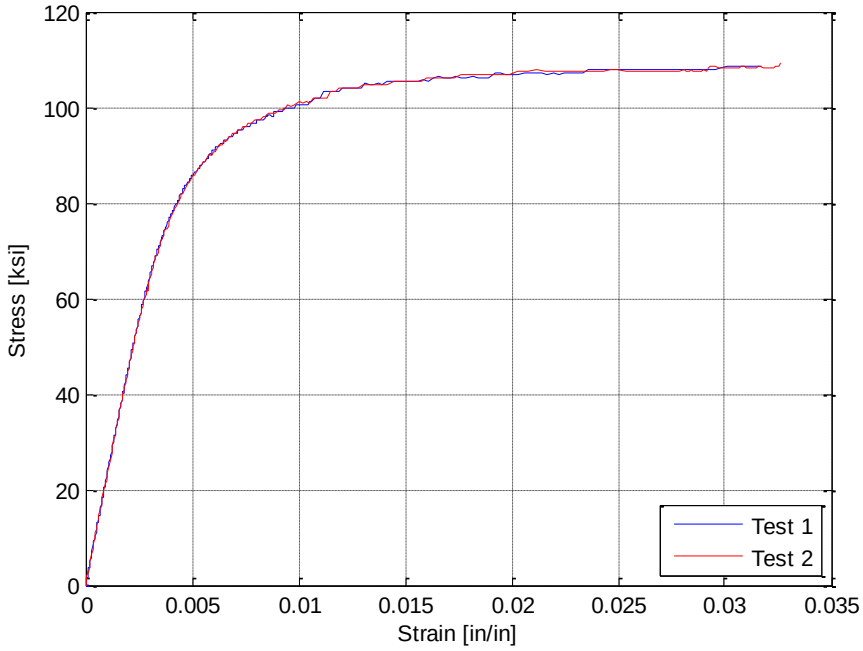


**Figure A - 15: Stress-strain relations for #4 stainless steel reinforcement of type 2205.**

The reason why the measurements for the stainless steel are only up to about 0.03 strains was because the strain was measured with strain gauges. The black steel rebar could be plotted for much higher strains because a potentiometer was used to measure the strains and could easily measure for much higher strains.

# Appendix B: Specimen Drawings

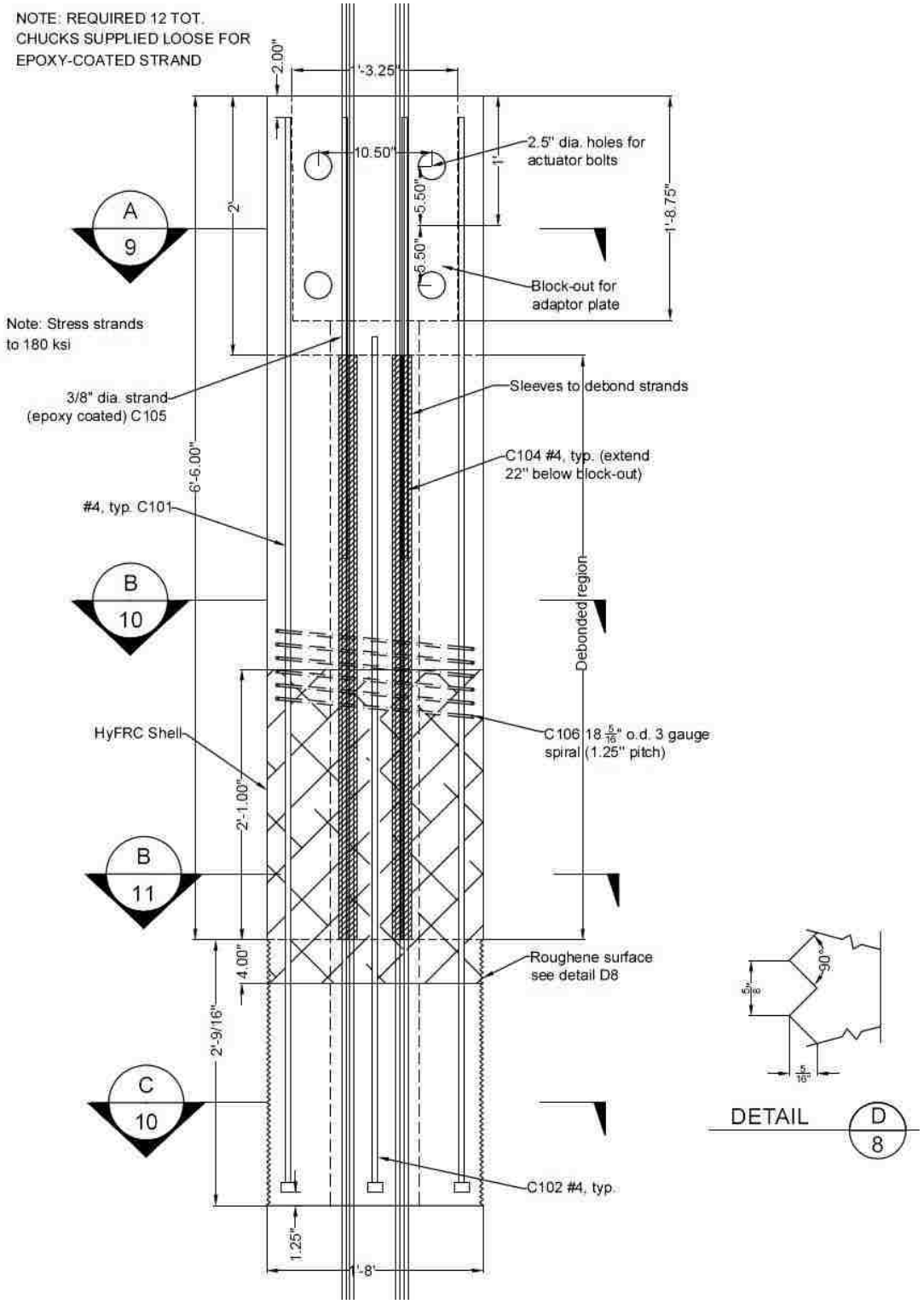


**Figure B - 1: Column elevation**

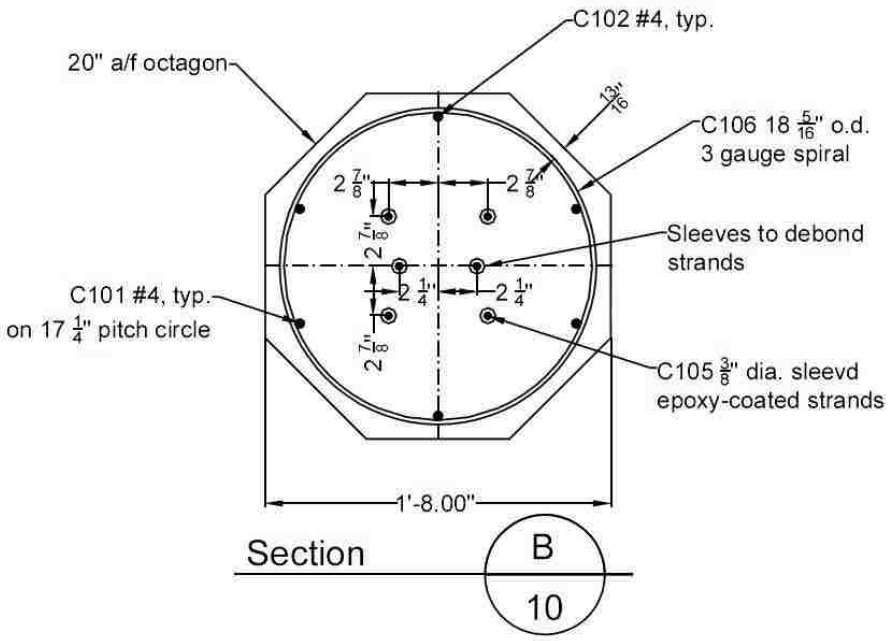


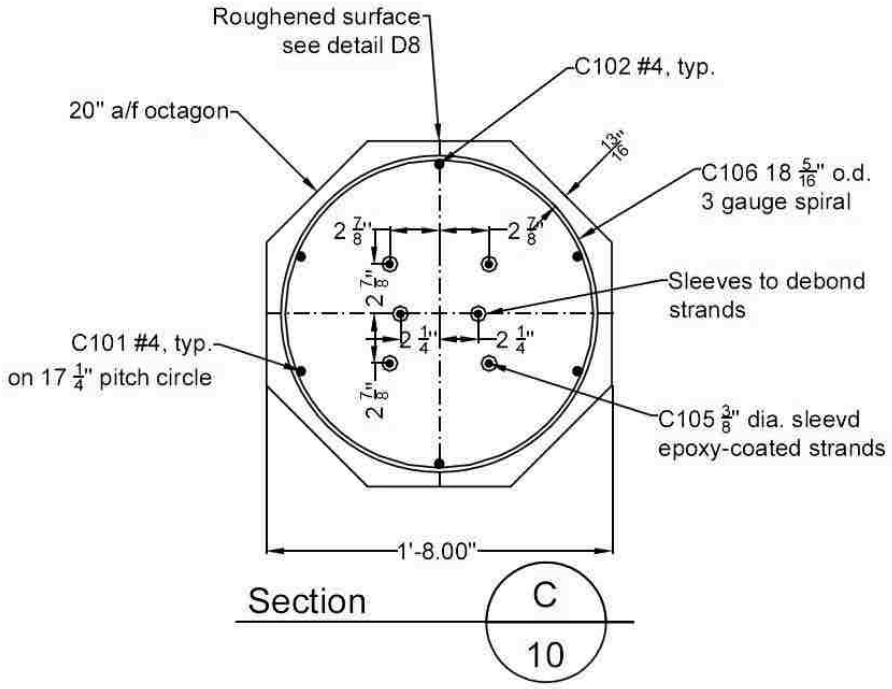


**Figure B - 2: Column section B-10 and C-10**

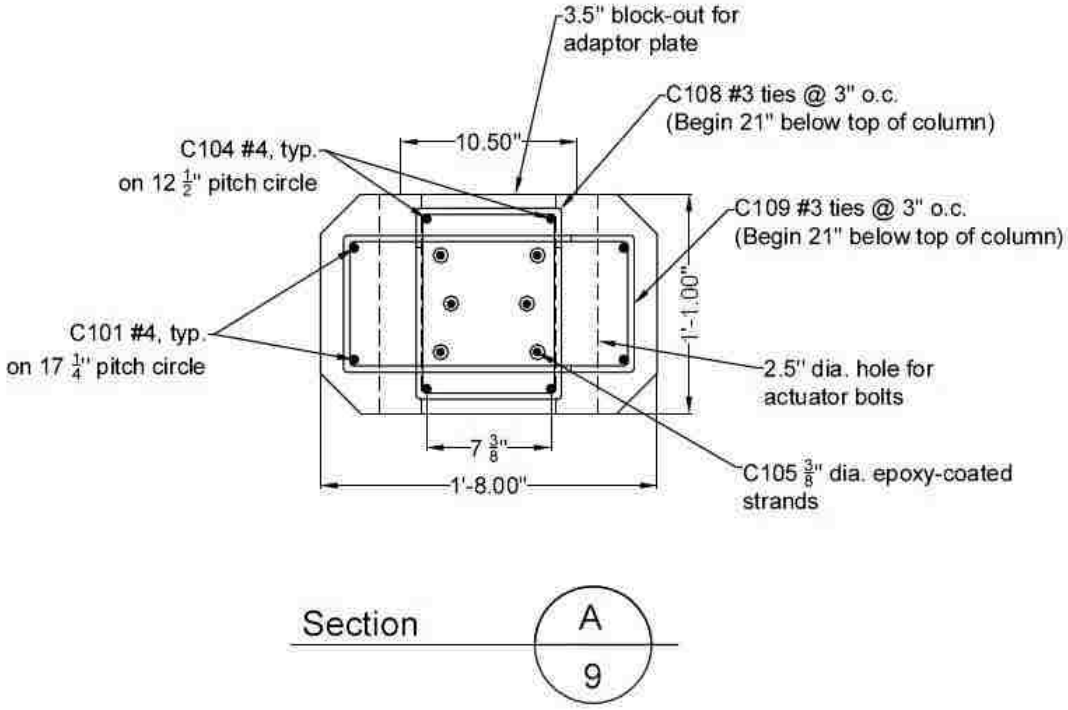


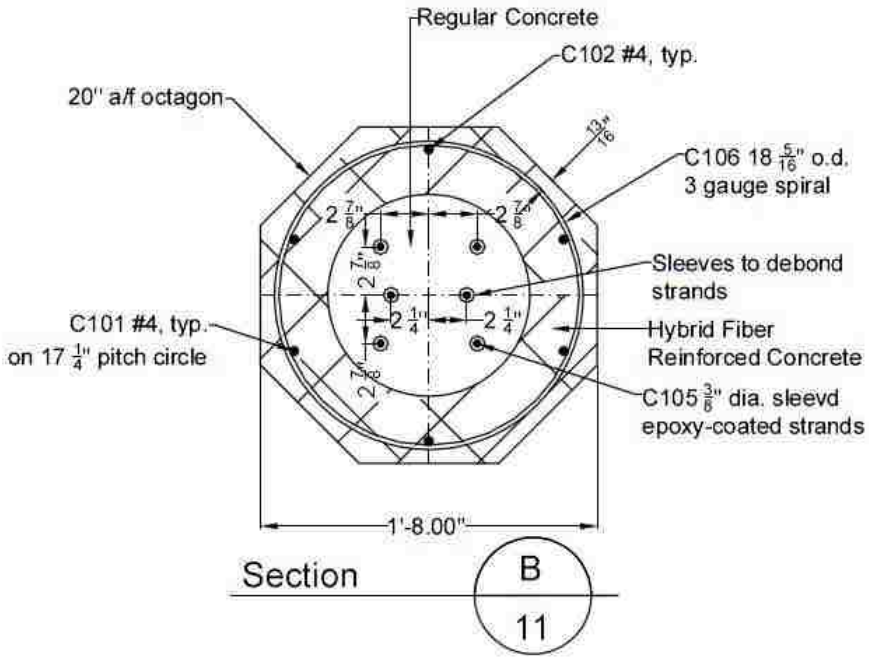


**Figure B - 3: Column section A-9 and B-11**

**Steel Quantity Schedule - regular black steel, Gr60**

| Bar Mark | Bar Type | Specimen Quantity | Total Quantity | Bar Size | Dimensions [in.] | | | ASTM | Notes |
|---|---|---|---|---|---|---|---|---|---|
| | | | | | Dimension A | Dimension B | Dimension C | | |
| C101 | 1 | 4 | 4 | #4 | 99,5 | - | - | 706 | Headed long. Bar * |
| C102 | 1 | 2 | 2 | #4 | 79,0 | - | - | 706 | Headed long. Bar * |
| C104 | 1 | 4 | 8 | #4 | 40,75 | - | - | 706 | Block-out long. Bar |
| C108 | 2 | 7 | 14 | #3 | 8 5/8 | 9,75 | 9 | 706 | Block-out ties |
| C109 | 2 | 7 | 14 | #3 | 8,25 | 17 3/8 | 13,5 | 706 | Block-out ties |
| N/A | 1 | 2 | 2 | #4 | 8-ft | | | | Bars for testing |




Notes:
1. All dimensions are out-to-out unless otherwise noted.
2. * On bars C101 and C102 add threads to put on Lenton Terminator heads on just one end of each bar.

**Figure B - 4: Steel schedule for both columns.**

Note that bars C101 and C102 were the longitudinal rebar and therefore changed between columns, other bars were the same. The spiral not included in schedule, see drawings for details.

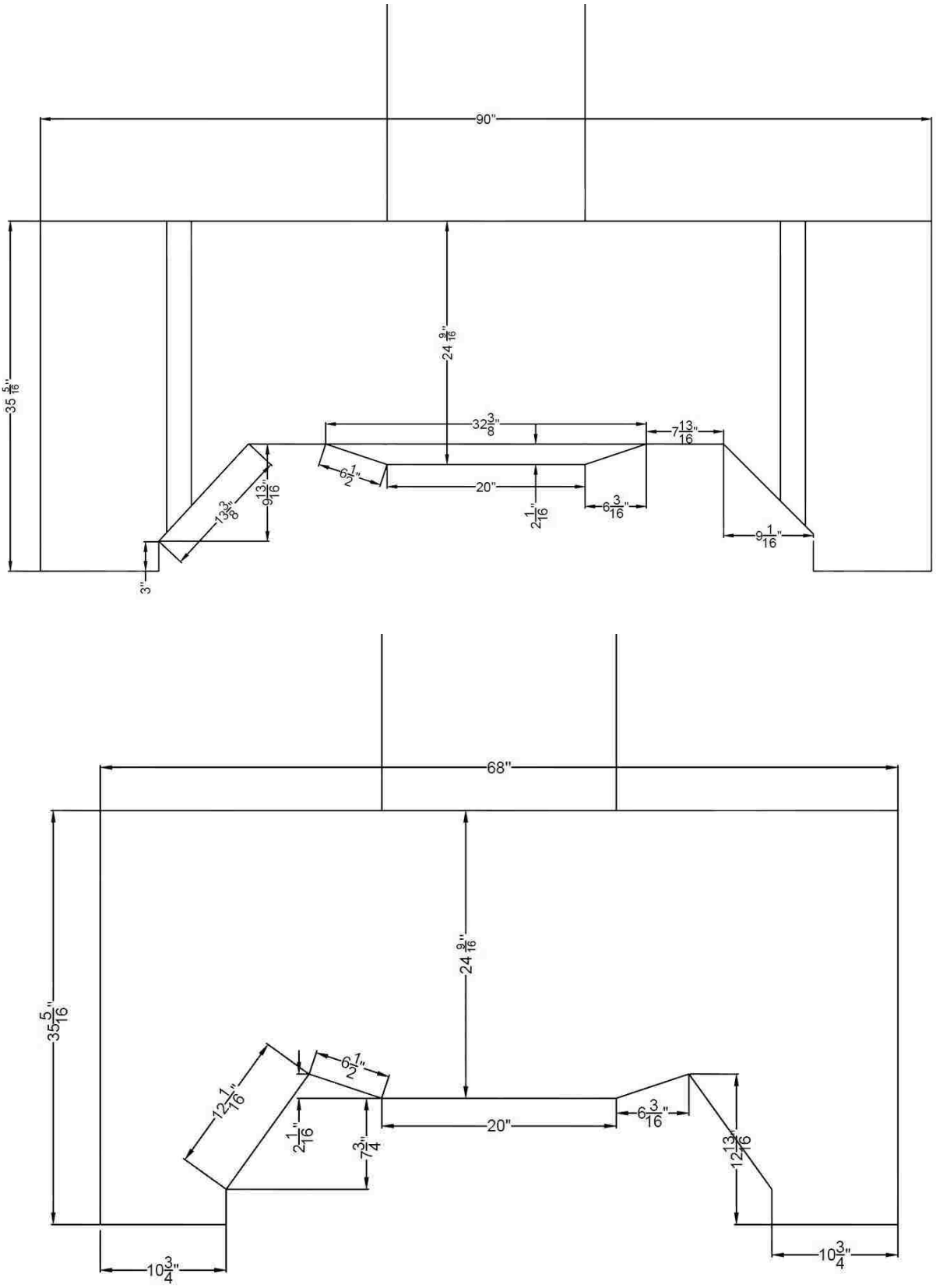


**Figure B - 5: Footing dimensions, profile and transverse sections respectively**

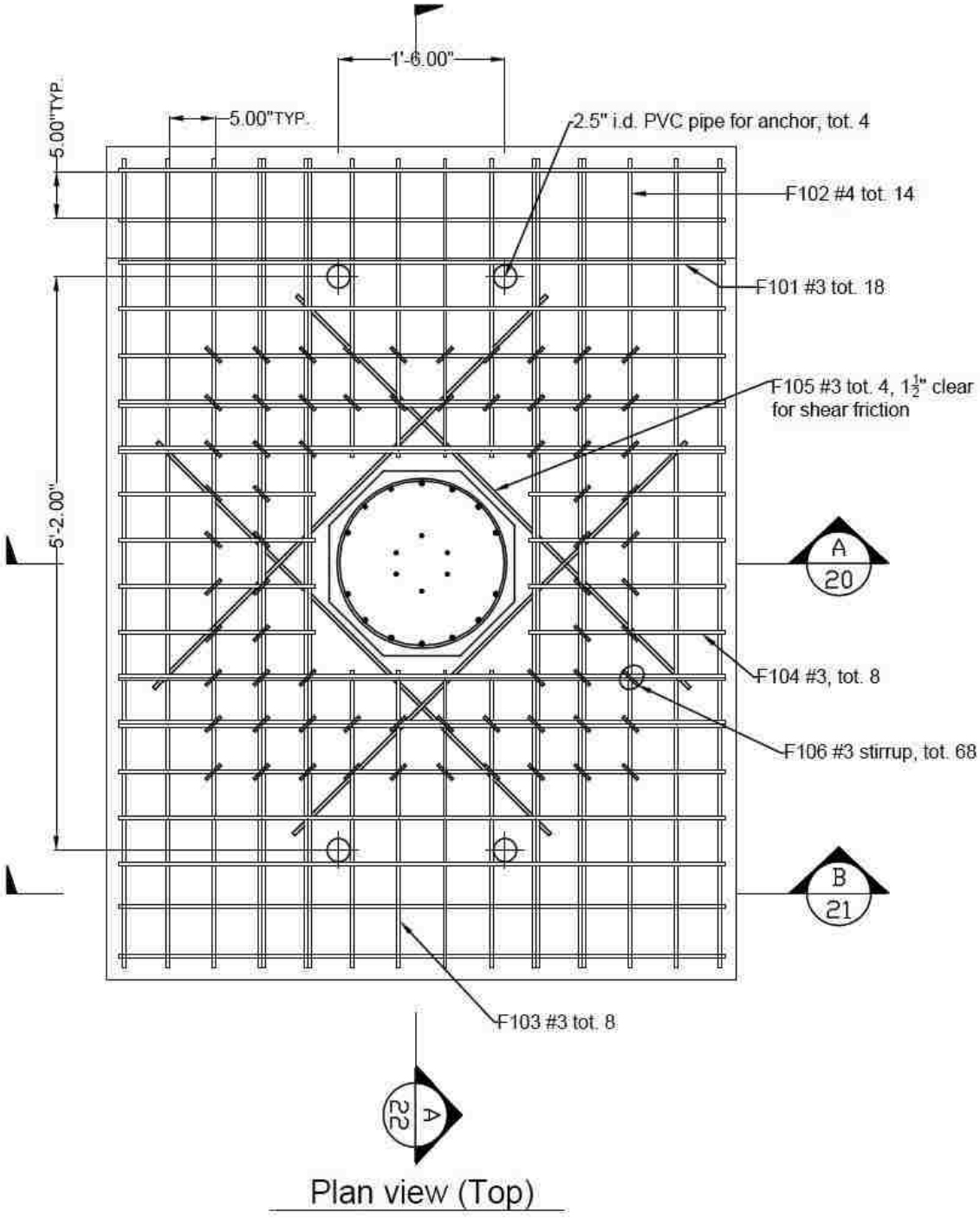


**Figure B - 6: Top footing steel (and stirrups)**

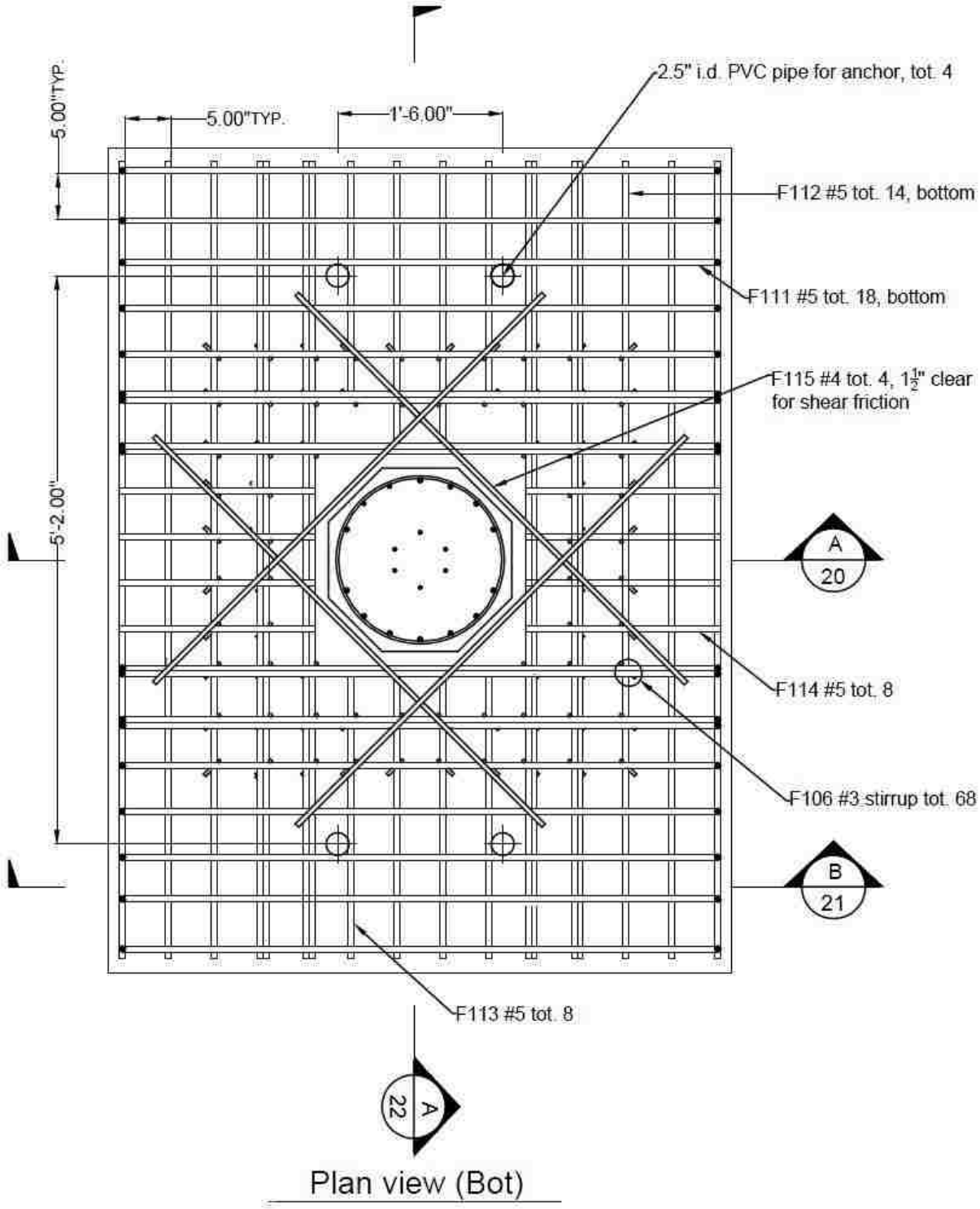


**Figure B - 7: Bottom footing steel (and stirrups)**

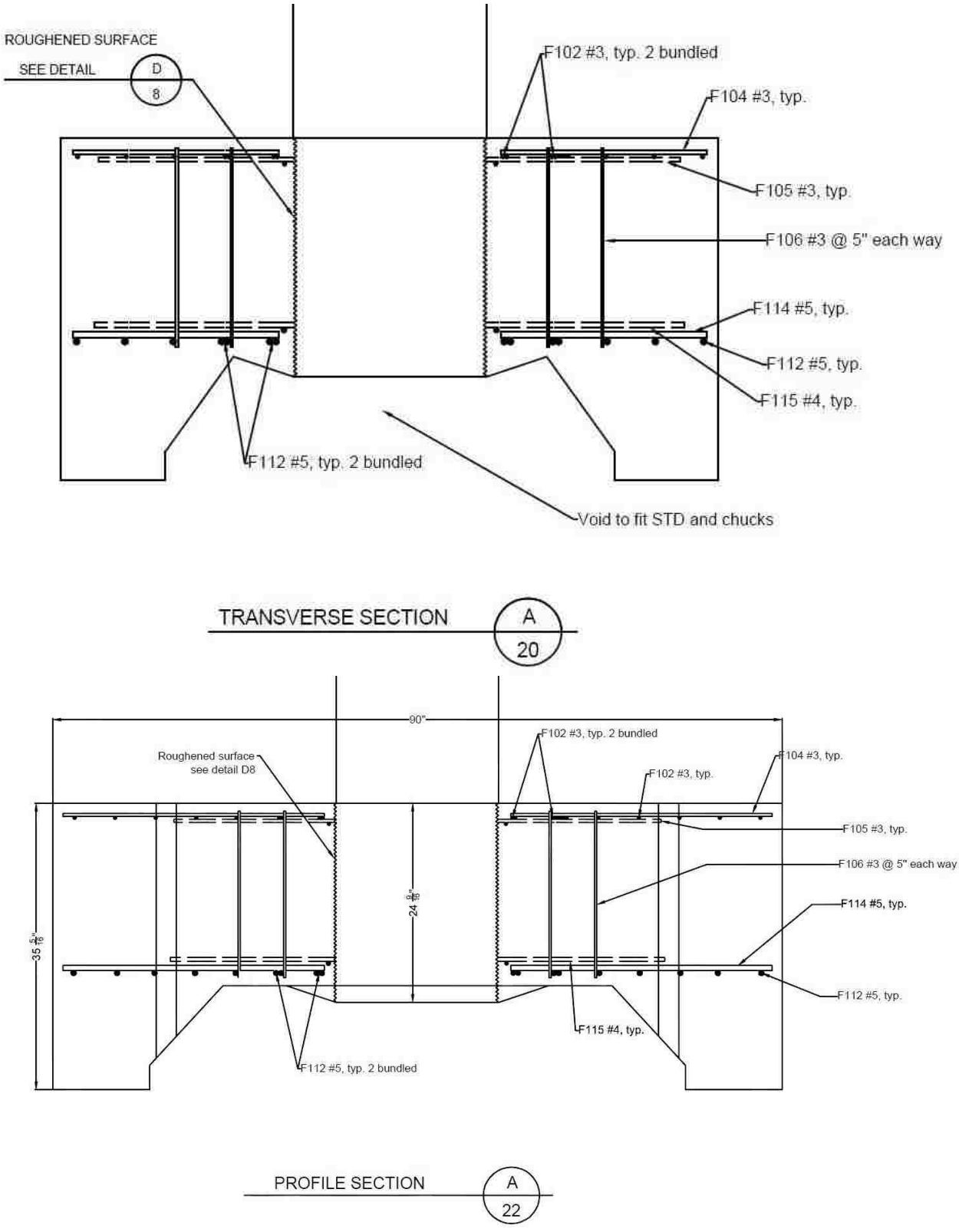


**Figure B - 8: Footing steel, sections**

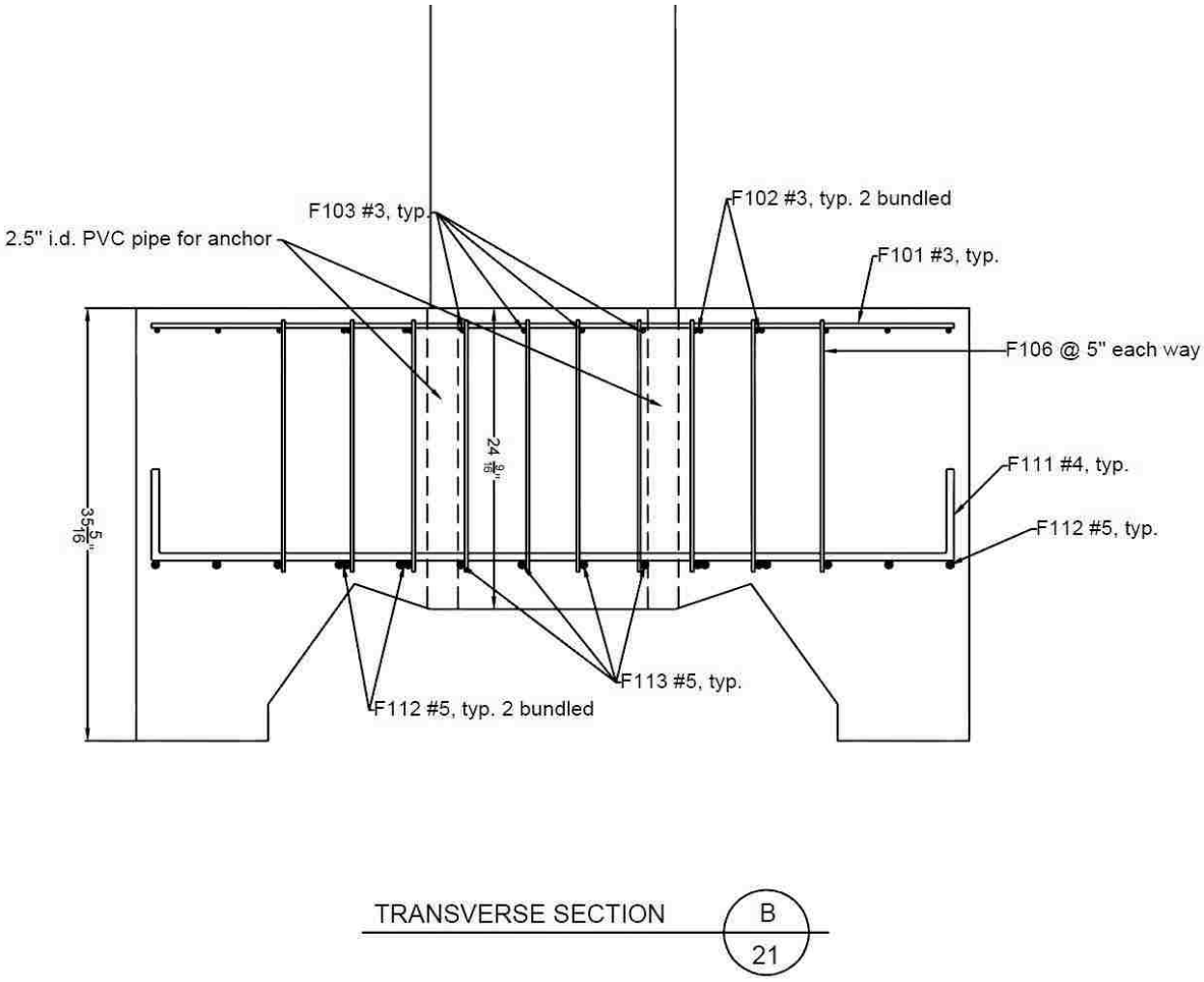


**Figure B - 9: Footing steel, section**

## Steel Quantity Schedule - Footing - regular black steel, Gr60

| | | | | | Dimensions [in.] | | | | |
|---|---|---|---|---|---|---|---|---|---|
| Bar Mark | Bar Type | Specimen Quantity | Total Quantity | Bar Size | Dimension A | Dimension B | Dimension C | ASTM | Notes |
| F101 | 1 | 20 | 40 | #3 | 65,5 | | | 706 | top mat |
| F111 | 2 | 20 | 40 | #5 | 65,5 | 9,375 | | 706 | bottom mat |
| F102 | 1 | 14 | 28 | #3 | 87,5 | | | 706 | top mat |
| F112 | 1 | 14 | 28 | #5 | 87,5 | | | 706 | bottom mat |
| F103 | 1 | 8 | 16 | #3 | 32,25 | | | 706 | top mat |
| F113 | 1 | 8 | 16 | #5 | 32,25 | | | 706 | bottom mat |
| F104 | 1 | 8 | 16 | #3 | 21,25 | | | 706 | top mat |
| F114 | 1 | 8 | 16 | #5 | 21,25 | | | 706 | bottom mat |
| F105 | 1 | 4 | 8 | #3 | 61 | | | 706 | top SF steel |
| F115 | 1 | 4 | 8 | #4 | 60 | | | 706 | bot. SF steel |
| F106 | 3 | 70 | 140 | #3 | 4,0 | 20,5 | 4 | 82 | transv. Steel |
| F108 | 4 | 4 | 8 | #6 | 6 | 26 | 12 | 706 | lifting loops |
| F109 | 5 | 8 | 16 | #4 | 18 | 9 | 8 | 706 | standees |

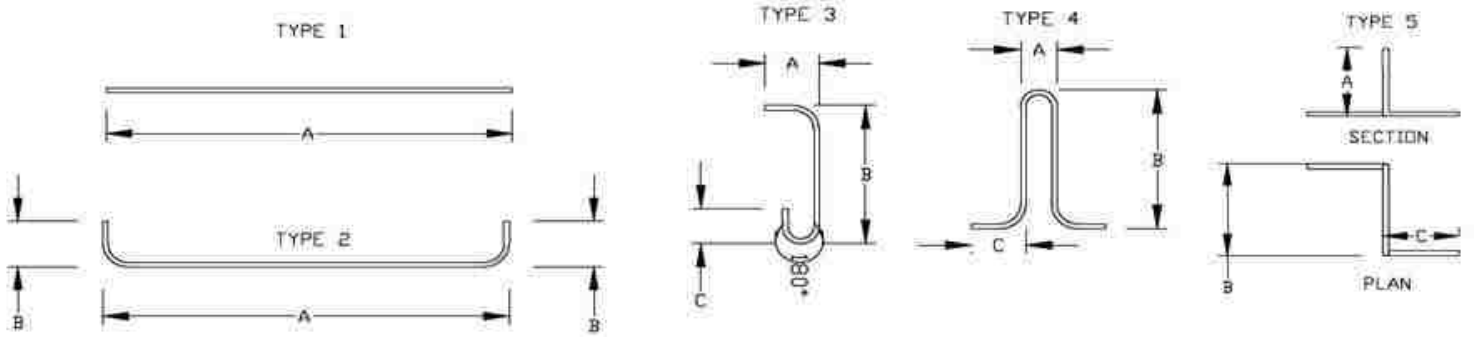


Notes:

1. All dimensions are out-to-out unless otherwise noted.

**Figure B - 10: Footing steel schedule**

# Appendix C: Test photos

**PreT-BS**

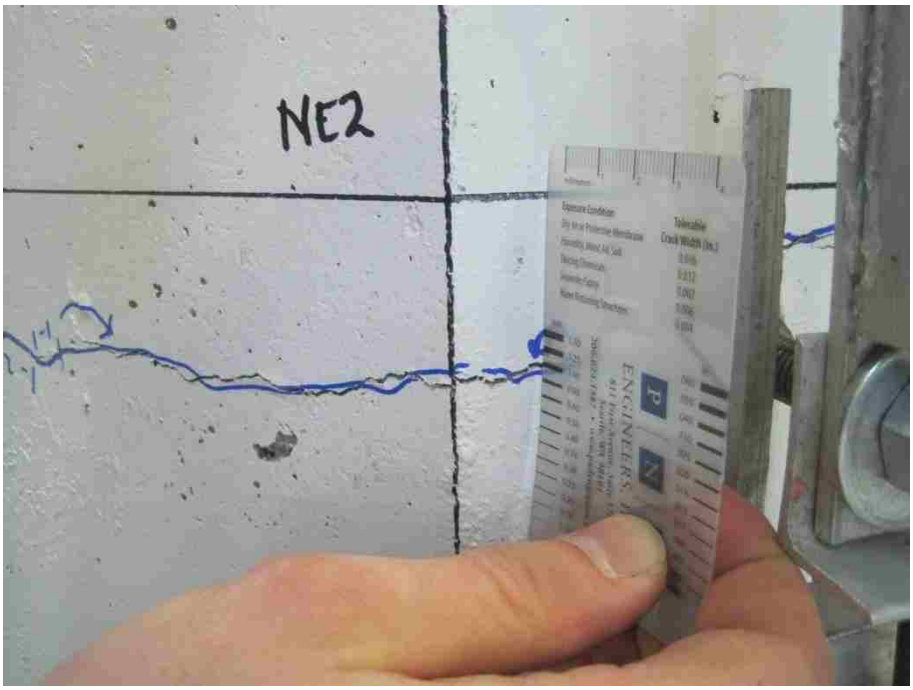


**Figure C - 1: First significant horizontal crack, cycle 3-1.**

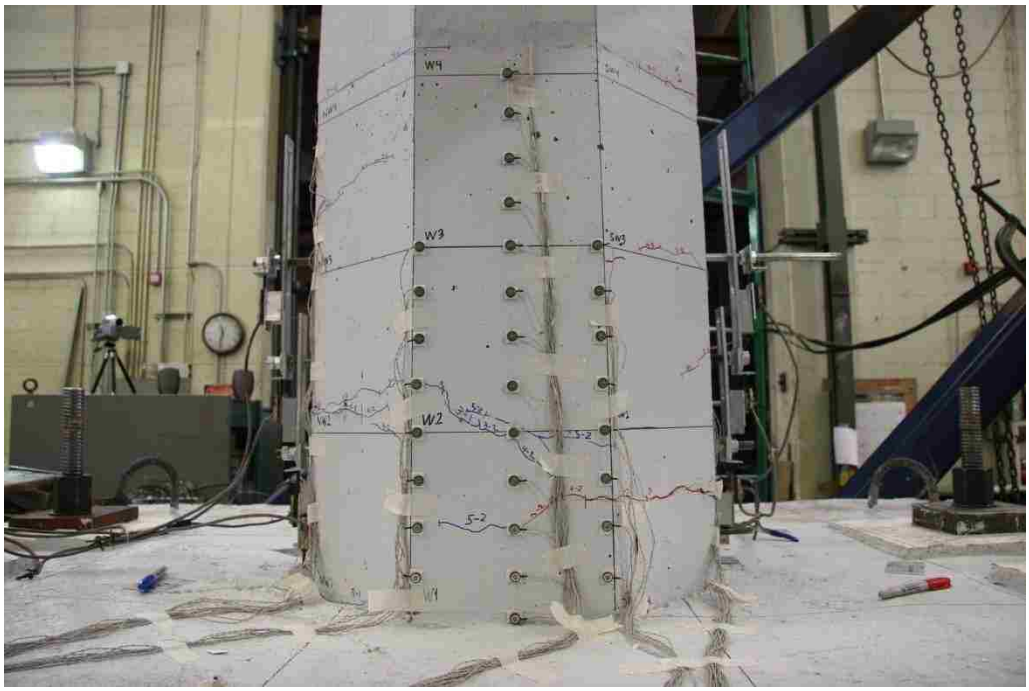


**Figure C - 2: First open residual crack, cycle 4-1.**

**Figure C - 3: Column fully spalled, cycle 9-1.**

**Figure C - 4: Large crack in concrete core, cycle 9-1.**

**Figure C - 5: Fracture of longitudinal reinforcement, cycle 8-1.**

**Figure C - 6: End of testing.**

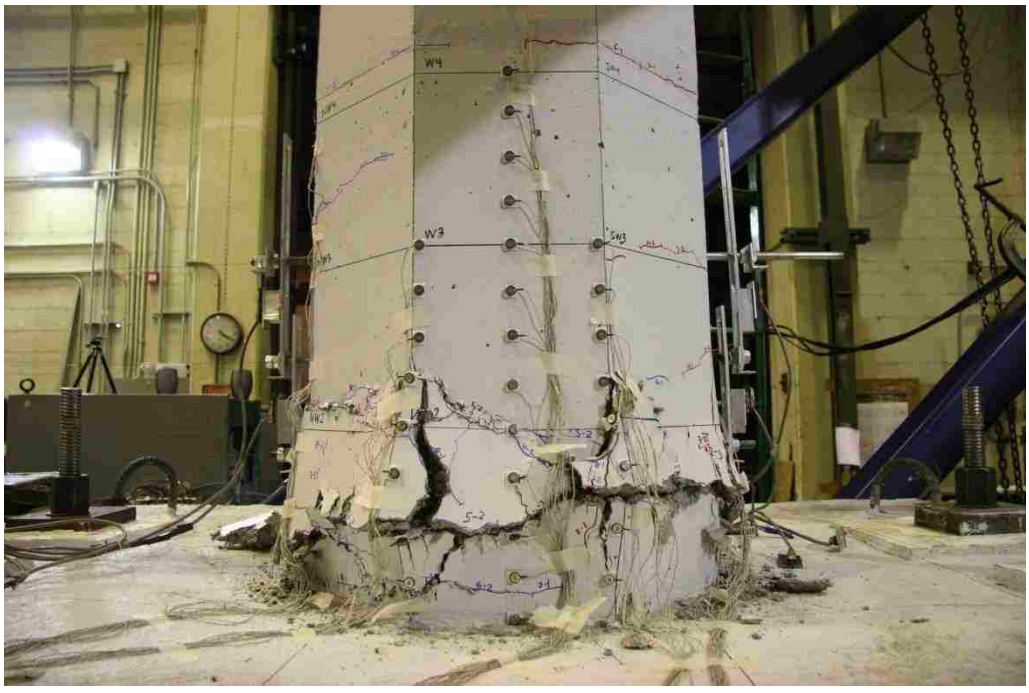


**Figure C - 7: End of testing, side view.**

**PreT-SS**

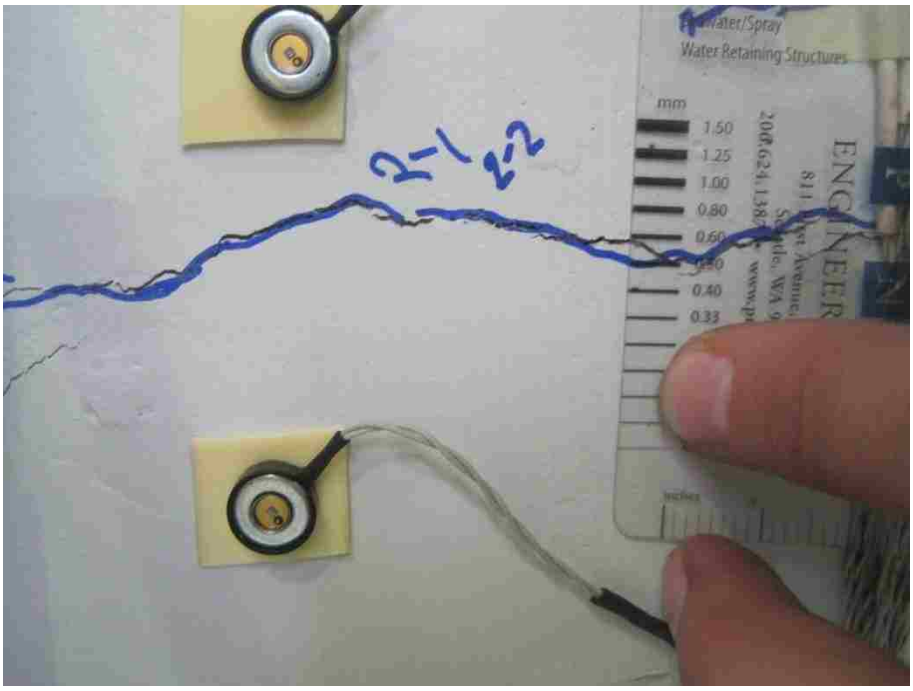


**Figure C - 8: First significant horizontal crack, cycle 3-2.**

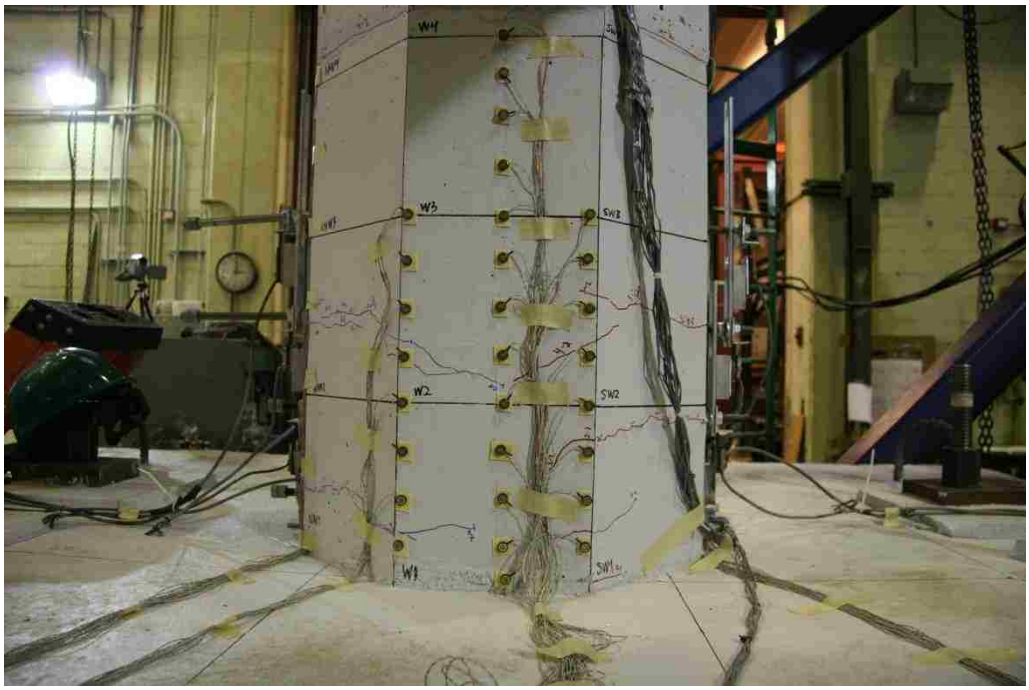


**Figure C - 9: First open residual crack, cycle 5-2.**

**Figure C - 10: Column fully spalled, cycle 9-1.**


**Figure C - 11: Large crack in concrete core, cycle 8-2.**

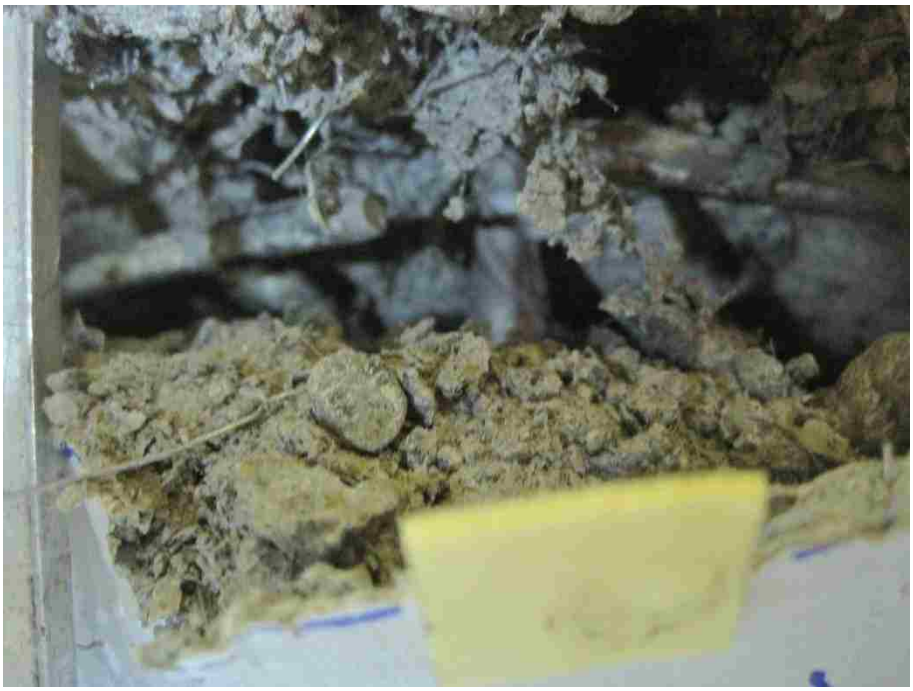

**Figure C - 12: Fracture of longitudinal reinforcement bar, cycle 9-2.**

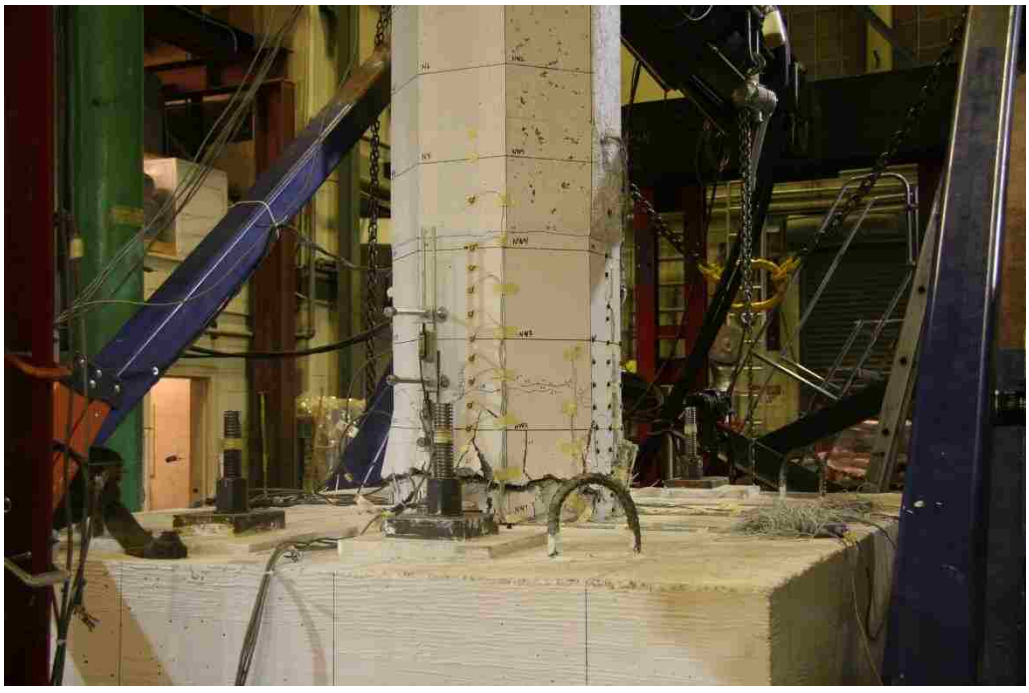

**Figure C - 13: End of testing.**

**Figure C - 14: End of testing, side view.**

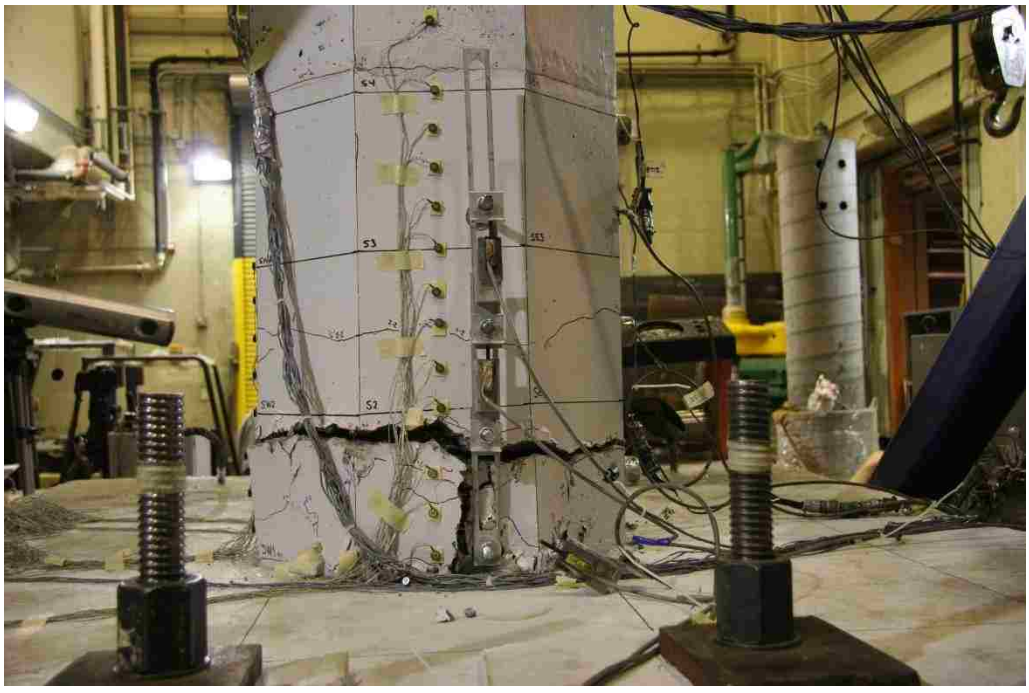

**Figure C - 15: End of testing, seen from south end of specimen.**

# Appendix D: Stainless steel reinforcing bars

This appendix describes the investigation into stainless steel reinforcing bars that was conducted prior to selecting bars for use in the tests.

Many alloys of stainless steel are available and provide different features, most of which are associated with corrosion resistance. ASTM A276 lists most of the stainless steel alloys that are suitable for use in concrete reinforcement bars. According to Trate et al. (2004) most stainless steel used for structural purposes falls into one of four major categories: alloy 2205 (S31803), type 316LN (S31653), 18Cr-3Ni-12Mn stainless that now-a-days is called EnduraMet 33 (or XM-29) (S24000) and type 304LN (S30453). Therefore we decided to look at these four alloys and one new one called EnduraMet 32 (or XM-28) (S24100). The S numbers are the UNS designation of the stainless steel alloys.

**Table D - 1: Alloys researched in the progress of choosing stainless steel reinforcement bars (ASTM International , 2010).**

| Alloy | UNS # |
|---|---|
| Type 304LN | S30453 |
| Type 316LN | S31653 |
| Alloy 2205 | S31803 |
| EnduraMet 33 | S24000 |
| EnduraMet 32 | S24100 |

The general characteristics of the alloys are discussed below.

Type 304LN (S30453) is a nitrogen-strengthened version of another stainless steel alloy type 304L (S30403). Adding nitrogen to the alloy of type 304L strengthens the alloy, and type 304LN has much higher yield and tensile strength than type 304L but comparable ductility, corrosion resistance and non-magnetic properties. Its corrosion resistance is similar to that of EnduraMet 33.

Type 316LN (S31653) is similar to 304LN, and is a nitrogen-strengthened version of another stainless steel alloy, type 316L. The higher nitrogen content makes the alloy a little more resistant to chloride pitting and crevice corrosion.

Alloy 2205 (S31803) is a duplex alloy in the sense that it has a microstructure consisting of both austenite and ferrite phases. The microstructure gives the alloy a magnetic feature and is therefore not

an appropriate choice in environment that contain device that are sensitive to magnetic fields. This alloy also has one of the best corrosion resistant available of most stainless steel alloys.

EnduraMet 33 (S24000) is high manganese and nitrogen strengthened stainless steel that has an austenitic microstructure. The alloy provides a higher yield and tensile strengths than type 304 alloy (S30400) but the corrosion resistance is somewhat lower that of type 304.

EnduraMet 32 (S24100) is a high manganese, low nickel, nitrogen-strengthened stainless steel with an austenitic microstructure like EnduraMet 33. The nitrogen provides higher yield and tensile strengths without losing any of the corrosion resistance or non-magnetic properties. (Carpenter Technology Corporation, 2002) (Carpenter Technology Company, 2010).

For the purposes of seismic resistance, one of the most important characteristics of stainless steel reinforcing bars is their mechanical properties, and in particular Young's modulus and minimum yield strength. Typical values are given in Table D - 2.

**Table D - 2: Mechanical properties of alloys investigated, yield strength is defined the stress when the steel reaches 0.2% elongation (Carpenter Technology Company, 2010).**

| Alloy | E [ksi] | Minimum yield strength [ksi] |
|---|---|---|
| Type 304LN | 29000 | 75 |
| Type 316LN | 29000 | 75 |
| Alloy 2205 | 28000 | 75 |
| EnduraMet 33 | 29000 | 75 |
| EnduraMet 32 | 29000 | 75 |

The relative resistance to corrosion of the different alloys is also of interest and is presented in Table D - 3.

**Table D - 3: 5 level rating scale for corrosion resistance is for comparative purposes, none being worst resistant and excellent the best (Carpenter Technology Company, 2010).**

| Alloy | Nitric Acid | Phosphoric Acid | Sodium Hydroxide | Sea Water | Salt (NaCl) Spray |
|---|---|---|---|---|---|
| Type 304LN | Good | Moderate | Moderate | Restricted | Good |
| Type 316LN | Good | Moderate | Moderate | Moderate | Good |
| Alloy 2205 | Good | Moderate | Moderate | Moderate | Excellent |
| EnduraMet 32 | Good | Restricted | Moderate | Restricted | Good |
| EnduraMet 33 | Good | Restricted | Moderate | Restricted | Good |

To evaluate a steel's suitability for use in the unbonded pre-tensioned system, mechanical characteristics other than just the minimum yield strength are needed. Cyclic strain hardening is one of the most important features. Many stainless steel alloys gain strength under cyclic loading, but the prestressing must be designed to overcome the compressive force in the bars if the column is to re-center. Thus, if the stainless steel strain-hardens excessively, the area of strand has to be larger to ensure re-centering. Both the extent and the predictability of the strain hardening are therefore important.

Researchers at the University of Buffalo (Zhou et al. 2008) have studied the cyclic properties of three types of stainless steel (EnduraMet 32, 316LN and alloy 2205), and MMFX II, which is a high strength, corrosion resistant steel that was recently developed. (MMFX, 2013). The results showed that the stainless steel reinforcing bars are much more ductile that the regular A706 Gr60 and MMFX II, and MMFX II has the least ductility. It was therefore not included in this investigation (Zhou et al., 2008).

The researchers conducted monotonic tension tests and cyclic tests.

**Table D - 4: Results from the monotonic tension test with gauge length of 2.25" (Zhou et al., 2008).**

| Alloy | E [ksi] | Specified $\sigma_y$ [ksi] | Actual $\sigma_{y1}$ [ksi] | Actual $\sigma_{y2}$ [ksi] | Actual $\sigma_u$ [ksi] | $\sigma_u / \sigma_{y2}$ | Elongation [%] |
|---|---|---|---|---|---|---|---|
| Type 316LN | 28981 | 75 | 77.14 | 77.75 | 116.34 | 1.50 | 52.8 |
| Alloy 2205 | 27705 | 75 | 94.06 | 96.97 | 130.53 | 1.35 | 38.7 |
| EnduraMet 32 | 29848 | 75 | 84.17 | 83.52 | 136.25 | 1.63 | 61.0 |
| A706 G60 | 30244 | 60 | 73.67 | 72.59 | 106.02 | 1.46 | 26.5 |

σy1 is determined by 0.2% offset method according to ASTM E 8, ASTM International (2004).

σy2 is defined as the stress corresponding to a strain of 0.35 percent, ACI Committee (2005).

Figure D - 1 compares the monotonic stress-strain curves.

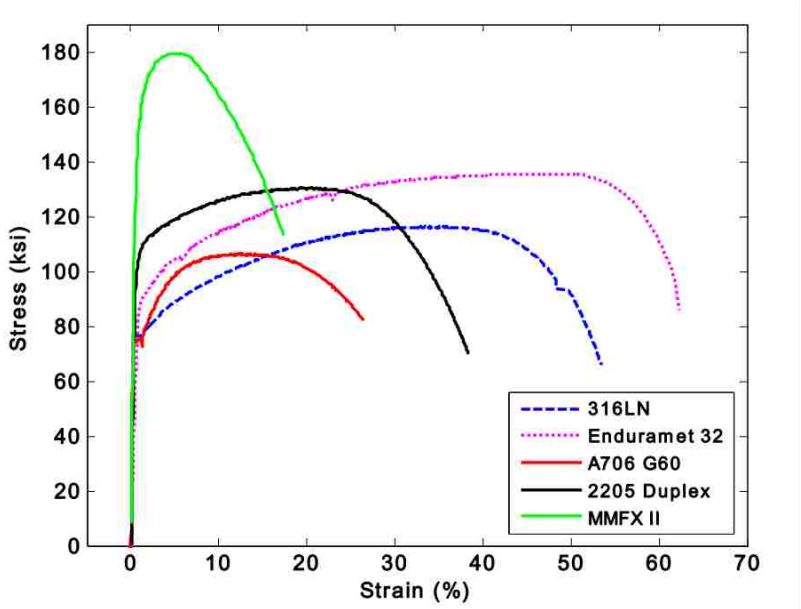


**Figure D - 1: Results from the monotonic tension tests done at University of Buffalo (Zhou et al., 2008).**

Three complete fatigue tests were completed on each alloy, defined by the R value, where R is the mean strain during the test. Strain vs. stress curves for the 316LN, 2205 and Enduramet-32 alloys and the ASTM A706 steel are shown in Figure D - 2 through Figure D - 13, for the cases of zero mean strain (R = −1), positive mean strain (R > −1) and negative mean strain (R < −1).

The results for stainless steel 316LN are shown in Figure D - 2 through Figure D - 4.

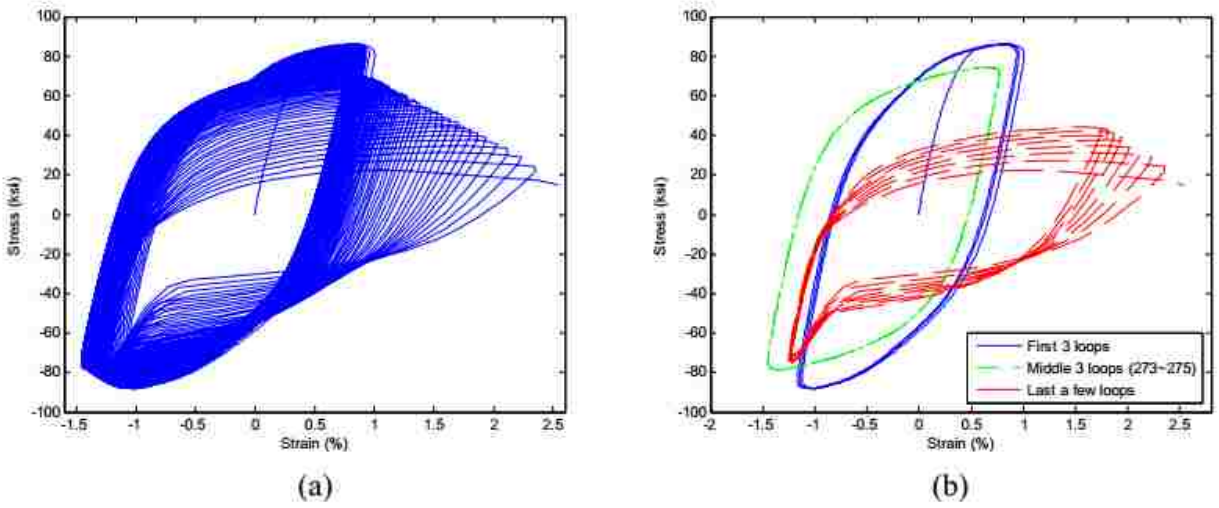


**Figure D - 2: Low-Cycle Fatigue Hysteresis Loops for 316LN at Strain Amplitude 1.116% (R = -1) (a) Whole Loops (b) Loop Extract (Zhou et al., 2008).**

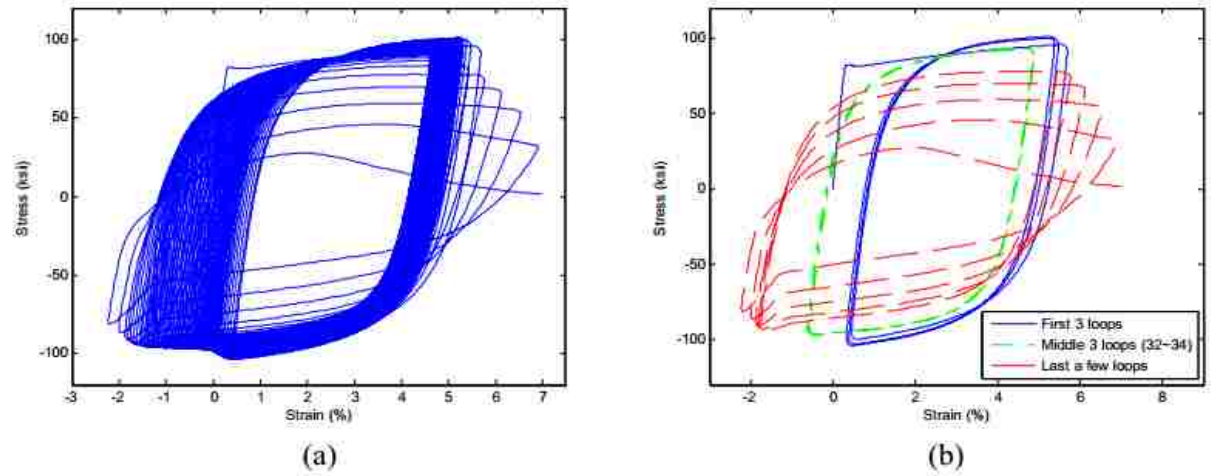


**Figure D - 3: Figure D.2 Low-Cycle Fatigue Hysteresis Loops for 316LN at Strain Amplitude 1.116% (R = -1) (a) Whole Loops (b) Loop Extract (Zhou et al., 2008) 1**

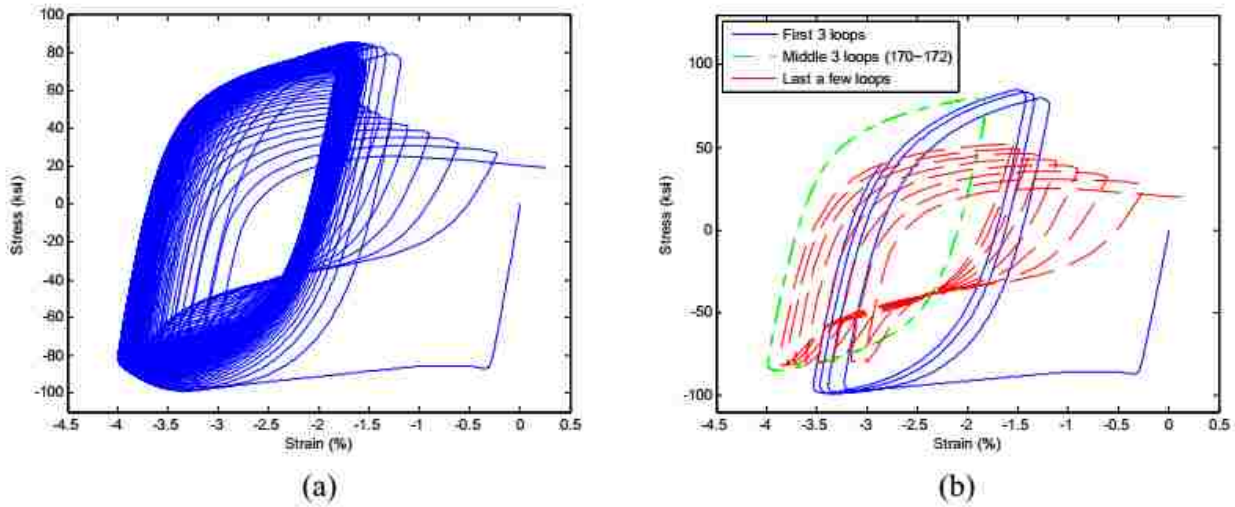


**Figure D - 4: Low-Cycle Fatigue Hysteresis Loops for 316LN at Strain Amplitude 1.097% (R < -1) (a) Whole Loops (b) Loop Extract (Zhou et al., 2008).**

The steel seemed to have a sharp yield on the first cycle in two of the three tests but not the third. Also the strain limits seemed to drift a lot in the small strain range test (R = -1). The cycling appears to cause a reduction in stress rather than an increase (i.e. negative strain hardening).

Next three figures will show the results for stainless steel alloy 2205 (duplex):

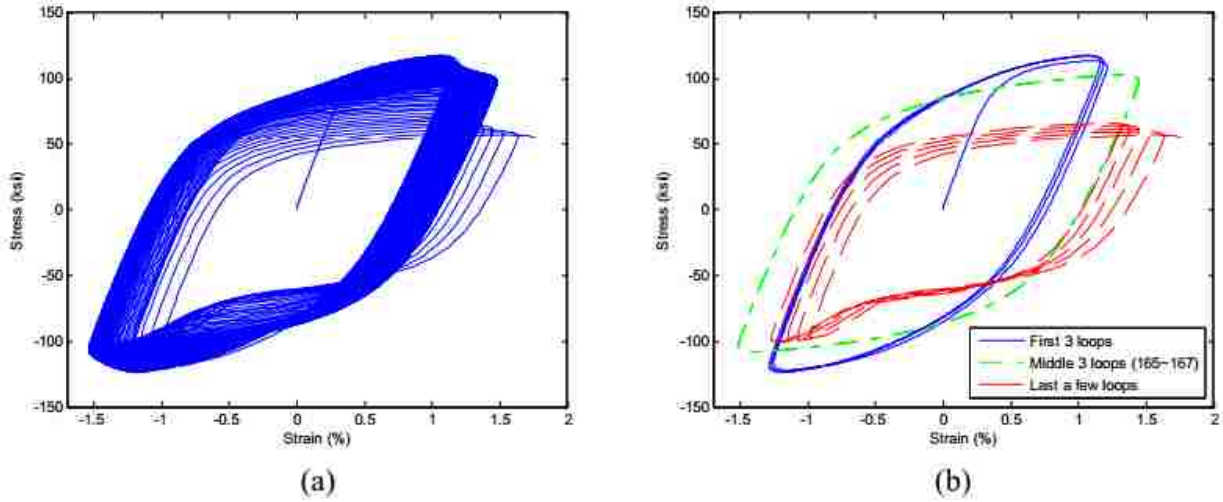


**Figure D - 5: Low-Cycle Fatigue Hysteresis Loops for Alloy 2205 (Duplex) at Stain Amplitude 1.450% (R = -1) (a) Whole Loops (b) Loop Extract (Zhou et al., 2008).**

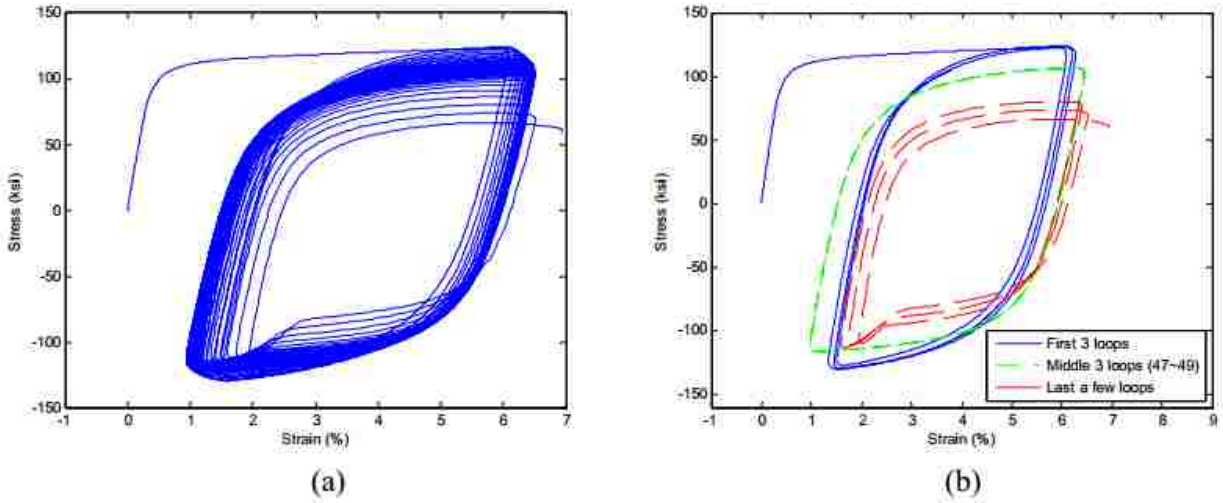


**Figure D - 6: Low-Cycle Fatigue Hysteresis Loops for Alloy 2205 (Duplex) at Strain Amplitude 2.744% (R > -1) (a) Whole Loops (b) Loop Extract (Zhou et al., 2008).**

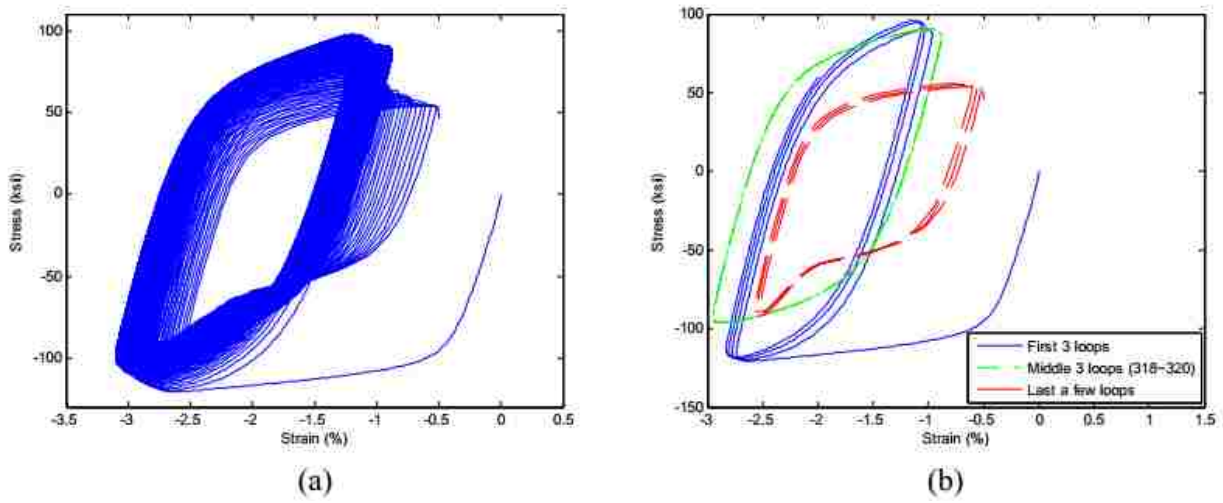


**Figure D - 7: Low-Cycle Fatigue Hysteresis Loops for Alloy 2205 (Duplex) at Strain Amplitude 1.014% (R < -1) (a) Whole Loops (b) Loop Extract (Zhou et al., 2008).**

Alloy 2205 did certainly not have sharp yield at 316LN on the first cycle in in any of the tests. The strain limits also seemed to be much more stable than for the stainless steel of type 316LN. When the alloy is subjected to cyclic loading the alloy response is negative strain hardening. On the other hand the negative strain hardening is much less for alloy 2205 than 316LN and alloy 2205 tends to keep the strength longer during cyclic loading.

The results for the stainless steel alloy EnduraMet 32 are displayed in Figure D - 8 through Figure D - 10.

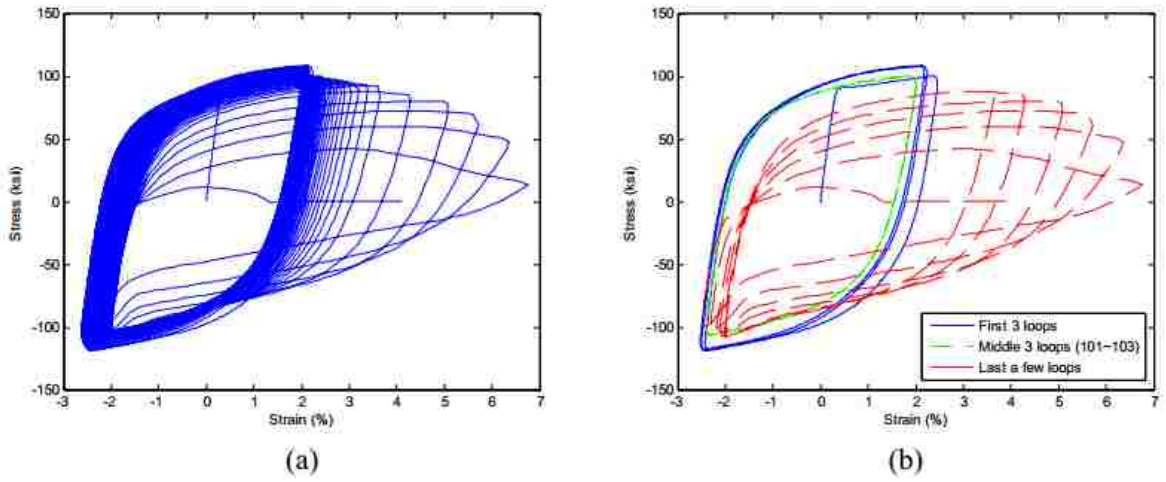


**Figure D - 8: Low-Cycle Fatigue Hysteresis Loops for EnduraMet 32 at Strain Amplitude 2.238% (R = -1) (a) Whole Loops (b) Loop Extract (Zhou et al., 2008).**

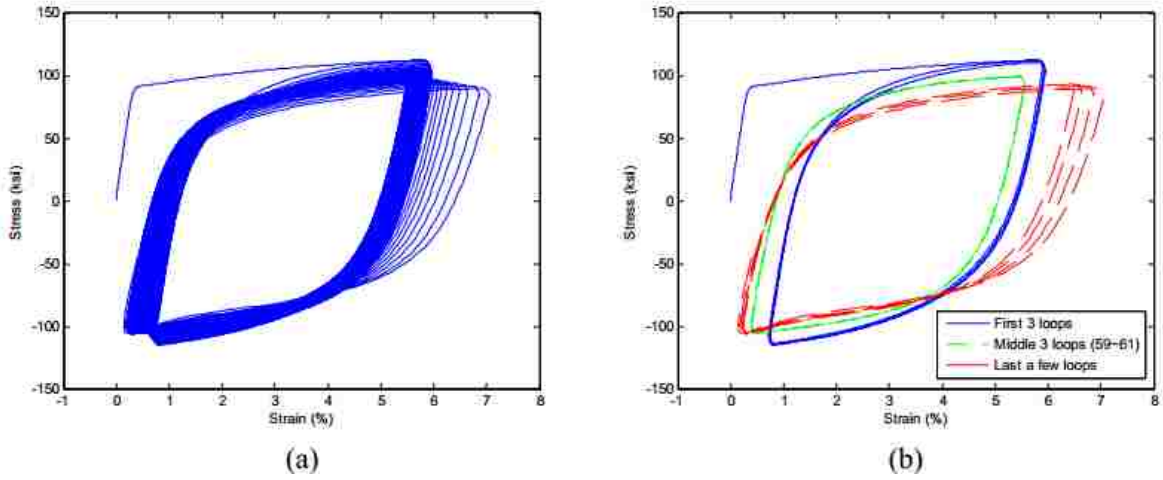


**Figure D - 9: Low-Cycle Fatigue Hysteresis Loops for EnduraMet 32 at Strain Amplitude 2.608% (R > -1) (a) Whole Loops (b) Loop Extract (Zhou et al., 2008).**

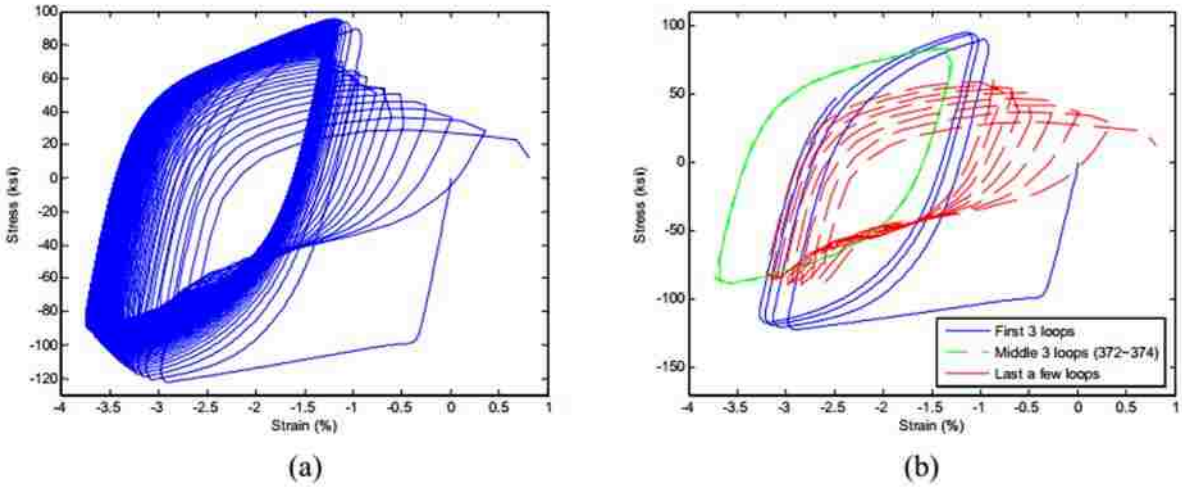


**Figure D - 10: Low-Cycle Fatigue Hysteresis Loops for EnduraMet 32 at Strain Amplitude 1.205% (R < -1) (a) Whole Loops (b) Loop Extract (Zhou et al., 2008).**

In all load cases the EnduraMet 32 resulted in a sharp yield. The strain limits drifted a lot for both load case R = -1 and R < -1. When the alloy is subjected to cyclic loading the alloy response is negative strain hardening. The negative strain hardening seemed less than for the 316LN but much more than for alloy 2205.

To get a good comparison results for the regular carbon steel A706 G60 are displayed in the next three figures.

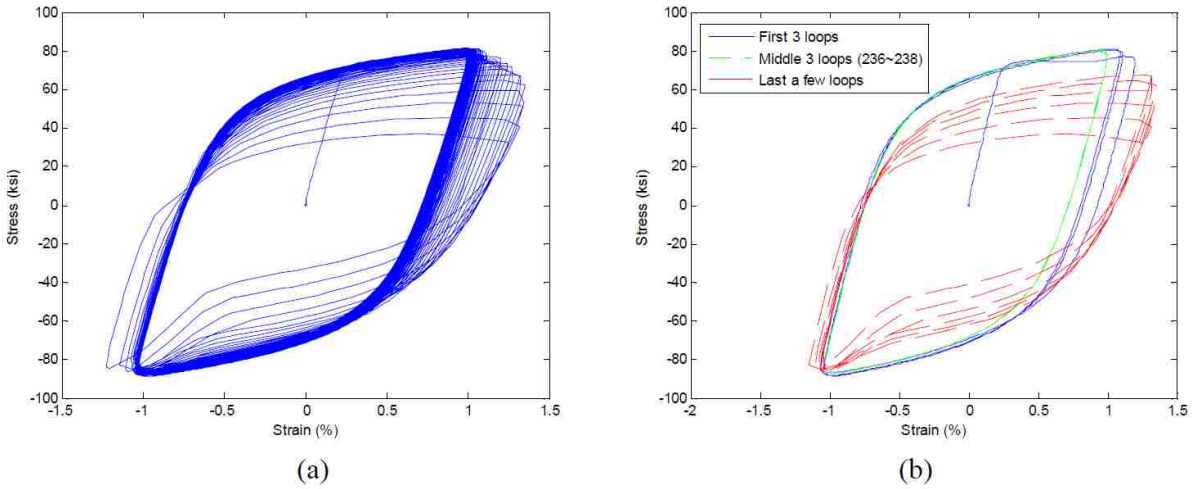


**Figure D - 11: Low-Cycle Fatigue Hysteresis Loops for A706 G60 at Strain Amplitude 1.022% (R = -1) (a) Whole Loops (b) Loop Extract (Zhou et al., 2008).**

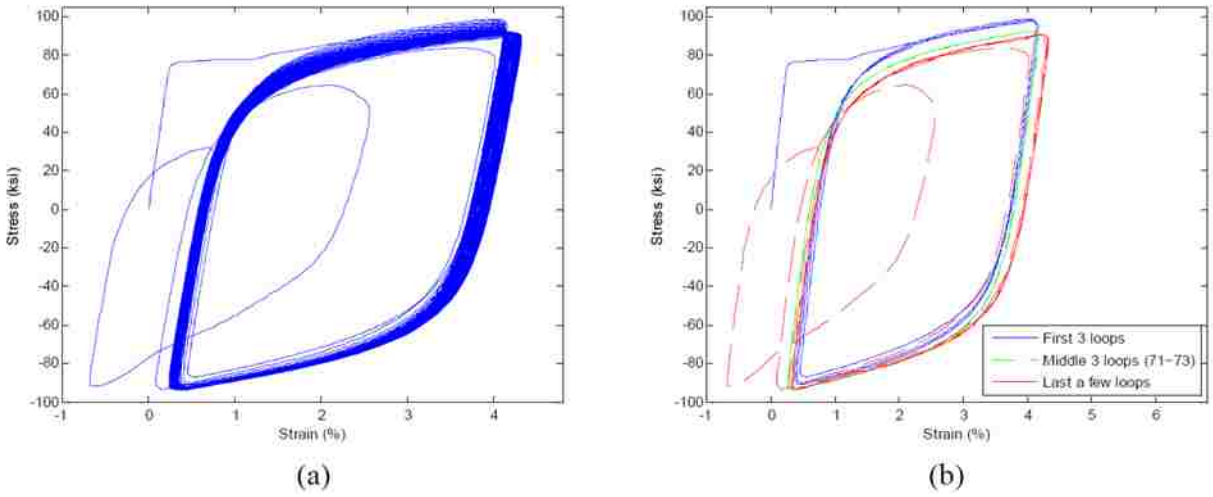


**Figure D - 12: Low-Cycle Fatigue Hysteresis Loops for A706 G60 at Strain Amplitude 1.946% (R > -1) (a) Whole Loops (b) Loop Extract (Zhou et al., 2008).**

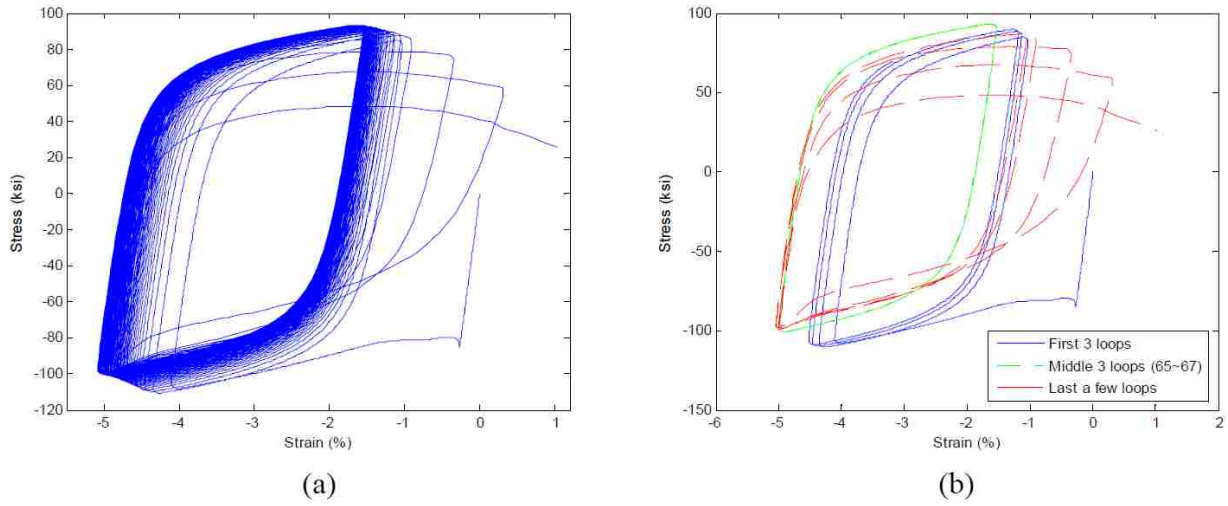


**Figure D - 13: Low-Cycle Fatigue Hysteresis Loops for A706 G60 at Strain Amplitude 1.715% (R < -1) (a) Whole Loops (b) Loop Extract (Zhou et al., 2008).**

During all the tests the A706 black steel reinforcement was most stable and kept most of its strength. Almost every loop lies on top of the previous one.

A research of strength degradation and energy dissipation of stainless steel reinforced concrete columns was performed in China in a collaboration of Foshan University, Guangdong University of Technology and The Architectural Design and Research Institute of Guangdong Province. Zhang et al. (2011) tested three specimens with stainless steel rebars and one with black steel rebar to investigate their strength degradation and energy dissipation.

The best way to see how this research worked out is to look at the results of the research. It is important to note that in this research 1.4362 duplex (S32304) stainless steel rebar was used and that alloy is most similar to the 2205 duplex alloy (S31803) at least when the chemical properties of these two alloys were compared. Also both alloys have a duplex microstructure consisting of both austenite and ferrite phases.

**Table D - 5: ASTM minimum strength limits, not that minimum strengths differ between ASTM and Carpenter Technology Company (ASTM International, 2010).**

| Alloy | ASTM minimum yield stress [ksi] | ASTM minimum tensile strength [ksi] |
|---|---|---|
| 2205 | 65 | 90 |
| 1.4362 | 58 | 87 |

Looking at the summary of the research it can be concluded that stainless steel reinforced concrete columns appear to have high flexural capacity. The total energy dissipation of the stainless steel column was 14% higher than for the comparable black steel column tested. The stainless steel columns also show good signs of ductility as expected, especially after having looked at the monotonic tension test of few stainless steel alloys and also the standard ASTM A276. The results from the authors of the research were simply: “So the reinforced concrete with stainless steel rebar can perform well in seismic” (Zhang et al., 2011).

Research was conducted at Politecnico di Milano (the Polytechnical of Milano) in collaboration with a steel melting shop in Aosta, Italy, Cogne Acciai Speciali. The research was mainly meant to present how austenitic stainless steel rebar, in this research type 304 (S30400), behaves under monotonic and cyclic loadings. Also the rebar were used to build concrete columns that were tested under cyclic loadings and comparing the results to columns with high ductile carbon steel rebar, (Franchi et al., 2006).

The monotonic stress-strain curve is shown in Figure D - 14.

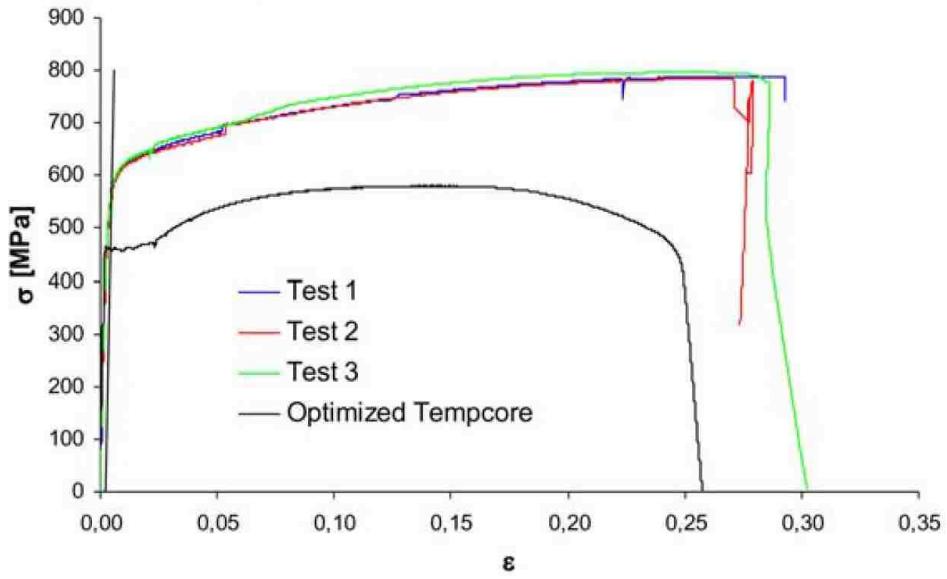


**Figure D - 14: Monotonic stress-strain curve for stainless steel type 304 in comparison with carbon steel (called Tempcore in the research). Note: 1MPa = 0.145 ksi. (Franchi et al., 2006).**

It can be noted that the end of the horizontal line of the graphs (around 20 mm or strain 0.27) is limited because the elongation test apparatus only allowed elongation up to 20 mm. These results clearly show us that the stainless steel is both stronger and more ductile than regular carbon steel.

Figure D - 15 and Figure D - 16 show the cyclic stress-stain behavior of the stainless steel (not embedded in concrete) for R = -1.

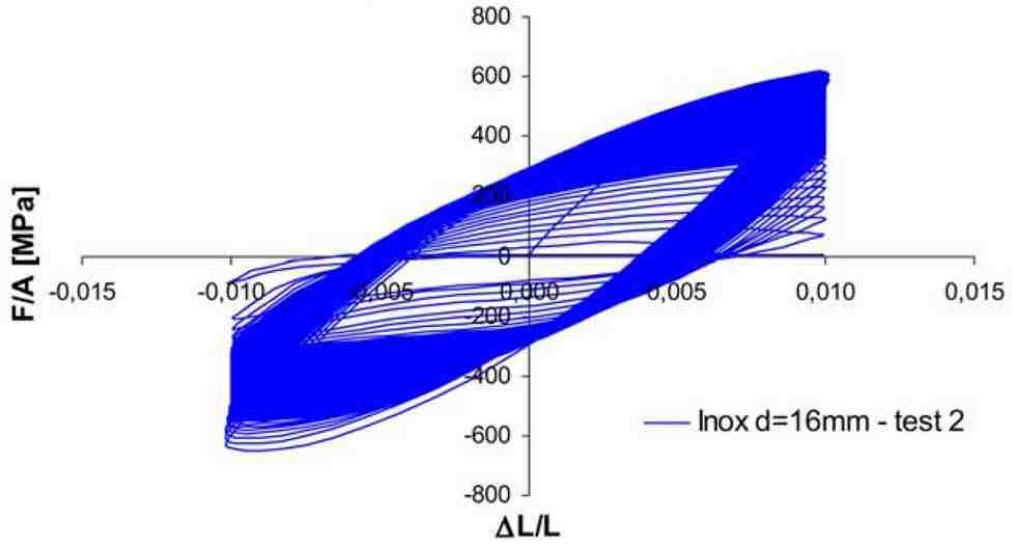


**Figure D - 15: Hysteresis behavior of stainless steel type 304 up to failure. Low cycle fatigue with ΔL/L = 1%, (Franchi et al., 2006).**

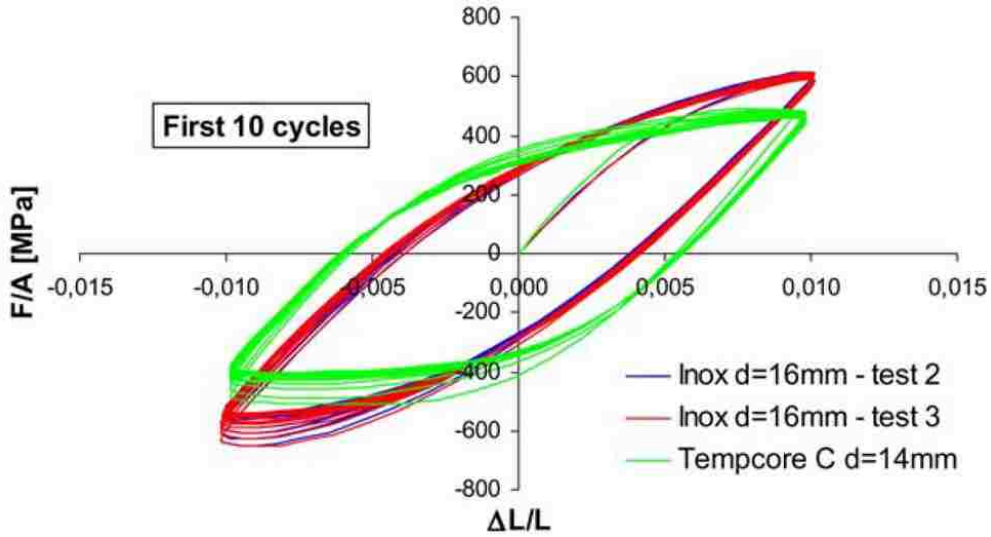


**Figure D - 16: The first 10 cycles of two tests of stainless steel type 304 compared to regular carbon steel (green hysteresis loops). Low cycle fatigue with ΔL/L = 1%, (Franchi et al., 2006).**

It is also interesting to look at the resistance decrease along all the cycles, to see how the resistance of different bars decreases with more cycles.

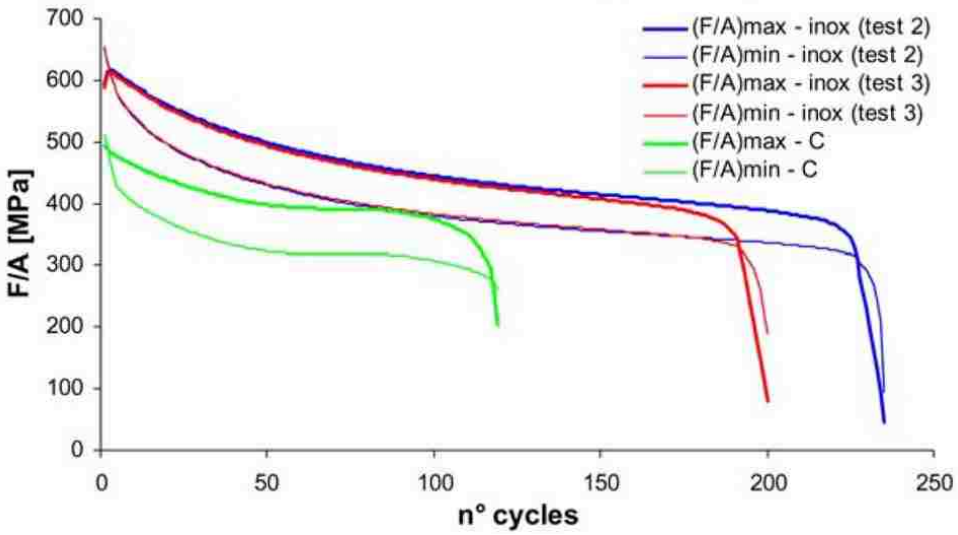


**Figure D - 17: Resistance decrease of different reinforcing bars for tests up to 1% strain. Red and blue lines are for the stainless steel and the green lines are carbon steel, (Franchi et al., 2006).**

Maybe the most interesting result from this research is the hysteresis loops of concrete column with stainless steel reinforcement bars.

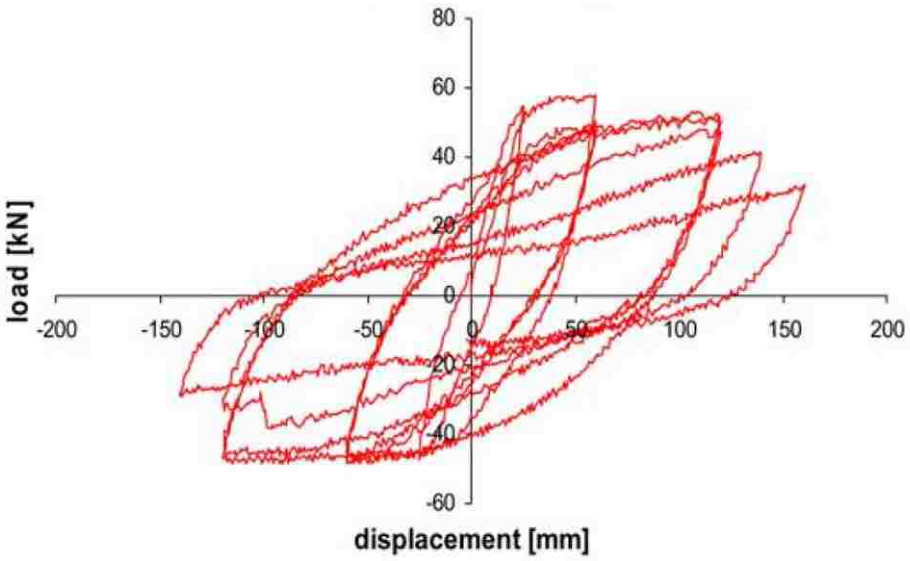


**Figure D - 18: Load-displacement hysteresis loops of the top section (1500 mm above column-footing interface) of the stainless steel concrete column, (Franchi et al., 2006).**

It is also interesting to look at the energy dissipation in every cycle and compare the column with stainless steel rebar with column with regular black (carbon) steel.

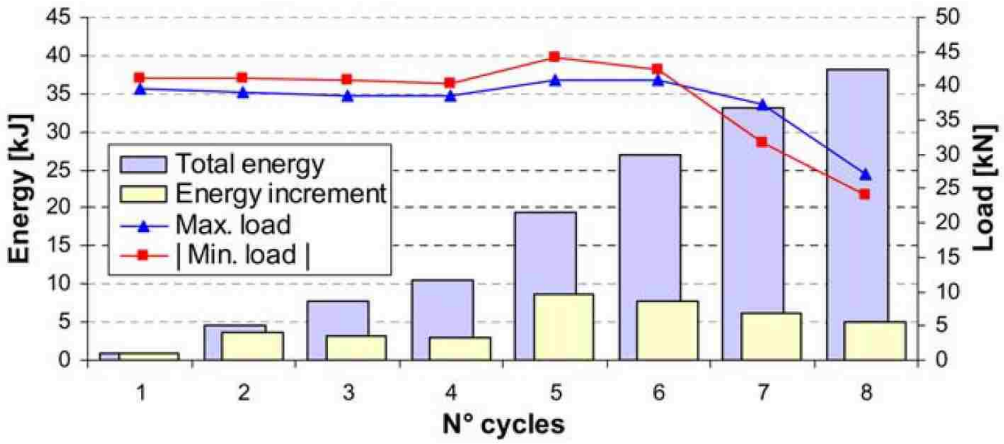


**Figure D - 19: Strength and energy dissipation of carbon steel reinforced concrete column, (Franchi et al., 2006).**

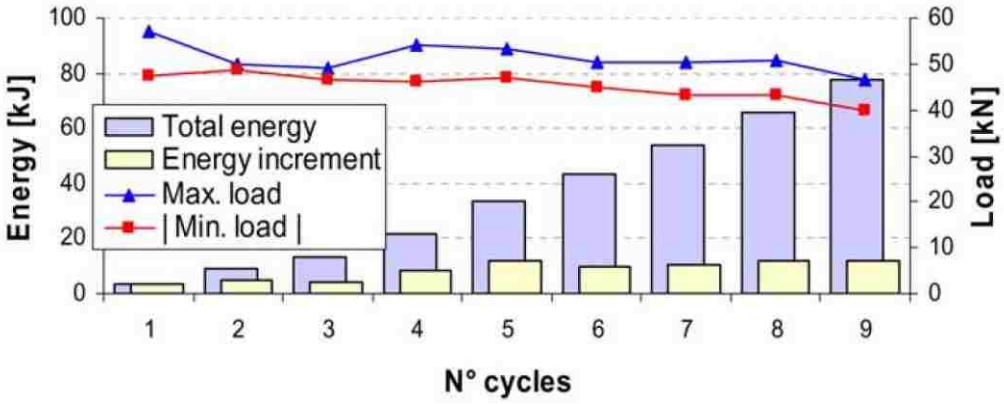


**Figure D - 20: Strength and energy dissipation of stainless steel reinforced concrete column, (Franchi et al., 2006).**

So by looking at the two graphs on strength and energy dissipation it can be seen that the stainless steel reinforced concrete column is clearly stronger than the carbon steel reinforced concrete column. Over all the cycles it can also be seen that the resistance of the stainless steel column stays closer to constant than for the carbon steel reinforcement column. By comparing the energy dissipation of the two columns it is easy to see that the stainless steel column dissipates much more energy than similar column using carbon steel.

The authors of the paper concluded that the columns reinforced with stainless steel will present, after same seismic action, a much lower level of damage than a similar column using carbon steel. On the other hand the authors also concluded that the stainless steel rebar showed unusual ductility level, both in monotonic and cyclic loading, compared to regular black steel. Tests on the prototypes also showed the ductile behavior but on the other hand also a higher horizontal force. In the research paper

they write “This fact suggests the idea of using stainless steel in seismic areas for a more limited behavior factor (larger horizontal forces) but using, at the same time, a limited steel area (because of the higher resistance of the stainless steel) and therefore resulting in expected limited damages to the structure after the earthquake.” (Franchi et al., 2006).

After looking at a number of researches on stainless steel, both embedded in concrete and in air, it can be concluded that stainless steel rebar can be used in seismic area. For the columns designed in this research it can be a problem if the rebar hardens too much as is the case for most stainless rebar. That is a problem since one of the main goals of proposed column is that they will re-center themselves and hardening of rebar will probably work against the re-centering.

The results from the Buffalo tests show that the EnduraMet 32 has the most strain hardening of all the alloys and that feature could work against the goal of a re-centering column. Therefore that alloy was eliminated.

Material availability and price were also investigated, with both these tests and future field construction in mind. Salit Specialty Rebar (SSR) is one of the premier stainless steel rebar suppliers and fabricators in North America and they were consulted. Alloy 2205 is available in many sizes (bar no. 3-11). Types 304LN and 316LN are very expensive, because of their high nickel contents, also the alloy is not as much used as 2205, perhaps because of the higher cost. Obtaining information about the alloy EnduraMet 33 was difficult (SSR does not produce it).